

Modeling the Dynamics of Central Pattern Generators and Anesthetic Action

By

TAMARA JOY SCHLICHTER

B.S. (California State University, Long Beach) 2004

DISSERTATION

Submitted in partial satisfaction of the requirements for the degree of

DOCTOR OF PHILOSOPHY

in

Applied Mathematics

in the

OFFICE OF GRADUATE STUDIES

of the

UNIVERSITY OF CALIFORNIA

DAVIS

Approved:

Timothy J. Lewis

Brian Mulloney

Anne C. Smith

Committee in Charge

2011

Contents

Abstract	v
Acknowledgments	vi
Chapter 1. General Introduction	1
Part 1. Mechanisms Underlying Locomotion in the Crayfish Swimmeret System	3
Summary	4
Chapter 2. Introduction	6
2.1. Neural mechanisms generating locomotion are complex and largely unknown	6
2.2. The crayfish locomotor neural circuit	7
2.3. Phase Response Curve (PRC)	10
2.4. Theory of Weakly Coupled Oscillators (TWCO)	13
2.5. Previous modeling work	14
2.6. Aims of Part 1	18
Chapter 3. Phase Response Properties of Half-Center Oscillators using Morris-Lecar Intrinsic Dynamics	20
3.1. Summary	30
Chapter 4. Phase Response Properties of Half-Center Oscillators using Phase Models	31
4.1. The HCO phase model	31
4.2. Derivation of map for firing times	34
4.3. PRC of HCO	38
4.4. Application to sinusoidal PRCs	43
4.5. Summary	49

Chapter 5. Phase Response Properties of Half-Center Oscillators using Leaky Integrate-and-Fire Models	52
5.1. General form of PRC for HCO	52
5.2. δ -function synapses	58
5.3. Exponential synapses	61
5.4. Examples	62
5.5. Summary	65
Chapter 6. Phase Locking Dynamics in a Chain of Half-Center Oscillators	66
6.1. Intersegmental Connectivity	67
6.2. Numerical simulations in a chain of HCOs	67
6.3. Applying the theory of weakly coupled oscillators (TWCO)	71
6.4. Summary	77
Chapter 7. Addendum: Analysis of HCO phase models	79
7.1. HCO phase model with standard δ -function synapses	79
7.2. HCO phase model with exponential synapses	82
7.3. The correct limit to synaptic currents with fast decay	84
7.4. Summary	87
Chapter 8. Crayfish Conclusion	88
8.1. Summary	88
8.2. Future Modeling and Experimental Work	89
Appendix A.	91
A.1. Morris Lecar Model	91
A.2. Linearization of Firing Map	93
A.3. iPRC for LIF model	94
Part 2. Dynamical and Biophysical Mechanisms of Anesthetic Action	96
Summary	97
Chapter 9. Physiological Background	98
9.1. Volatile anesthesia in the lamprey spinal cord	98

9.2. Neural network underlying fictive locomotion in lamprey spinal cord	99
9.3. Isoflurane action on the isolated spinal cord preparation	102
9.4. Previous work on anesthetics	105
9.5. Isoflurane targets	108
Chapter 10. Mathematical Models and the Mechanism of Bursting Using Bifurcation Diagrams	109
10.1. The Brodin et al. model is a biophysical model of the lamprey EIN	109
10.2. The Butera et al. model is a minimal bursting model.	110
10.3. Hodgkin-Huxley formalism for neuronal models.	110
10.4. Bursting mechanisms	111
10.5. Understanding bursting through bifurcation analysis	113
Chapter 11. Results	117
11.1. Model for TREK and TASK	117
11.2. The Modified Butera et al. Model	121
11.3. The Reduced and Modified Brodin et al. Model	126
Chapter 12. Conclusion	133
12.1. Summary	133
12.2. Future Experimental Work	134
12.3. Future Modeling Work	136
Appendix B.	139
B.1. Modified Butera et al. model	139
B.2. Reduced and modified Brodin et al. model	142
Bibliography	145

Tamara Joy Schlichter

March 2011

Applied Mathematics

Modeling the Dynamics of Central Pattern Generators and Anesthetic Action

Abstract

This thesis contains two parts. Part 1 of this thesis has two goals. The first is to understand the phase response properties of half-center oscillators (HCOs) using idealized models. The second is to begin developing an understanding of the phase-locking mechanisms between coupled half-center oscillators using numerical simulations and the theory of weakly coupled oscillators. This work is a starting point towards a greater understanding of the mechanisms underlying coordinated limb movement during locomotion in the crayfish swimmeret system. The analysis is compared to experimental data from the crayfish swimmeret system and possible experiments are suggested.

The goal of Part 2 of this thesis is to build mathematical models to study the effects of volatile anesthetic on neural networks in the spinal cord. The network under consideration is composed of excitatory interneurons in the lamprey central pattern generator (CPG), a spinal cord neuronal network responsible for generating rhythmic locomotor movement in vertebrates such as swimming or walking. It is thought that the excitatory interneurons of the CPGs are the main target of the volatile anesthetic isoflurane, leading to immobility under anesthesia. We model these interneurons and incorporate the most relevant effects of the volatile anesthetic isoflurane on intracellular conductances using bifurcation analysis and numerical simulations.

Acknowledgments

CHAPTER 1

General Introduction

This thesis contains two parts. Part 1 uses idealized models to determine the phase response properties of a half-center oscillator (HCO) and the phase-locking properties in a chain of HCOs. Part 2 builds mathematical models to study the effects of volatile anesthesia on neural networks in the lamprey spinal cord. Both parts concern central pattern generators (CPGs) for locomotor rhythms. In part 1, we try to understand the mechanism underlying phase maintenance in the crayfish swimmeret system during normal locomotion. In part 2, we try to understand how the volatile anesthetic isoflurane stops the pattern generating neural activity in the lamprey spinal cord to cause immobility (lack of motion).

Central pattern generators (CPGs) are neural networks that produce rhythmic motor patterns such as walking, swimming, breathing, pumping blood, digestion, and flying (reviewed in [MC96] [MB01] [MBST05]). They were first introduced in 1911 by Brown [Bro11] [Bro14] as the mechanism behind the rhythmic flexion and extension of limbs in a deafferented cat.

Evidence that locomotor CPGs exist and can operate without sensory or supraspinal feedback is seen when the spinal cord is isolated [Wil61] [IW64] [GMS⁺81] (reviewed in [MS10]). An isolated spinal cord that is placed in a bath of artificial cerebrospinal fluid may intrinsically demonstrate neural activity similar to that during locomotor behavior or may produce this activity upon the application of certain neuromodulators. This is known as *fictive locomotion* and is seen in many animals including the leech [KC76], lamprey [CW80], and crayfish [HW60] [IW64].

The size of CPGs can range from one cell to hundreds of cells [MC96]. The CPGs of invertebrates usually contain small networks where individual neurons can be clearly identified (as in the crayfish). On the other hand, vertebrate CPGs usually contain large numbers of neurons that can only be identified in terms of broadly defined classes (as in the lamprey

[KHKA⁺01]). In all CPG networks, both synaptic dynamics and intrinsic neural properties of network components play a role in shaping the dynamics of the full network. Understanding this interplay is a main focus throughout this thesis.

Often, CPGs are coupled forming networks that coordinate rhythmic activity, as in coordinated limb movement during locomotion [Gri81]. In segmental animals such as the crayfish and lamprey, each segment contains one or more CPGs. The segments are coupled through ascending and descending interneurons whose relative timing and strengths are crucial to coordination.

Part 1 of this thesis is motivated by the crayfish swimmeret system. In chapters 3-5, we use both biophysical and idealized models of the crayfish CPG to develop a greater understanding of how an individual CPG responds to input. In chapter 6, we present preliminary work on what factors might be involved in achieving coordination in a chain of CPGs. Part 2 is motivated by the lamprey locomotor system. In the isolated lamprey spinal cord, application of volatile anesthetics leads to cessation of rhythmic activity, which corresponds to immobility. The mechanisms underlying this anesthetic action are the focus of part 2.

Part 1

Mechanisms Underlying Locomotion in the Crayfish Swimmeret System

Summary

Part 1 of this thesis has two goals. The first is to understand the phase response properties of half-center oscillators (HCOs) using idealized models. The second is to begin developing an understanding of the phase-locking mechanisms between coupled half-center oscillators using numerical simulations and the theory of weakly coupled oscillators. This work is a starting point towards a greater understanding of the mechanisms underlying coordinated limb movement during locomotion in the crayfish swimmeret system. The analysis is compared to experimental data from the crayfish swimmeret system and possible experiments are suggested.

Part 1 is broken down into three topics:

1. The phase response properties of idealized models of half-center oscillators are examined. The dynamics of the cells in the half-center oscillator are described by either coupled Morris-Lecar neurons, leaky integrate-and-fire neurons or coupled one-variable phase models. The coupling between the cells is described by either delta-function pulse coupling or current-based exponential synapses. Analytical or semi-analytical solutions for the phase response curves (PRCs) of the latter two idealized half-center oscillators are obtained. The form of these solutions for the PRCs show how the cell's individual PRC and the coupling properties produce the PRC of the half-center oscillator. We find that the PRC of the HCO is piecewise defined with two halves centered around half-period. Each half of the HCO's PRC is described by a product of the single cell PRC with an attenuating factor. This implies that the single PRC determines the qualitative shape of the PRC of the HCO, while the strength of coupling between the cells determines the amount of attenuation in each half.
2. The phase-locking properties of a chain of idealized HCOs are studied using numerical simulations and the theory of weakly coupled oscillators. The length of the chain varies from two to four segments long. How the phase-locked state depends on the PRC of the HCO, the coupling dynamics between HCOs, and the number of HCOs in a chain are studied. Results show that phase-locking is not guaranteed and the ability of one length of chain to phase lock does not predict phase-locking

in a different length chain. The duty cycle of intersegmental coupling is found to play a substantial role in determining the ability of the chain to phase lock.

3. The bifurcation structure of the phase model HCO is analyzed as the strength of the coupling between cells in the HCO is varied. The dependence of the stability of the anti-phase state on the type and strength of coupling is determined. Coupling is described by either current-based synapses or standard δ -pulse coupling. Results show that when HCOs are coupled with the standard δ -pulse, the stable anti-phase state undergoes a period-doubling cascade to chaos as coupling strength increases. However, when coupling is described by current-based synapses, there is only one stable anti-phase state despite changes in coupling strength. This indicates that standard δ -pulse coupling does not match the limit of the current-based synapses to the δ -pulse. We show why this is the case and determine a “corrected” δ -pulse coupling model which provides the correct limit.

CHAPTER 2

Introduction

2.1. Neural mechanisms generating locomotion are complex and largely unknown

How do animals move in a coordinated fashion? For locomotion in most mammals and arthropods, limbs must maintain a constant phase difference over a range of speeds ([SM98a] and references therein). This is known as phase constancy or phase maintenance. The cellular mechanisms that accomplish this coordination are poorly understood.

In an intact animal, the CNS is capable of coordinating limb movement to create normal locomotion. In some animals, when the neural circuitry underlying locomotion is dissected out, it is still able to generate the coordinated neuronal activity required for locomotion [HW60] [WW84]. This activity, which is called fictive locomotion, can be analyzed to elucidate the neural mechanisms by which the animal generates locomotor activity.

An example of a model system that lends itself to experimental study and mathematical modeling is the crayfish swimmeret system [HW60] [MHH06] [MH07] [SHM09] [SM98b] [JMCK03]. While much is known, many questions remain surrounding how the crayfish swimmeret system maintains coordinated locomotion. Here, we use mathematical modeling to compliment past and future experimental preparations to accelerate our understanding. The overall goal of the following chapters is to use idealized phase models to begin to understand the phase maintenance mechanism in the crayfish swimmeret system. We use the knowledge from the experimental laboratory of Dr. Brian Mulloney (University of California, Davis), who has worked to describe the neural circuitry of the crayfish and in doing so, identifying the mechanisms underlying coordinated locomotion in the crayfish [NM99] [THM01] [MHH06] [MH07] [Mul96] [SHM09] [Mul96].

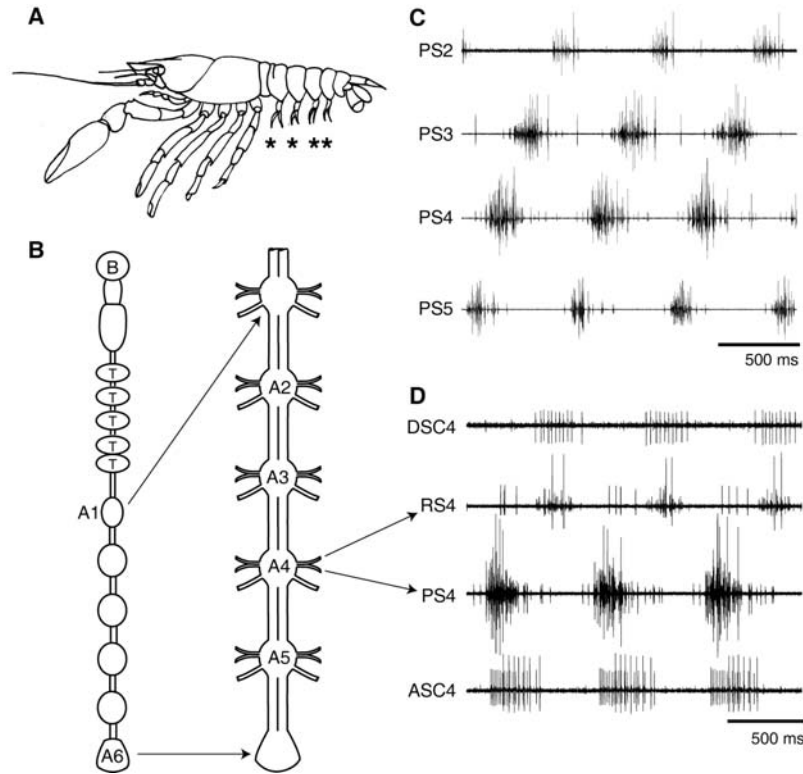


FIGURE 2.1. A) Lateral view of the crayfish. Stars mark the four swimmerets. B) Diagram of the crayfish CNS. B: brain. T: Thoracic ganglia. A1: Initial abdominal ganglia. A6: terminal abdominal ganglia. The six abdominal ganglia are expanded to show the four swimmeret ganglia A2 through A5. C) Simultaneous recordings from power-stroke (PS) branches of the swimmeret nerves from ganglia A2 (PS2), A3 (PS3), A4 (PS4), and A5 (PS5) that show three cycles of bursts of spikes in PS axons. D) Simultaneous extracellular recordings from coordinating axons (ASC4, DSC4) and PS and return-stroke (RS) branches from A4 (arrows). ASC_E spikes are the smaller of the two sizes on ASC4, and occur simultaneously with PS bursts. DCS bursts occur simultaneously with RS bursts.

2.2. The crayfish locomotor neural circuit

2.2.1. Four pairs of bilateral modules drive four pairs of bilateral swimmerets. The crayfish is a lobster-like animal that has four bilateral pairs of swimmerets responsible for generating forward thrust (starred figure 2.1A). Each swimmeret is associated with one of four segments in the crayfish abdomen (labeled A2 through A5 in figure 2.2A and 2.1B) [MH00]. Figure 2.2A shows a schematic of the main neural circuitry in one hemicord of the crayfish swimmeret system, where the hemicord is the left or right half of the ventral nerve cord. Each segment contains intersegmental coordinating neurons [MHH06] [MH07], motor neurons [MH00], and a pattern-generating module of neurons responsible for rhythm generation and coordination in the swimmeret system [MCM93] [MMC93].

Motor neurons in each module innervate the muscles of their associated swimmeret to elicit swimming. During forward swimming, the swimmerets in each segment produce alternating cycles of power-stroke (PS) and return-stroke (RS) movements driven by the home module's PS and RS motor neurons (seen in figure 2.1D). The PS and RS neurons are labeled PS2 through PS5 and RS2 through RS5 in figure 2.2A. Figure 2.1C shows simultaneous recordings from PS branches in all four segments and figure 2.1D shows simultaneous recordings from PS and RS branches in segment 4. These motor neurons are driven by a pair of non-spiking local interneurons whose synaptic organization forms the core of the local pattern-generating circuit within each module (box in figure 2.2A, expanded in 2.2B) [Mul96].

Mulloney and co-workers have shown that the intersegmental projections act to coordinate the modules to achieve a posterior-to-anterior progression of power strokes with a near 25% phase lag between neighboring swimmerets (see figure 2.1C). This phase lag persists despite changes in frequency, i.e. the system exhibits phase maintenance [MHH06]. Figure 2.1C shows recordings from power-stroke nerves in each segment during fictive swimming. Notice the phase-locked rhythm with about 25% phase lag between segments with the most posterior segment leading the rhythm. How the CNS coordinates neural activity in the modules to create and maintain this specific phase-locked rhythm is the long-term goal of this project.

2.2.2. Local non-spiking neurons make up each segmental CPG. In each hemisegment, a pair of non-spiking local interneurons form reciprocal inhibitory connections, creating a local half-center oscillator (HCO) [PM85]. HCOs occur in many rhythm generating networks such as in *Clione* swimming [Sat85] [AOP⁺93], *Xenopus* embryo swimming [AOP⁺93], crayfish locomotion [Mul96], lamprey swimming [GW99], and leech heartbeat [CDS92]. However, the crayfish is an especially simple case in that the CPG can be accurately modeled as one HCO with only two cells. HCO models for central pattern generators, which usually consist of two large groups of neurons, are widely studied [MS90] [PM74] [JMKK03] [JK06]. HCOs consist of two cells (or groups of cells) connected by relatively strong reciprocal inhibition [Bro11] [Bro14] (figure 2.2B). Typically, the cells in a HCO are phase-locked in an anti-phase state: the cells rhythmically switch between states in which

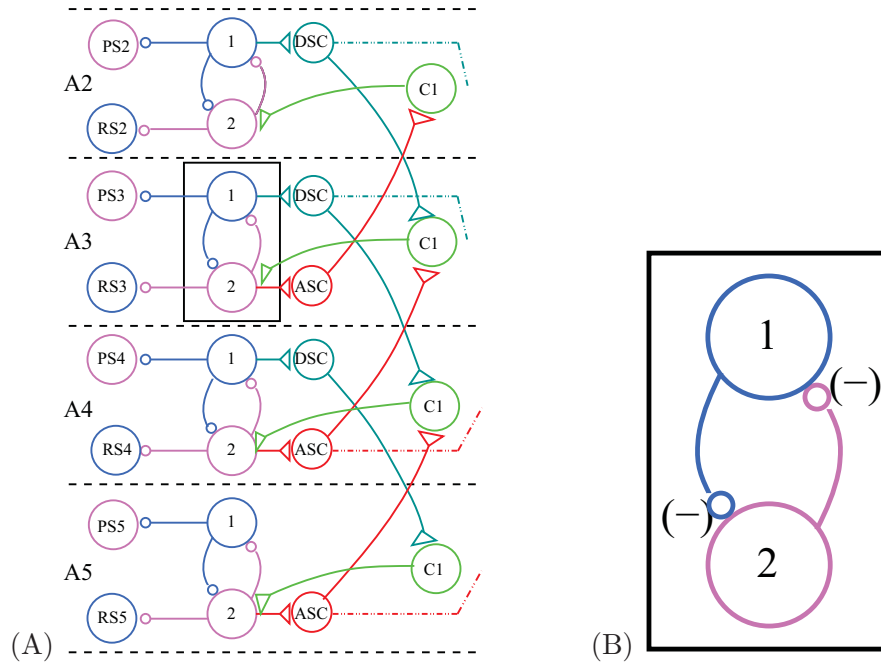


FIGURE 2.2. (A) Main circuitry of the crayfish swimmeret system. Horizontal dotted lines separate each of the four segments. Each segment contains power-stroke (PS) and return-stroke (RS) motor neurons driven by a pair of non-spiking local interneurons (1) and (2). Cell 1 drives the descending interneurons (DSC) which relay information to the commissural interneurons (C1) in each posterior segment. Cell 2 drives the ascending interneurons (ASC) which relay information to the commissural interneurons (C1) in each anterior segment. The commissural interneurons (C1) then relay that information through a graded synapse to cell 2 in their home segments. Circles represent inhibitory connections. Triangles represent excitatory connections. (B) The pattern generating circuit in each segment is a half-center oscillator (two cells coupled with reciprocal inhibition), which we study independently of all other segments.

one cell is active while the other is suppressed. This allows for the alternating order of two antagonistic movements. In the case of the crayfish, this neural behavior drives the power stroke and return stroke movements of the swimmerets. Depending on the strength and type of synaptic connection between the cells within a HCO, the cells may exhibit other behaviors such as synchrony, alternating order firing, a stable asymmetric steady state, and even chaos [WR92] [TKB98] [LR03] [OM09]. However, for purposes of studying the crayfish swimmeret system, we are only interested in the stable anti-phase state.

2.2.3. Intersegmental coordinating neurons connect modules. Each segmental module contains two coordinating neurons that project axons to influence other modules [Ste71] [NM99]. The ascending coordinating neuron (ASC), which receives input in phase with PS motor neurons, projects in an ascending direction to influence more anterior modules. The descending coordinating neuron (DSC), which receives input in phase with RS motor neurons, projects in a descending direction to influence more posterior modules (see

figure 2.2A). However, the coordinating neurons do not exert their influence on the HCO neurons in their target modules directly. Rather, they synapse onto commissural interneurons within each module, which are called ComInt 1 (labeled C1 in figure 2.2A) [SHM09]. In each module, ComInt 1 integrates the input from ASC and DSC neurons, then relays the information to the local interneurons via a graded synapse [MH03]. The connection through ComInt 1 is a recent discovery and creates a novel form of intersegmental circuitry with unknown consequences. Previous modeling work and experimental study had assumed modules were directly connected via coordinating neurons [JMKK03] [SM98b] [MH07].

2.3. Phase Response Curve (PRC)

To understand phase-locking in the crayfish swimmeret system, we must first understand how the HCOs in each module respond to external stimuli. The oscillatory dynamics of the HCO are shaped by the synapses between the two cells as well as the intrinsic dynamics of the cells, i.e. it is the entire HCO that controls the oscillation in each segment. To understand how the HCO will respond to external input, we use phase response curves (PRCs). In neurophysiology, PRCs are usually measured for single cells. However, we want to understand how the entire HCO in each module will respond to perturbations from other segments, and therefore we need the PRC of the HCO. Treating the HCO as a ‘single unit’, we examine how its phase resetting properties are generated from the intrinsic dynamics of the cells within the HCO and the coupling properties between the cells.

A PRC quantifies the relationship between the timing of a current stimulus delivered to a neuronal oscillator and the resulting phase shift [Win80]. Phase identifies the location of the oscillator on its limit cycle. To measure the PRC, the neuron must first be at its oscillatory steady state. Then, a small brief depolarizing current pulse is given to the cell at a particular phase which causes a phase shift. This shift is recorded as the phase response of the cell. As a simple example, we consider the phase response properties of the single cell Morris Lecar model (figure 2.3). The phase shift can be seen in figure 2.3A,C,E. In figure 2.3A, the solid blue line is the voltage trajectory of the cell after receiving a brief depolarizing current pulse near time $t = 50$ msec. The blue dotted line is the trajectory that the cell would have taken had it not received a brief current pulse. Figure 2.3C shows

the corresponding phase of the cell. The arrows in 2.3A indicate the timing change that occurred as a result of the stimulus, which is recorded as the change in phase. Figure 2.3E shows this process on the phase circle. Each point on the circle represents a different phase, and as the cell oscillates in time (figure 2.3A), it circulates around the circle repeatedly with a constant velocity [Win80]. The perturbations to measure phase responses are delivered at different times in the cycle, and the resulting phase shifts at each point in the period make up the PRC (figure 2.3F).

To understand how to read a PRC, consider figure 2.3B,D,F. Figure 2.3B shows the voltage trajectory over a single period, and figure 2.3D shows the corresponding phase of the cell. Figure 2.3F is the PRC, showing the sign and magnitude of the phase shift of the cell as a function of the phase that the stimulus is given. Positive phase shifts correspond to phase advances and negative phase shifts to phase delays. If a stimulus arrives just after phase 0, the cell will advance in phase. If a stimulus arrives near phase $T/3$, it will have little-to-no effect on the phase of the cell. If a stimulus arrives near phase $3T/4$, the cell will undergo a relatively large phase delay.

Using different sizes and shapes of stimuli to measure the PRC generates different results. Generating PRCs with small stimuli (in duration and amplitude) approximating a small δ -function pulse and normalizing by the total charge of the stimulus generates the infinitesimal PRC (iPRC). The iPRC can be thought of as the Green's function or impulse response function for the periodically oscillating cell because it describes the reaction of the cell to a small δ -function perturbation. The oscillators receive small perturbations due to coupling. When the perturbations are small enough, they sum approximately linearly, i.e. the total phase response of the oscillator can be found by convolving the perturbation with the iPRC. The iPRC is required for the theory of weakly coupled oscillators [EK90], which is used to determine phase-locked states in chains of oscillators where coupling between oscillators is weak [Neu79] [Kur84], as appears to be the case in the crayfish swimmeret system [SHM09].

iPRCs can also be measured by linearizing the system around the limit cycle solution, solving the adjoint equation, and normalizing [Neu79]. Both methods produce the same result for

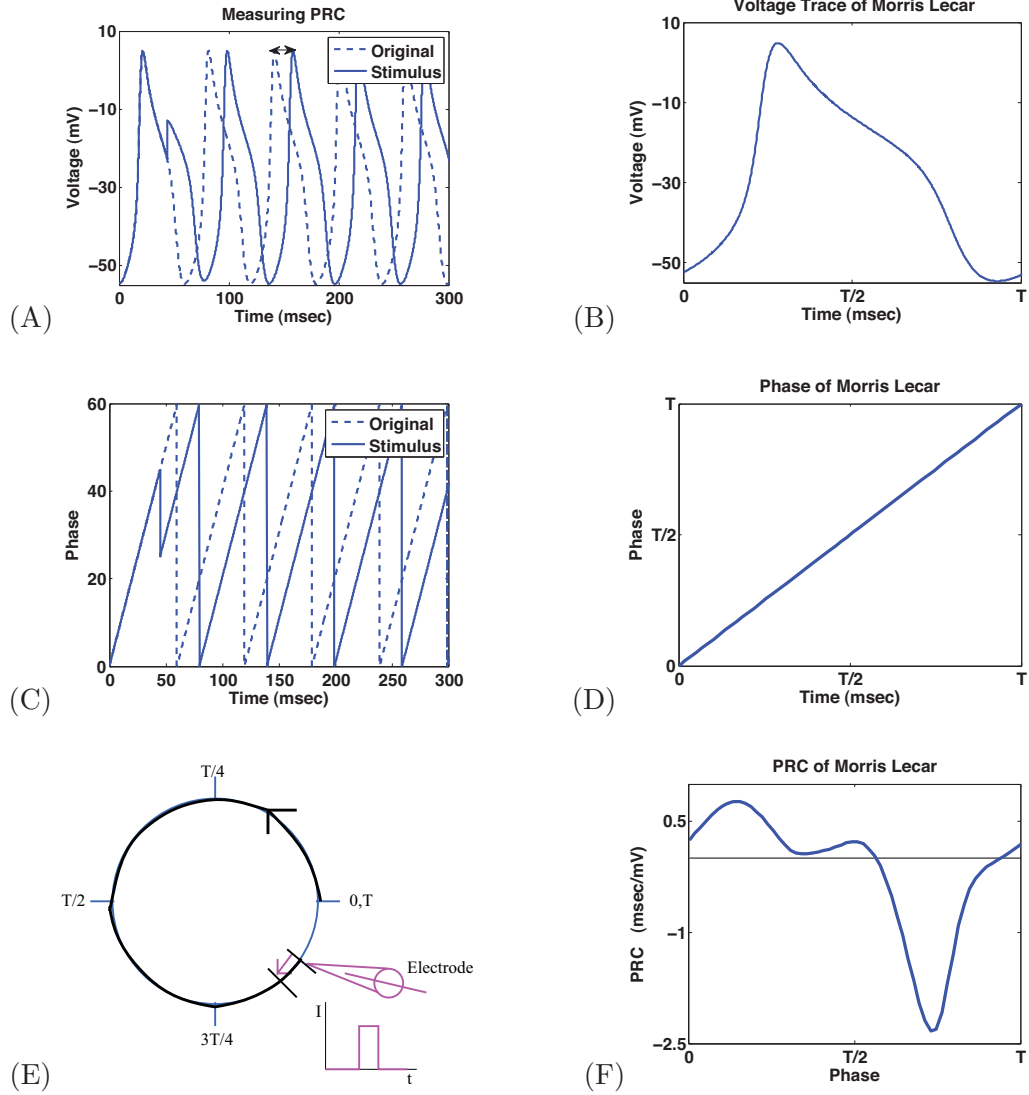


FIGURE 2.3. (A)(C): Example of how to measure PRC. (A) A small pulse is given to the voltage trace to measure the PRC. (C) The corresponding change in phase. (E) The circle represents the phase of the cell. The pink electrode stimulates the cell at various phases, (only one phase is shown). The cell is either advanced or delayed, and this change is recorded as part of the PRC. Small I vs t graph shows a ‘small’ current pulse given to the cell at each phase. (B)(D)(F): Example of PRC for a Morris Lecar cell. (B) Voltage trace over one period, T . (D) The corresponding phase of the cell. (F) The PRC.

sufficiently small, brief perturbations. If the neuronal oscillator model is described by

$$(2.1) \quad \frac{dX}{dt} = F(X)$$

where X is an N -dimensional state variable vector and $F(X)$ is a vector function describing the rate of change of the state variables, then the iPRC is the T -periodic solution to

$$(2.2) \quad \frac{d\bar{z}}{dt} = -DF(X_{LC}(t))^T \bar{z}$$

subject to

$$(2.3) \quad \bar{z}(0) \cdot F(X_{LC}(0)) = 1.$$

The iPRC is the component of the vector \bar{z} corresponding to the voltage V . $DF(X_{LC})$ is the Jacobian of $F(X)$ evaluated along the limit cycle solution $X_{LC}(t)$. In chapter 3 we find the iPRC numerically using the adjoint method [EK91], which is automated in the software package XPPAUT [Erm02].

2.4. Theory of Weakly Coupled Oscillators (TWCO)

The theory of weakly coupled oscillators is often used to predict phase-locking in networks where the coupling between oscillators is relatively weak. In this theory, the phase shifts of small perturbations due to coupling sum approximately linearly, so the evolution of each oscillator can be described by a convolution of the coupling input and the oscillator's iPRC [Kur84] [KE02] (equation (2.5)). This substantially reduces the complexity of the system and allows the analysis of phase-locking to be much more tractable.

Consider two weakly coupled neuronal oscillators with intrinsic periods T . The network equations corresponding to equation (2.1) are

$$(2.4) \quad \frac{dx_i}{dt} = F(x_i) + I_{j,i}(x_j)$$

Let the phase of neuron i at time t be $\phi_i = t + \psi_i(t)$, where $\psi_i(t)$ is relative phase. $z_i(t)$ is the iPRC of oscillator i and is defined by F . $I_{j,i}$ describes the weak coupling from oscillator j to oscillator i . Because the coupling is weak, it only has a small effect on the oscillator in one period, but these effects accumulate over time and can lead to phase-locking. The TWCO uses averaging methods to reduce the dynamics of each oscillator to a single equation describing the evolution of its relative phase (equation (2.5)). Equation (2.5) is an example for which cell i receives input only from cell j .

$$(2.5) \quad \frac{d\psi_i}{dt} = \frac{1}{T} \int_0^T z_i(\tilde{t} + \psi_i) I_{j,i}(X_{LC}(\tilde{t} + \psi_j)) d\tilde{t} = H_i(-\Delta\psi)$$

where $\Delta\psi = \psi_i - \psi_j$. $H_i(-\Delta\psi)$ is interaction function, and X_{LC} is the limit cycle solution to equation (2.4). Steady states of these equations correspond to phase-locked states of the coupled oscillators.

This theory uses singular perturbation methods to separate the properties of the circuit controlling the rhythmic activity in each module (the iPRC of the local oscillators, z) from the properties of the coordinating information arriving from other modules (the coupling between oscillators, $I_{j,i}$), as seen in equation (2.5). We exploit this separation in this thesis. We first study the phase response properties of each segment separately from the coordinating circuitry. We study how the intrinsic properties of HCO cells and coupling determine the phase response properties of the HCO. These properties can be studied separately in the experimental setting, as well [MMC93] [MH07] [SHM09]. We then use the phase response properties of the HCO along with coupling information to determining the phase-locking ability of a chain of HCOs. We use the TWCO in chapter 6 to obtain qualitative insights into intersegmental phase-locking and identify possible biophysical mechanisms underlying coordination.

2.5. Previous modeling work

2.5.1. Phase maintenance and intersegmental circuitry in the crayfish swimmeret system. Several modeling papers have paved the way for future progress towards our goal. Skinner et al. [SKM97] modeled the crayfish swimmeret system as a chain of four phase oscillators with bidirectional nearest neighbor coupling. They only describe the general form of the interaction functions H_{ASC} and H_{DSC} , but include no detail. They tested the ability of this system to maintain a constant phase lag of 25% between each segment despite changes in frequency [BM95]. Using coupled oscillator theory to study phase-locking in the system leads to the following predictions. First, coupling between segments must be asymmetric, but ascending and descending coordinating neurons must have approximately equal strengths. Second, intersegmental coupling must have little effect on the period of the system.

To gain insight into how asymmetric coupling between segments might arise, Skinner & Muloney [SM98b] used extensive numerical simulations of a biophysical model to test which

alternative configurations of intersegmental circuits agreed with experimental results. They modeled the pattern-generating oscillator in each segment with three non-spiking interneurons. Each interneuron was described by Morris-Lecar type equations, which are often used as a ‘minimal’ biophysical model for electrically excitable cells. They modeled the coordinating neurons indirectly with a simple synaptic current injection into their target neurons. They tested seven possible intersegmental circuits for the ability to maintain a 25% phase lag and preserve the relative burst duration over a range of frequencies, and found that only one of the seven configurations worked. They proposed that this configuration is a possible pattern of intersegmental circuitry in the crayfish swimmeret system. Note that in this case they modeled each oscillator with three non-spiking interneurons. The synaptic connections in the proposed intersegmental circuit are not collapsable to a two-cell model. Therefore, this results is not applicable here.

Jones et al. [JMKK03] used the intersegmental circuitry proposed in Skinner et al. [SM98b] to investigate the biophysical mechanisms that help maintain a phase difference of 25% between two segments. They reduced the biophysical model to a phase model using the TWCO. They showed that ascending and/or descending connections are sufficient to maintain 25% phase lag over a range of frequencies due to the shape of their respective H interaction functions, where the H function describes the effect of the connection on the phase of the module. They generated PRCs for input to each of the two coordinating interneurons using the biophysical model introduced in Skinner & Mulloney and compared them to experimentally generated PRCs (stimulating the interneurons and recording the change in phase through the PS motor neuron). The experimental data is consistent with the types of connections predicted by the model.

Similar to Skinner et al., we also use phase models in chapter 6 to study phase locking in a chain of oscillators. However, we use recent knowledge of intersegmental circuitry and strengths to expand the model from nearest neighbor only coupling. More importantly, we don’t use a specific form of H . Instead, we take a step back and get H from the HCO PRC and coupling. This is a step towards a more realistic model.

Both the Skinner & Mulloney [SM98b] and Jones et al. [JMKK03] studies used three interneurons to model the local pattern-generating circuit. However, new evidence suggests that one of these interneurons is actually ComInt1. Furthermore, both studies consider only pairs of HCOs. The intersegmental circuitry and strengths have since been experimentally described [MHH06] [MH07] [SHM09]. We use this knowledge when we study phase-locking between segments in chapter 6. The intrinsic cellular dynamics and synapses from biophysical model modified from Skinner & Mulloney are used in chapter 3 to begin to understand the phase response properties of the HCO. In chapter 6, we consider chains of lengths one through four and show that positive results in a pair of oscillators does not necessarily translate to a larger chain.

2.5.2. PRCs of CPGs and phase-locking between coupled HCOs. Few theoretical studies have explicitly examined how the intrinsic neuronal properties and synaptic dynamics within a network CPG affect the PRC of the CPG or the phase-locking between coupled CPGs [VKH⁺08] [KE09] [JK06]. Perhaps the most relevant work to ours is Ko & Ermentrout [KE09]. In their study, the PRC of a HCO composed of two coupled phase models is obtained in terms of the PRCs of the individual oscillators and the interaction functions H obtained from a phase reduction. They find that the PRC of the HCO has the same qualitative shape as the single cell PRC. This work is similar to our analysis in chapter 4, where we derive the PRC of a phase model HCO, but it differs from our analysis because they measure the PRC of their system by giving weak, instantaneous perturbations to *both* oscillators at the same time. This facilitates analysis of the system. We, however, measure the PRC of the HCO by giving weak, instantaneous perturbations to only one cell. This is a key difference because intersegmental coupling in the crayfish swimmeret system has input into only one cell in the HCO. Therefore, phase-locking predictions from Ko & Ermentrout are not applicable to the crayfish.

The study by Jones & Kopell [JK06] was motivated by Skinner & Mulloney [SM98b] and studied how phase lags are produced between two weakly coupled HCOs. Each HCO is composed of two strongly and reciprocally-coupled relaxation oscillators. The local HCO networks are described using canonical Morris-Lecar type models in the relaxation oscillator limit, and are assumed to be in a stable anti-phase state. The weak coupling between

the HCOs is unidirectional, instantaneous, and can have either inhibitory or excitatory effects. Using geometric singular perturbation theory, they find that the time constant of the inhibition in the local network can affect the phase lag between HCOs without changing the phase lag between the two cells within the HCO. However, in chapter 6 when we study phase locking between networks, we use the TWCO rather than geometric singular perturbation theory and focus on how shapes of the PRCs of the local networks and intersegmental coupling affect the phase lag between HCOs, rather than intrinsic parameters in model for the single cells of the local network. Specifically, as a step towards a more realistic model, we use bidirectional intersegmental coupling, a chain of up to four HCOs, and do not use relaxation oscillators in the HCO.

2.5.3. Coupled oscillator work in lamprey. Many papers study the mechanisms underlying intersegmental coordination and phase lag in the lamprey locomotor system. Locomotion in the lamprey is produced by alternating activation of muscles on opposite sides of the body with a rostral-to-caudal delay. This generates a wave of curvature down the length the lamprey with a wavelength of approximately one body length. The lamprey has approximately 100 body segments, and the spinal cord produces a constant intersegmental phase lag of 1% despite changes in frequency [WW84]. There is a large collection of work by Williams & Sigvardt et al., Buchanan and coworkers, Ermentrout & Kopell, Cohen et al. (e.g. [SW96] and references therein). They combine theory and experiments to investigate the mechanisms underlying intersegmental coordination. In these papers, the lamprey CPG is modeled as a chain of coupled phase oscillators each described by an intrinsic frequency and nearest neighbor interaction functions H . Experimentally, ventral root recordings are performed during fictive locomotion [WSK⁺90] [WS94] and sometimes in split-bath preparations to study the effects of unequal activation [Sig93] [SW96]. The model is tailored by experimental results, and a variant of the model is developed for which variables can be experimentally measured [Wil92b] [WS95]. Mathematical analysis predicted that asymmetric coupling is dominant in determining the intersegmental phase lag, but that descending coupling is dominant in determining the frequency of the coupled oscillators [WSK⁺90] [Wil92b] [Wil92a] [WS95] [SW96]. Experiments confirmed these predictions [Sig93] [SW96]. Analysis also predicted the existence of a boundary region in the

rostral end of the chain where the phase lag differs from the rest of the cord [Wil92b], and experiments confirmed this prediction [WS94]. These studies provide a framework that is useful for gaining insights into the mechanisms underlying intersegmental phase lag and phase maintenance in the crayfish swimmeret system. We use similar tactics of combining theory and experiments, as the modeling and analysis in chapters 3-6 are motivated by experimental results. We also apply the TWCO to begin to understand phase maintenance in a chain of oscillators and generate experimentally testable predictions. Specifically, these studies begin with the interaction function H and combine CPGs in a long chain with nearest neighbor coupling. As previously mentioned, we take a step towards a more realistic model by studying the phase response properties of the oscillators and generating H from the HCO PRC and coupling.

2.6. Aims of Part 1

The goal of this project is to use mathematical modeling and analysis to develop a greater understanding of the mechanisms underlying phase maintenance in the crayfish swimmeret system. The TWCO (section 2.4) uses singular perturbation methods to separate the response properties of the circuit controlling each module (in terms of the PRC of the local oscillators) from the properties of the coordinating information arriving from other modules (the coupling between oscillators). These properties can be studied separately in the experimental setting, as well [MMC93] [MH07] [SHM09]. We utilize this separation to understand phase maintenance in two steps. First, we study the phase response properties of models of the local CPGs in a single segment (figure 2.2B). Second, with a description of the connectivity between segments stemming from experiments, we use the TWCO to begin to understand which PRC shapes of the CPGs and connectivity properties might play a role in phase maintenance (chapter 6). We look at how the duty cycle of intersegmental coupling, as well as the shape of the HCO PRC effect phase locking.

To study the phase response properties of the local CPG, we connect two non-spiking local interneurons via inhibitory synapses. The cells and their synapses form a half-center oscillator (HCO) with one cell active while the other is suppressed and vice versa. We treat the entire HCO as a ‘single oscillatory unit’ and examine the phase response curve (PRC)

of the HCO in terms of the PRC of the individual cells and the synaptic properties between the cells. We use a Morris-Lecar model (chapter 3), phase models (chapter 4), and the leaky integrate-and-fire model (chapter 5) to describe the single cells within the HCO.

As part of the analysis of HCOs, we examine the bifurcation structure of the phase model HCO using the strength of coupling between cells within the HCO as the bifurcation parameter (chapter 7). Diagrams for both δ -function pulse coupling and current-based exponential synapses are studied. Standard δ -pulse coupling is often used in phase models as an approximation to very fast current-based synapses [KE09] [GE02]. We demonstrate that this is not a good approximation. We show that when the appropriate limit to a delta-function is taken, a new δ -pulse coupling function can be derived that provides a good approximation to current-based exponential synapses with small time constants.

CHAPTER 3

Phase Response Properties of Half-Center Oscillators using Morris-Lecar Intrinsic Dynamics

The goal of this chapter is to begin to explore how the phase response properties of HCOs are determined from the intrinsic cellular properties and synaptic properties within the HCO. We use a modified version of the Morris-Lecar network model of the crayfish central pattern generator (CPG) from Jones et al. [JMKK03] [SM98b]. In the original model of Jones et al., there were three local interneurons forming the CPG: cells 1A, 1B, and 2. Here, we use only two local interneurons, cells 1 and 2, when modeling the HCO. In our model, the cells in the HCO are identical and coupling is symmetric. We are most interested in anti-phase behavior in the HCO case because the HCO in the crayfish swimmeret system operates in anti-phase.

In addition to exploring the phase response properties of HCOs, we also examine a single cell and a single cell with an autapse (figure 3.1). This chapter compares the PRCs of each case and examines how changing various parameters lead to changes in the PRCs. The aim is to highlight the fact that understanding how these changes come about is very

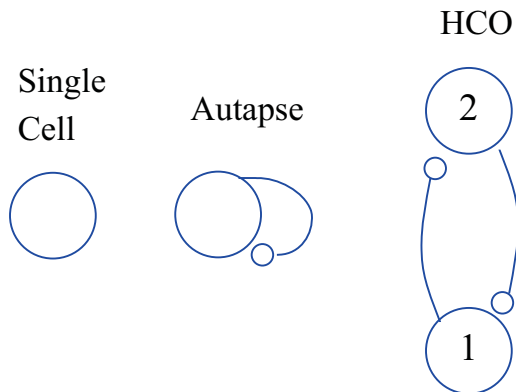


FIGURE 3.1. Three cases analyzed in this chapter. Right to left: Single cell, single cell with inhibitory autapse, two identical cells coupled with reciprocal inhibition.

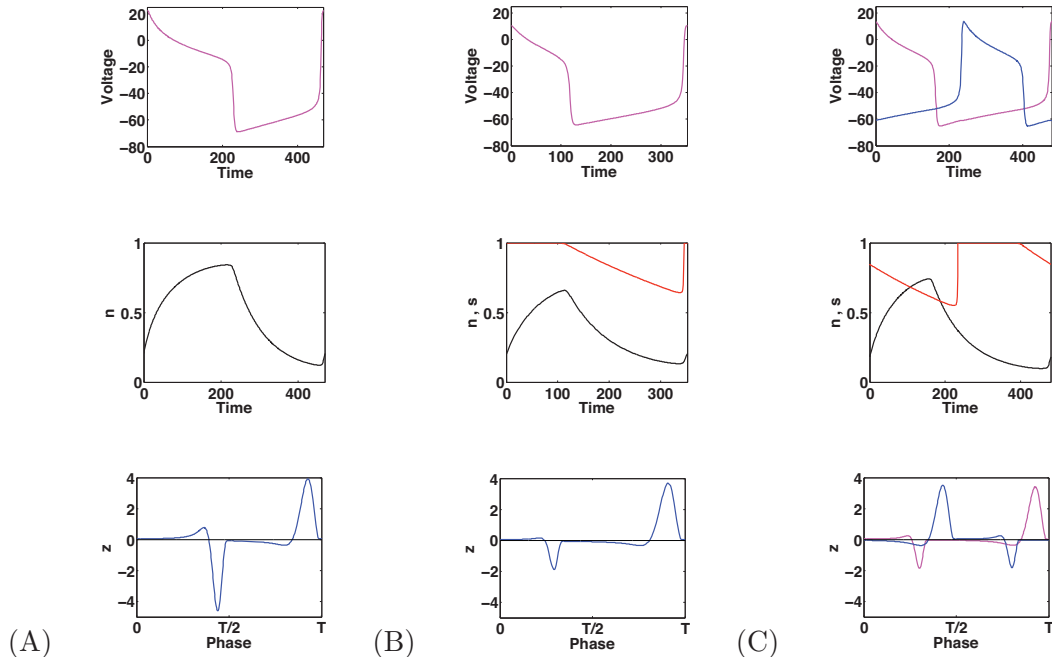


FIGURE 3.2. Comparing the three cases in figure 3.1 using the Morris-Lecar model and parameters from Jones et al. [JMKK03] with the exception of g_{syn} . Here, $g_{syn} = .1$. $I_{app} = 1$ for autapse and HCO. $I_{app} = 0$ for single cell. Membrane potential has units mV, n and s are in arbitrary units, and the PRCs have units msec/mV. (A) Single Cell. Top to bottom: Single cell voltage trace, n , PRC for single cell. (B) Autapse. Top to bottom: Single cell with autapse voltage trace, n (black) and s (red), PRC for single cell with autapse. (C) HCO. Top to bottom: Voltage trace of cell 1 (pink) and cell 2 (blue) in HCO, n (black) and s (red) for cell 1, PRC of HCO when measured by stimulating cell 1 (pink) and cell 2 (blue).

complicated. We do this through a series of examples. In each example, parameters are altered and the resulting PRCs are compared.

In this chapter, the PRCs are computed in XPPAUT [Erm02] using the adjoint method, i.e. they are the iPRCs, but one can think of them as being computed by stimulating cell 1 or cell 2, with brief small current pulses. Initially, all parameters are taken to be the same as in Jones et al. except the local synaptic conductance, which is taken to be 0.1 mS/cm^2 rather than 0.5 mS/cm^2 . This change is made to counter the effect of going from a three-cell interneuron circuit to a two-cell circuit.

The Jones et al. study uses weakly coupled oscillator theory to derive interaction functions that predict phase differences between neurons in neighboring segments. They study how phase differences are effected by changes in frequency, intersegmental coupling strength, and intersegmental coupling pattern. To compare the interaction functions in Jones et al.

with the PRCs presented here, one must convolve the PRCs with the synaptic waveform used in Jones et al.

The dynamics of the isolated cells in each case (the single cell, the single cell with an autapse, and the HCO) are modeled by a Morris-Lecar model containing two variables: membrane potential (V) and the fraction of open potassium channels (n). The time constants in the Jones et al. model dictate that the evolution of n is much slower than V , putting the single cell in the relaxation oscillator regime. As the parameter controlling the time constant for n (ϵ_1) is increased, the cells move out of the relaxation regime and into a smoother oscillation that more closely resembles the voltage profiles seen in the crayfish non-spiking interneurons. In the case of the HCO and the single cell with the autapse, the synapses are described by a conductance-based model. The synaptic gating variable s is modeled to activate quickly when the presynaptic membrane potential is above a certain threshold, and decay slowly when the presynaptic membrane potential is below the same threshold. See the appendix for a full description of the model.

Figure 3.2 compares the PRCs for each case in figure 3.1 using the parameters given in Jones et al. (except for g_{syn}). These parameters allow the cell to oscillate on its own without applied current. Column (A) in figure 3.2 shows the voltage (upper), fraction of open potassium channels n (middle, black), and PRC (bottom) for one period in the single cell. Column (B) shows the same for the single cell with the autapse. The middle panel in (B) also plots the synaptic activation variable s (red). Column (C) shows the same for the HCO. The top panel in (C) plots the voltage for cell 1 (pink) and cell 2 (blue). The bottom panel in (C) plots the PRC of the HCO with respect to cell 1 (pink) and cell 2 (blue), i.e. the PRC corresponding to stimulating cell 1 or cell 2, respectively. When the HCO is in anti-phase, stimulating cell 2 produces an identical PRC to cell 1 shifted by one-half of the period because the HCO is symmetric. Each figure in this chapter is organized in a similar manner to figure 3.2.

For the default parameters, the qualitative shape of the PRCs are similar for each case (bottom row of figure 3.2). They each begin with an interval of small phase advances followed immediately by a large negative lobe (referred to as the ‘delay lobe’). The delay

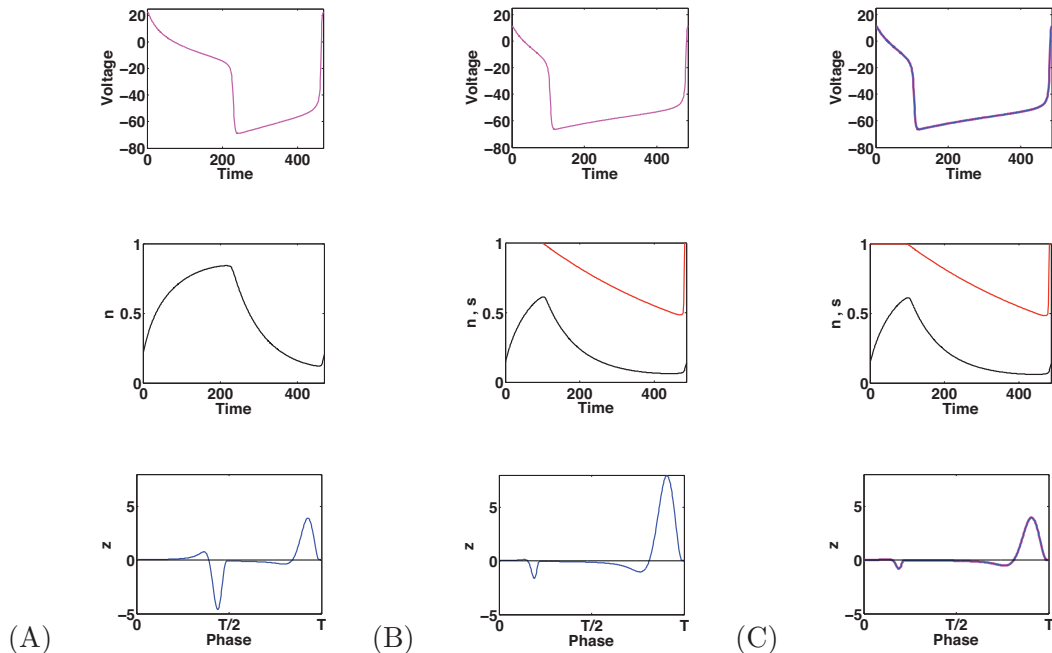


FIGURE 3.3. Effect of decreasing the applied current in the Morris-Lecar model. $I_{app} = 0$ for all three cases. Membrane potential has units mV, n and s are in arbitrary units, and the PRCs have units msec/mV. (A) Single Cell. Top to bottom: Single cell voltage trace, PRC for single cell. (B) Autapse. Top to bottom: Single cell with autapse voltage trace, n (black) and s (red), PRC for single cell with autapse. (C) HCO. Top to bottom: Voltage trace of cell 1 (pink) and cell 2 (blue) in HCO, n (black) and s (red) for cell 1, PRC of HCO when measured by stimulating cell 1 (pink) and cell 2 (blue).

lobe corresponds to the phase around which the voltage ‘jumps down’ to the hyperpolarized state. The delay lobe is followed by a period of small phase delays and then a large positive lobe (referred to as the ‘advance lobe’). The advance lobe corresponds to the phase around which the voltage ‘jumps up’ to the depolarized state. The delay lobe for the single cell PRC occurs later in the period than in the other cases (bottom of A versus bottom of B and C). Also, the delay lobe of the single cell PRC is larger in magnitude than the advance lobe. The opposite is true for the single cell with the autapse and the HCO. However, the magnitude of the advance lobe is similar for all three cases.

The period of each case varies, as well. The single cell and HCO periods are similar, whereas the period of the single cell with the autapse is significantly smaller. Because the applied current is 0 nA for the single cell case and 1 nA for the other two cases, the exact reason for the similarities and differences in the period between the three cases is difficult to understand [SKM94] [DRR09]. Furthermore, it is unclear how valid it is to compare the

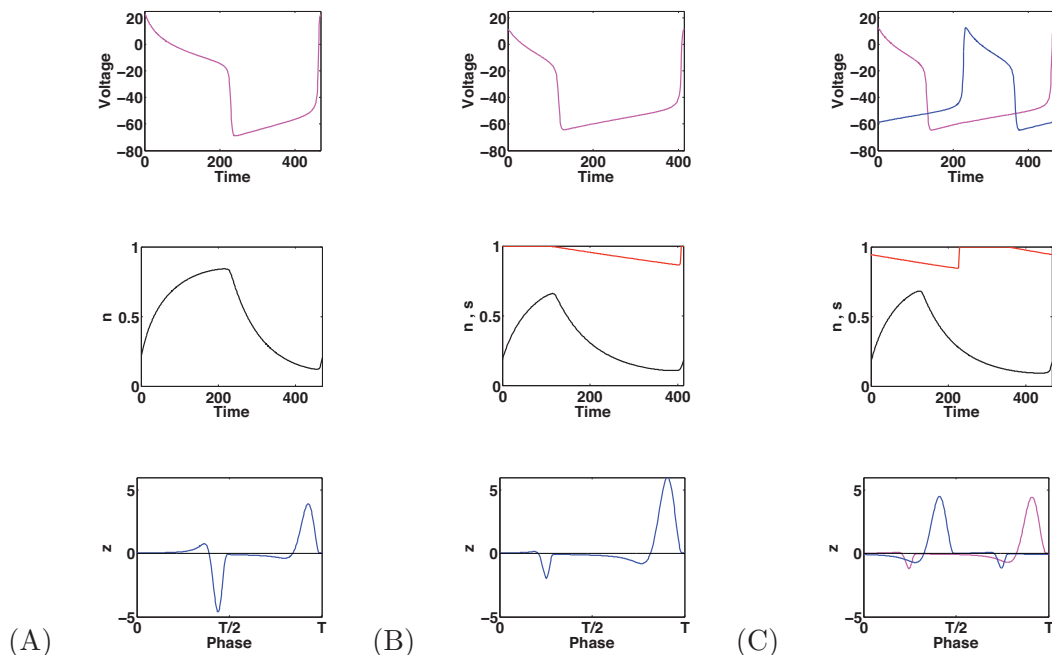


FIGURE 3.4. Effect of increasing the synaptic time constant (slow synaptic decay) in the autapse and HCO. $\epsilon_2 = .0015$. Membrane potential has units mV, n and s are in arbitrary units, and the PRCs have units msec/mV. (A) Single Cell. Top to bottom: Single cell voltage trace, n , PRC for single cell. (B) Autapse. Top to bottom: Single cell with autapse voltage trace, n (black) and s (red), PRC for single cell with autapse. (C) HCO. Top to bottom: Voltage trace of cell 1 (pink) and cell 2 (blue) in HCO, n (black) and s (red) for cell 1, PRC of HCO when measured by stimulating cell 1 (pink) and cell 2 (blue).

single cell PRC to the other two considering the difference in applied current. However, if the single cell received 1 nA of applied current, it would not oscillate. These factors compound the difficulty in pinpointing the cause for any differences.

Figure 3.3 compares the PRCs of each case when the injected current (I_{app}) is set to 0 nA for the autapse and HCO cases. It should be noted that initially the single cell has an injected current of 0 nA and the autapse and two-cell network have an injected current of 1 nA. If the single cell receives an injected current of 1 nA, it enters depolarization block and does not oscillate. When $I_{app} = 0$ nA, the HCO quickly converges to synchronous behavior rather than anti-phase. The synchronous behavior displayed here is contrary to intuition that inhibitory synapses lead to anti-synchrony behavior. It has been shown that inhibitory synapses that decay sufficiently slowly can lead to synchrony [VVAE94] [TKB98] [WR92]. However, the rate of decay has not changed here and the period has changed very little. A noticeable difference is that the duty cycle of the autapse and HCO oscillations

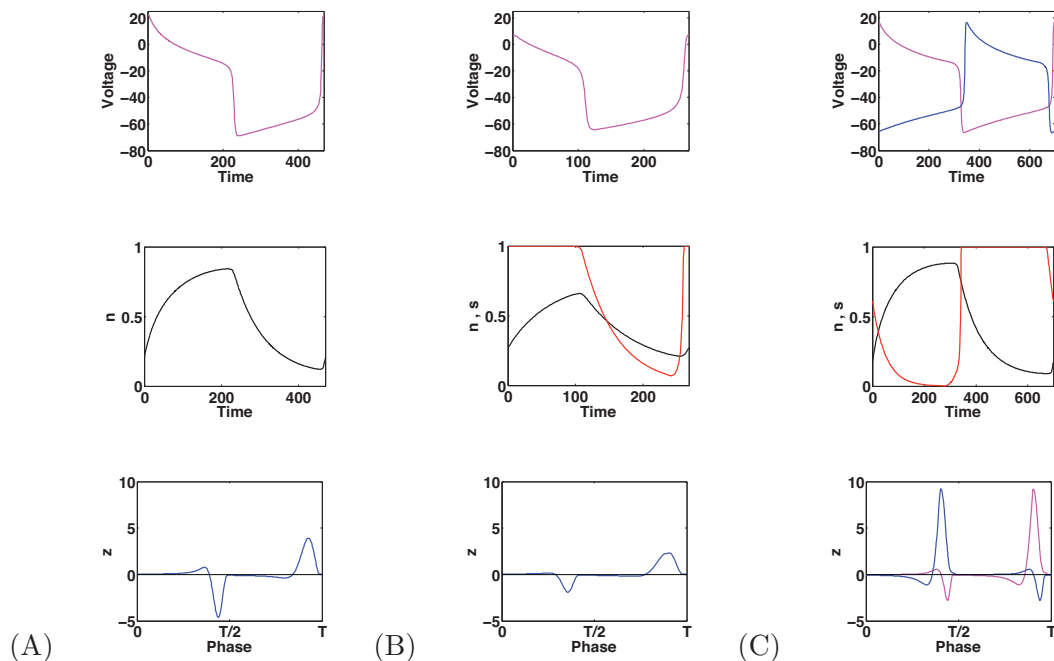


FIGURE 3.5. Effect of decreasing the synaptic time constant (fast synaptic decay) in the autapse and HCO. $\epsilon_2 = .06$. Membrane potential has units mV, n and s are in arbitrary units, and the PRCs have units msec/mV. (A) Single cell. Top to bottom: Single cell voltage trace, n , and s for single cell. (B) Autapse. Top to bottom: Single cell with autapse voltage trace, n (black) and s (red), PRC for single cell with autapse. (C) HCO. Top to bottom: Voltage trace of cell 1 (pink) and cell 2 (blue) in HCO, n (black) and s (red) for cell 1, PRC of HCO when measured by stimulating cell 1 (pink) and cell 2 (blue).

are significantly shorter. This allows the synaptic activation variable s to reach a lower minimum, which might play into why the HCO is synchronous. The HCO and single cell periods are very similar to the default parameter case. However, the period of the single cell with the autapse is now identical (486 msec) to the HCO. Furthermore, the PRC for the single cell with the autapse has exactly twice the amplitude of the HCO PRC. As in figure 3.2, the autapse and HCO PRCs are qualitatively similar to the single cell PRC, with differences in magnitude and location of the advance and delay lobes.

Figures 3.4, 3.5, and 3.6 study how altering the decay rate of the synapse affects the PRCs. Figure 3.4 compares the PRCs of each case when the synaptic time constant is increased ($\epsilon_2 = .0015$), causing the synapses to decay more slowly. Figure 3.5 compares the PRCs of each case when the synaptic time constant is decreased ($\epsilon_2 = .06$), causing the synapses to decay very quickly. When the synapses are slower (figure 3.4), the period in all three cases is similar. With faster synapses (figure 3.5), the period of the single cell with the autapse is

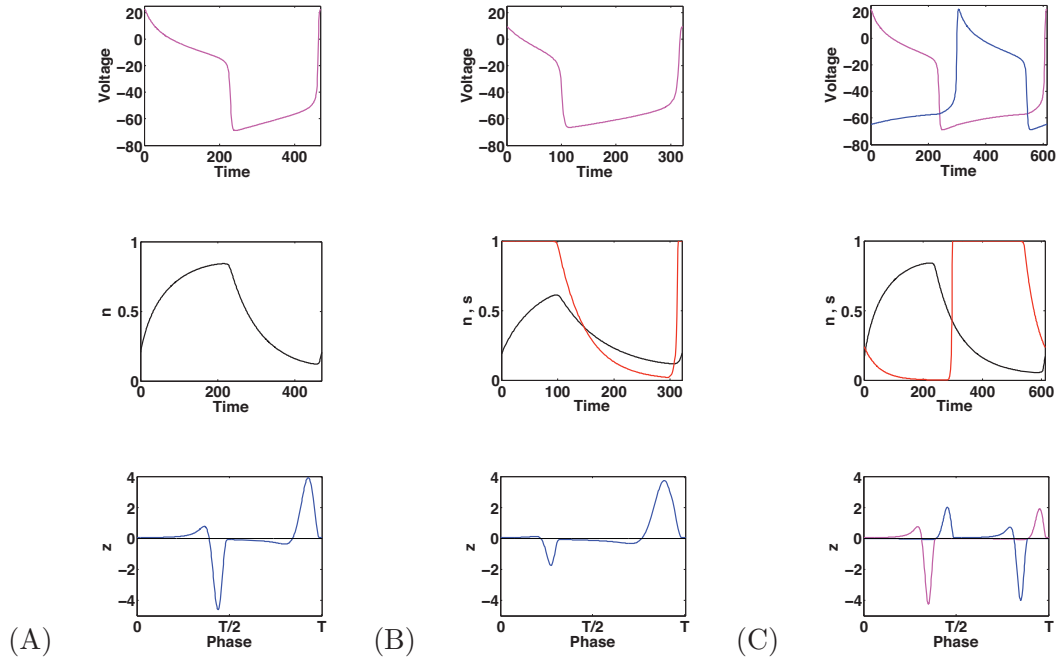


FIGURE 3.6. Effect of decreasing the synaptic time constant and decreasing the applied current in the autapse and HCO. $\epsilon_2 = .06$. $I_{app} = 0$. Membrane potential has units mV, n and s are in arbitrary units, and the PRCs have units msec/mV. (A) Single cell. Top to bottom: Single cell voltage trace, n , PRC for single cell. (B) Autapse. Top to bottom: Single cell voltage trace, n (black) and s (red), PRC for single cell with autapse. (C) HCO. Top to bottom: Voltage trace of cell 1 (pink) and cell 2 (blue) in HCO, n (black) and s (red) for cell 1, PRC of HCO when measured by stimulating cell 1 (pink) and cell 2 (blue).

much smaller than the single cell, and the period of the HCO is much larger than the single cell. Comparing the duty cycles in each figure, the autapse and HCO duty cycles are smaller when the synapse is slower. However, the qualitative shapes of the PRCs and voltage traces are very similar in both figures for all cases, and are similar to the default parameters (figure 3.2). Thus, the qualitative shape of the PRCs are not sensitive to changes in the synaptic time constant for these parameters, despite the significant change in behavior of the synaptic activation variable.

Figure 3.6 compares the PRCs of each case when the rate constant of the synaptic current is decreased ($\epsilon_2 = 0.06$) and the injected current is decreased ($I_{app} = 0$ nA). As in figure 3.5, decreasing ϵ_2 causes faster synaptic decay. Here, the HCO is near anti-synchrony, i.e. the cells are not in exact anti-phase, but they are close to it. The period of the autapse and HCO are similar to figure 3.5, but the duty cycles are slightly decreased. The qualitative shape of the PRCs for the autapse and HCO are also similar to figure 3.5, however the PRC

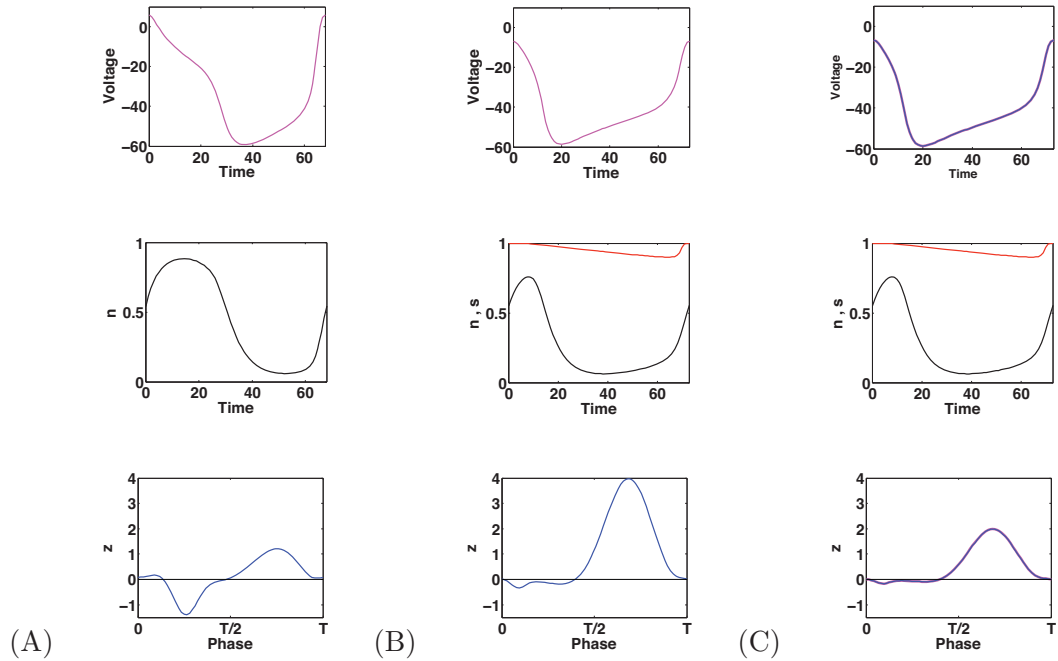


FIGURE 3.7. Effect of increasing the rate constant of the potassium current in the Morris-Lecar model for all three cases. $\epsilon_1 = .1$. Membrane potential has units mV, n and s are in arbitrary units, and the PRCs have units msec/mV. (A) Single cell. Top to bottom: Single cell voltage trace, n , PRC for single cell. (B) Autapse. Top to bottom: Single cell with autapse voltage trace, n (black) and s (red), PRC for single cell with autapse. (C) HCO. Top to bottom: Voltage trace of cell 1 (pink) and cell 2 (blue) in HCO, n (black) and s (red) for cell 1, PRC of HCO when measured by stimulating cell 1 (pink) and cell 2 (blue).

of the HCO now displays opposite magnitudes for the delay and advance lobes. In figure 3.5, the delay lobe in the PRC of the HCO was significantly smaller in magnitude than the advance lobe. The opposite is true in figure 3.6. This demonstrates that altering the synaptic time constant can sometimes have a significant effect on the PRC.

Figure 3.7 compares the PRCs of each case when the rate constant of the potassium current is increased ($\epsilon_1 = 0.1$). This change is made to obtain a smoother oscillation that more closely resembles what is seen in the crayfish non-spiking interneurons. Again, we see that the cells in the HCO converge to synchrony. The PRCs for all three cases are ‘broader’ than in the previous figures. The magnitude of the PRC for the autapse is exactly twice that of the HCO. Both PRCs are qualitatively similar, and significantly different from the single cell PRC. The PRCs for the autapse and HCO have broad small delay lobes and broad large advance lobes, whereas the delay and advance lobes in the single cell PRC are

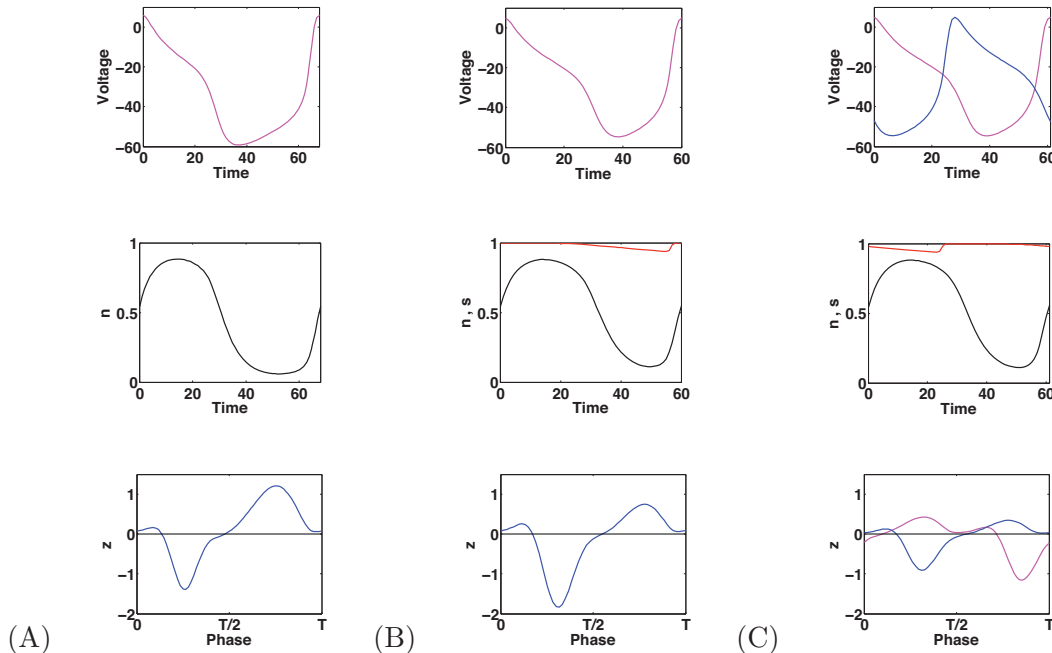


FIGURE 3.8. Effect of increasing the rate constant of the potassium current in the Morris-Lecar model in all three cases and decreasing the synaptic conductance in the autapse and HCO. $\epsilon_1 = .1$. $g_{syn} = .02$. Membrane potential has units mV, n and s are in arbitrary units, and the PRCs have units msec/mV. (A) Single cell. Top to bottom: Single cell voltage trace, n , PRC for single cell. (B) Autapse. Top to bottom: Single cell with autapse voltage trace, n (black) and s (red), PRC for single cell with autapse. (C) HCO. Top to bottom: Voltage trace of cell 1 (pink) and cell 2 (blue) in HCO, n (black) and s (red) for cell 1, PRC of HCO when measured by stimulating cell 1 (pink) and cell 2 (blue).

of similar magnitude. Also, compared to default parameters (figure 3.2), the period for all three cases is significantly smaller.

Figure 3.8 compares the PRCs of each case when the rate constant of the potassium current is increased ($\epsilon_1 = 0.1$) and the synaptic conductance is decreased ($g_{syn} = 0.02$). With the addition of decreased coupling, the HCO returns to near anti-phase. Of note is that the duty cycle for the autapse and HCO cases is very different between figures 3.7 and 3.8. The period for the autapse and HCO cases are slightly smaller than in figure 3.7, but are still very different from default (figure 3.2). However, in figure 3.8 the delay lobes in the PRCs for the autapse and HCO are larger than the advance lobes, which is opposite to figure 3.7. The PRC found from stimulating either cell is shown in the bottom panel of figure 3.8C. If the HCO were in true anti-phase, the PRCs would be shifted versions of each other. However, here we see that the PRC of the HCO is larger in magnitude when generated by

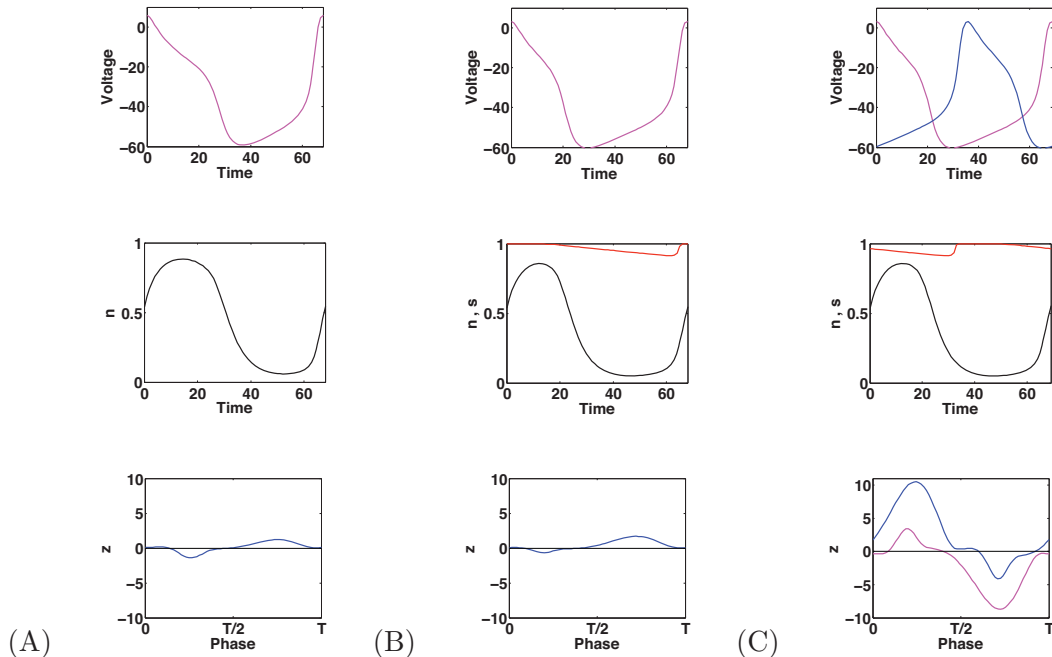


FIGURE 3.9. Effect of increasing the rate constant of the potassium current in the Morris-Lecar model, and decreasing the synaptic conductance and applied current in the autapse and HCO. $\epsilon_1 = .1$. $g_{syn} = .02$. $I_{app} = 0$. Membrane potential has units mV, n and s are in arbitrary units, and the PRCs have units msec/mV. (A) Single cell. Top to bottom: Single cell voltage trace, n , PRC for single cell. (B) Autapse. Top to bottom: Single cell with autapse voltage trace, n (black) and s (red), PRC for single cell with autapse. (C) HCO. Top to bottom: Voltage trace of cell 1 (pink) and cell 2 (blue) in HCO, n (black) and s (red) for cell 1, PRC of HCO when measured by stimulating cell 1 (pink) and cell 2 (blue).

stimulating cell 2 (dark gray line) compared to when the PRC is generated by stimulating cell 1 (light gray line).

Figure 3.9 compares the PRCs of each case when the rate constant of the potassium current is increased ($\epsilon_1 = 0.1$), the synaptic conductance is decreased ($g_{syn} = 0.02$), and the injected current is decreased ($I_{app} = 0$ mV). As in figure 3.8, the HCO displays near anti-synchrony behavior and the period for all three cases are similar to figure 3.8. However, there are big differences between the PRC for the single cell with the autapse and the HCO. The PRC of the single cell with the autapse has a small delay lobe followed by a large advance lobe. But when the PRC of the HCO is generated by stimulating cell 1 (light gray line), it has a small advance lobe followed by a large delay lobe. The PRC of the HCO found by stimulating cell 2 (dark gray line) is not simply a shift by one-half period. It has a large advance lobe followed by a small delay lobe. In other words, the PRC derived from stimulating cell 2

(dark gray line) is a reflected (over the x-axis) and shifted version of the PRC derived from stimulating cell 1 (light gray line). If the cells were in true anti-synchrony, the two PRCs would simply be shifted by one-half of the period. Furthermore, the PRC of the HCO has a significantly larger magnitude than that for the single cell with the autapse and the single cell.

3.1. Summary

This chapter demonstrates how various parameters in a biophysical model can alter the PRC of the HCO in a seemingly unpredictable manner. For example, increasing the rate constant of the potassium current (figure 3.7) caused the cells in the HCO to oscillate synchronously and caused the advance and delay lobes of the PRCs to broaden and change in magnitude. Identifying the cause of these differences is a difficult task because there are numerous variables, parameters, and time scales to consider. In order to build a framework for understanding these results, chapters 4 and 5 examine analytically tractable models. Chapter 4 uses phase models and chapter 5 uses leaky integrate-and-fire models for the single cells. The coupling between the cells is either instantaneous or current-based with fast decay times. The analysis in each chapter provides insight into how the PRC of a HCO is determined from the single cell PRCs and the coupling between the cells.

CHAPTER 4

Phase Response Properties of Half-Center Oscillators using Phase Models

The previous chapter highlighted the difficulty in understanding how the phase response properties of a HCO arise from the single cell properties and synaptic dynamics even when relatively simple biophysical models are used. In this chapter, we use an idealized model for the intrinsic dynamics of cells within the HCO, which allows us to derive and analyze an analytic expression for the PRC of the HCO. From this, we can begin to see directly how the single cell and synaptic properties influence the PRC of the HCO [KE09]. Specifically, each cell is described by only its phase and its PRC. The synapses between cells are modeled by exponential current-based synapses in the limiting case of very fast synapses.

4.1. The HCO phase model

The dynamics of each cell within the HCO are described with a single equation defining the evolution of the phase of the cell during oscillations and its response to input. The state of each cell is completely described by its phase in the oscillation $\phi \in [0, T]$, where T is the intrinsic period of the cell. The response of the individual cells to input is given in a phase dependent manner as prescribed by their PRC, $z(\phi)$. The cells are coupled by inhibitory exponential synapses [VVAE94]. When a cell reaches phase $\phi = T$, it “fires” and elicits a synaptic current in the postsynaptic cell. The equations governing the HCO phase model

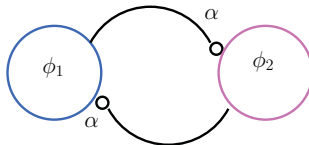


FIGURE 4.1. Idealized HCO phase model. Two cells described only by their phases ϕ_1 and ϕ_2 are coupled through reciprocal inhibitory synapses of strength α .

are

$$(4.1) \quad \begin{aligned} \frac{d\phi_1}{dt} &= 1 - \alpha s_2(t) z(\phi_1(t)) && \text{if } \phi_1 = T, \phi_1 \rightarrow 0 \\ \frac{d\phi_2}{dt} &= 1 - \alpha s_1(t) z(\phi_2(t)) && \text{if } \phi_2 = T, \phi_2 \rightarrow 0 \\ \frac{ds_1}{dt} &= \frac{-s_1}{\tau} && \text{if } \phi_1 = T, s_1 = s_1 + (1/\tau) \\ \frac{ds_2}{dt} &= \frac{-s_2}{\tau} && \text{if } \phi_2 = T, s_2 = s_2 + (1/\tau) \end{aligned}$$

where ϕ_i is the phase of cell i . The term $\alpha s_i(t)$ is the synaptic current, where α is the synaptic strength and $s_i(t)$ describes the synaptic waveform. If $\alpha > 0$, the synapse is inhibitory; if $\alpha < 0$, the synapse is excitatory. In this chapter, we consider only inhibitory synapses ($\alpha > 0$). The parameter τ describes the rate of decay of the synaptic current. Each cell is assumed to have an identical PRC, $z(\phi_i)$. Note that we can prescribe any PRC $z(\phi)$ to the cells. Figure 4.2 shows an example of the dynamics in this model. The phase of each cell (top) and the synaptic current generated by each cell are plotted as functions of time (bottom).

4.1.1. Reduction to appropriately capture the effects of exponential synapses using δ -function synapses. Even though this is an idealized model, it is still difficult to analyze because it is 4-dimensional and non-linear. We simplify the model by using instantaneous synapses so that the effects of every inhibitory post-synaptic current (IPSC) results in an instantaneous jump in phase. However, simply replacing the synaptic conductance ($s(t)$) with a standard δ -function, as discussed in chapter 7, causes a discontinuity in time where only the phase response of the cell at the time of the pulse is accounted for and all other phases are ignored. Exponential synapses do not do this. Therefore, we systematically reduce the model by approximating the synaptic coupling term ($\alpha s(t)z(\phi(t))$) with a new function in the case where the time constant for decay is very small, i.e. the synapses are very fast ($\tau \ll T$). When $\tau \ll T$, $s_j(t) = \frac{1}{\tau} e^{-t/\tau} \gg 1$ ($j = 1, 2$) on the short time scale (when $t \ll \tau$). This is a reasonable approximation because $\tau \ll T$ indicates that the synapses decay very fast, and there is little-to-no synaptic conductance remaining at larger values of t . If α and $z(\phi)$ are such that $\alpha s(t)z(\phi(t)) \gg 1$ when $t \ll \tau$, we can approximate $\frac{d\phi_i}{dt}$ by

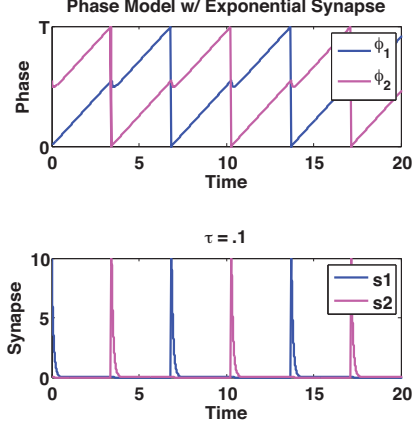


FIGURE 4.2. Phase and synaptic conductance of cells 1 and 2 over time. $T = 2\pi$. $\alpha = 1$. $\tau = 0.1$. $z(\phi) = -\sin(\phi)$. (Top) Two phase oscillators in anti-phase. (Bottom) The synaptic conductance triggered when each cell fires and is reset.

$$(4.2) \quad \frac{d\phi_i}{dt} \approx -\alpha s(t) z(\phi_i(t)) = -\frac{\alpha}{\tau} e^{-t/\tau} z(\phi_i(t)).$$

Let ϕ_i^0 be the phase of cell i when a synaptic current is delivered to it, and let $\phi_i + \Delta\phi$ be the phase of cell i when the synaptic current is approximately zero. Integrating the differential equation in (4.2),

$$(4.3) \quad \int_{\phi_i^0}^{\phi_i^0 + \Delta\phi} \frac{d\phi}{z(\phi)} \approx -\frac{\alpha}{\tau} \int_0^\infty e^{-t/\tau} dt.$$

We can integrate to infinity on the right-hand side because we are considering very fast decay, so the exponential decays to zero almost immediately. The right-hand side integrates to $-\alpha$,

$$(4.4) \quad \int_{\phi_i^0}^{\phi_i^0 + \Delta\phi} \frac{d\phi}{z(\phi)} \approx -\alpha.$$

Let $Z(\phi)$ be the antiderivative of $\frac{1}{z(\phi)}$, then

$$(4.5) \quad Z(\phi_i^0 + \Delta\phi) - Z(\phi_i^0) \approx -\alpha.$$

By solving the nonlinear algebraic equation (4.5) for $\Delta\phi(\phi_i^0)$, we obtain a phase response curve for fast synaptic input, i.e. the phase shifts caused by a current of strength α delivered at a particular phase ϕ . We call $\Delta\phi(\phi)$ the synaptic phase response curve. Note that as $\alpha \rightarrow 0$, $\Delta\phi(\phi) \rightarrow -\alpha z(\phi)$. In this reduction, we explicitly use exponential synapses, but the reduction is identical for any synaptic current that is delivered sufficiently fast. That

is, the reduction does not depend on the shape of the input, it only depends on the total charge and the assumption that the input decays very fast.

The above argument reduces system (4.1) to the δ -pulse-coupled HCO phase model

$$(4.6) \quad \begin{aligned} \frac{d\phi_1}{dt} &= 1 + \delta(\phi_2)\Delta\phi(\phi_1) \\ \frac{d\phi_2}{dt} &= 1 + \delta(\phi_1)\Delta\phi(\phi_2). \end{aligned}$$

The dynamics of this system are as follows. The phase of each cell increases linearly according to its intrinsic dynamics $\frac{d\phi_1}{dt} = \frac{d\phi_2}{dt} = 1$ until the phase of cell i reaches T . At this time, cell i is reset to 0 and an instantaneous pulse of strength α is delivered to cell j . The phase of cell j is immediately shifted by $\Delta\phi(\phi_j)$.

The relative simplicity of the δ -pulse-coupled HCO allows us to analytically derive its PRC. The following sections define a firing map for the model. The PRC is derived by giving small perturbations to one of the cells at various times throughout its cycle and finding the next firing time in the HCO. This firing time can then be used as an initial condition for the firing time map, which determines each subsequent firing time of the cells in the HCO. The differences between the firing times in the perturbed and unperturbed systems yields the PRC for the HCO.

4.2. Derivation of map for firing times

Using the δ -pulse-coupled HCO phase model (system (4.6)), we derive a map to describe the phase of cell 1 when cell 2 fires and vice versa. The discrete-time firing map captures the intrinsic (i.e. unperturbed) dynamics of the HCO model in a single finite-difference equation.

We derive the firing map as follows. Assume that at time t^k cell 1 has just fired and has been reset to phase 0 (labeled ‘Start’ in figure 4.3 cell 1) and that cell 2 has just been phase shifted by an inhibitory synaptic pulse and is at phase ϕ^k (labeled ‘Start’ in figure 4.3 cell 2). The superscript represents the number of firings that have occurred in the system since

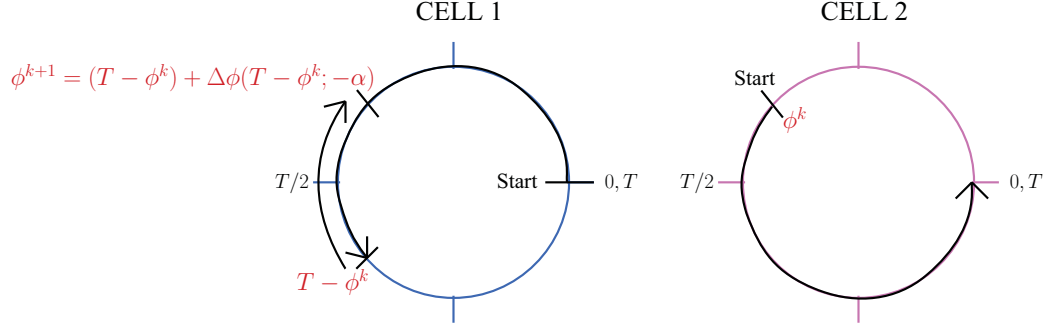


FIGURE 4.3. Deriving the firing map. The circles represent the phase of each cell.

time 0. The phases of the cells increase linearly (i.e. evolve at a rate of 1) until cell 2 reaches phase T , at which time (t^{k+1}) cell 2 fires, is reset to phase 0, and triggers an inhibitory synaptic pulse of strength α in cell 1. At this point, both cells have moved a distance of $T - \phi^k$, putting cell 1 at phase $T - \phi^k$ prior to the inhibitory pulse. Therefore, the phase shift of cell 1 due to the inhibitory synaptic pulse is $\Delta\phi(T - \phi^k)$, making the phase of cell 1 immediately after the pulse

$$(4.7) \quad \phi^{k+1} = T - \phi^k + \Delta\phi(T - \phi^k) = h(\phi^k).$$

This relationship is the firing map. The map has also been referred to as the spike time response curve map [GE02] [NBD⁺05] [OM09]. That is, when this map is iterated, it gives the phase of cell 1 after cell 2 fires and vice versa. For example, let cell 1 be at phase $\phi_1^0 = 0$ and cell 2 be at phase ϕ_2^0 . After one firing in the system, cell 2 is at phase $\phi_2^1 = 0$ and cell 1 is at phase $\phi_1^1 = h(\phi_2^0) = T - \phi_2^0 + \Delta\phi(T - \phi_2^0)$. After a second firing in the system, cell 1 is at phase $\phi_1^2 = 0$ and cell 2 is at phase $\phi_2^2 = h(\phi_1^1) = T - \phi_1^1 + \Delta\phi(T - \phi_1^1)$. When an appropriate form for the synaptic PRC $\Delta\phi$ is chosen (discussed in section 4.2.1), this firing map converges to a fixed point that corresponds to anti-phase, as illustrated graphically in figure 4.4.

4.2.1. Fixed point of the firing map corresponds to anti-phase. We now find the fixed point of the firing map along with conditions for its stability because we are interested in stable anti-phase oscillations in the HCO. During steady state anti-phase oscillations, when cell 1 is at phase 0 and cell 2 is at phase ϕ^* , after one firing in the system (i.e. at half-period of the HCO) cell 1 will be at phase ϕ^* and cell 2 will be at phase 0, and this pattern repeats. Thus, ϕ^* is the fixed point of the firing map (as shown in figure 4.4); i.e.,

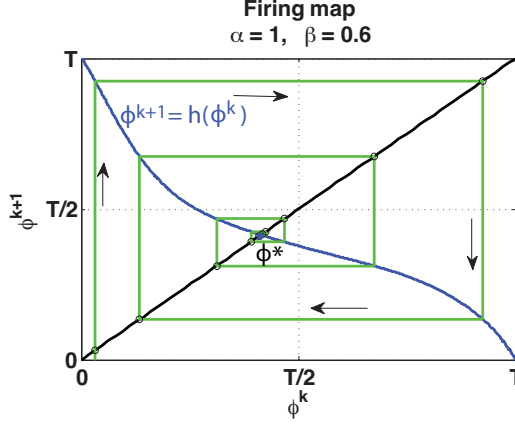


FIGURE 4.4. Iterations of the firing map $\phi^{k+1} = h(\phi^k)$ (map shown in blue). $z(\phi) = \beta - \sin(\phi + \sin^{-1}(\beta))$. $\alpha = 1$, $\beta = 0.6$. Map converges to stable fixed point ϕ^* .

ϕ^* can be found by solving

$$(4.8) \quad \phi^* = h(\phi^*) = T - \phi^* + \Delta\phi(T - \phi^*).$$

The fixed point ϕ^* is stable if and only if $|h'(\phi^*)| < 1$, i.e.

$$(4.9) \quad -1 < h'(\phi^*) = -1 - \Delta\phi'(T - \phi^*) < 1$$

which implies

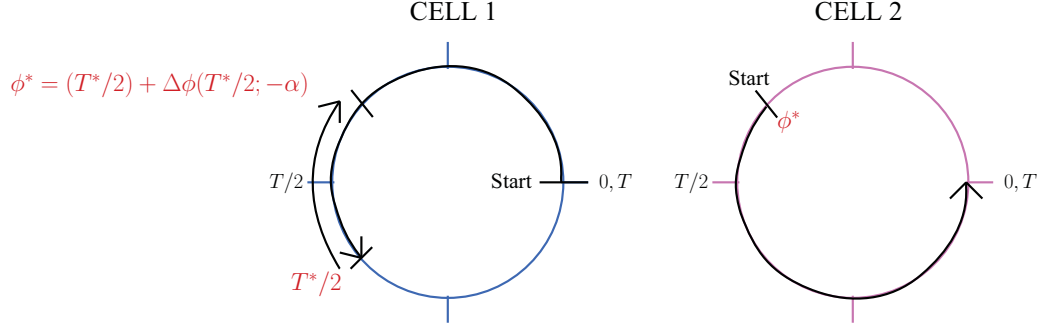
$$(4.10) \quad -2 < \Delta\phi'(T - \phi^*) < 0.$$

Therefore, if the slope of the synaptic PRC at phase $T - \phi^*$, $\Delta\phi'(T - \phi^*)$, is between -2 and 0, then the fixed point ϕ^* is stable. This corresponds to the criterion for stable anti-phase behavior in the HCO.

We define T^* as the period of the steady state oscillation of the HCO. When the above conditions for stable anti-phase are met, each inhibitory synaptic pulse arrives at phase $T^*/2$, as seen in figure 4.5. The period T^* is a combination of the intrinsic period and the phase shift due to the inhibitory pulse.

$$(4.11) \quad T^* = T - \Delta\phi(T^*/2).$$

Note that T^* is implicitly dependent on synaptic strength α and the PRC of the single cells $z(\phi)$ through $\Delta\phi(\phi)$. Because $T - \phi^* = T^*/2$, we can also write the fixed point equation

FIGURE 4.5. The fixed point of the firing map is ϕ^* .

(4.8) as

$$(4.12) \quad \phi^* = T^*/2 + \Delta\phi(T^*/2).$$

4.2.2. Linearize the firing map. When determining the PRC of the HCO, we give small perturbations to cell 1 when the HCO system is in anti-phase, and therefore the corresponding state in the firing map (equation 4.7) will not be moved far from the stable fixed point of the firing map ϕ^* . Thus, we can linearize the firing map around ϕ^* and obtain a good approximation of the full map. The linear map can be solved exactly for the change in phase that results from the small perturbation. The full details regarding the linearization are in the appendix.

Let $\phi^k = \phi^* + \tilde{\phi}^k$. $\tilde{\phi}^k$ is a small perturbation away from the steady state, ϕ^* . Substituting this into our firing map (equation (4.7)) and linearizing around $\phi^k = \phi^*$, we obtain the linearized map

$$(4.13) \quad \tilde{\phi}^{k+1} = h'(\phi^*)\tilde{\phi}^k.$$

If $\phi^* + \tilde{\phi}^0$ is the initial condition for the firing map, then

$$(4.14) \quad \tilde{\phi}^k = [h'(\phi^*)]^k \tilde{\phi}^0, \quad k = 0, 1, 2, \dots$$

Note that when deriving the PRC for the HCO, the initial condition $\phi^* + \tilde{\phi}^0$ for the map depends on the timing of the pulse. The firing map only captures the dynamics of the

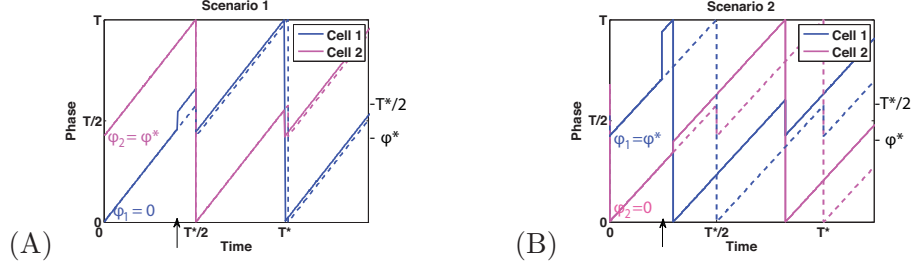


FIGURE 4.6. (A) Scenario 1: cell 1 is lagging when it receives the ϵ -pulse. (B) Scenario 2: cell 1 is leading when it receives the ϵ -pulse.

system after the first cell fires following the perturbation. This issue will be discussed in sections 4.3.1 and 4.3.2.

4.3. PRC of HCO

To measure the PRC of the HCO, a δ -function perturbation of size ϵ ($\epsilon \ll 1$) is delivered only to cell 1 at various times (t_θ) in the period of the HCO during steady state oscillations. There are two scenarios to consider. In scenario 1, the pulse is given to cell 1 while cell 1 is lagging, i.e. the next cell to fire in the system is cell 2. In scenario 2, the pulse is given to cell 1 while cell 1 is leading, i.e. the next cell to fire in the system is cell 1. $\tilde{\phi}^0$ is the change in phase of the lagging cell after the leading cell fires. We denote the phase of the HCO by θ and the time at which the perturbation is given by t_θ ($0 < t_\theta < T^*$). The phase of the cells within the HCO are denoted by ϕ_1 and ϕ_2 , respectively, with $0 < \phi_i < T$.

4.3.1. Scenario 1: Cell 1 is lagging. At time 0, we let cell 1 begin at phase $\phi_1 = 0$ and cell 2 begin at phase $\phi_2 = \phi^*$, i.e. the cells are in anti-phase (see figure 4.6A). The perturbation is given to cell 1 between time $0 < t_\theta < T^*/2$, where the phase of cell 1 is between $0 < \phi_1 < T^*/2$ (figure 4.7A). Note that this scenario will give the HCO PRC for phases $0 < \theta < T^*/2$. Figure 4.7B shows the firing times for scenario 1. Vertical lines represent the time at which the cells fire and are reset. Blue lines indicate times at which cell 1 fires and pink lines indicate times at which cell 2 fires. The dotted lines indicate the unperturbed firing times. The solid lines indicate firing times following the perturbation. We denote the firing times as t_i and the phase of the cell that does not fire at time t_i as ϕ^i (recall the phase of the cell that fires at time t_i is $T \rightarrow 0$). The small perturbation causes

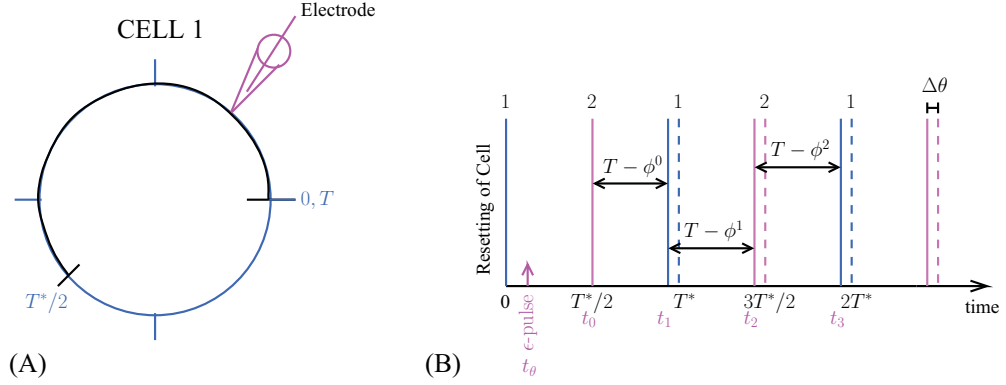


FIGURE 4.7. Scenario 1: $0 < \phi_1 < T^*/2$. The ϵ -pulse is given to cell 1 when cell 1 is following cell 2. The firing times are denoted by vertical lines with the number of the firing cell above them. The unperturbed firing times are denoted by dotted lines. The perturbed firing times are denoted by solid lines. The difference between where cell 1 would have fired and where it did fire after the ϵ -pulse is recorded as the change in phase, $\Delta\theta$.

cell 1 to instantaneously shift its phase by $\epsilon z(\phi_1)$. When cell 2 fires at time

$$(4.15) \quad t_0 = T^*/2,$$

cell 1 is at phase $T^*/2 + \epsilon z(\phi_1)$, and therefore the inhibitory synaptic pulse from cell 2 shifts the phase of cell 1 by $\Delta\phi(T^*/2 + \epsilon z(\phi_1))$. Thus, immediately after cell 2 has fired and has been reset to phase 0, the phase of cell 1 is

$$(4.16) \quad \phi^0 = T^*/2 + \epsilon z(\phi_1) + \Delta\phi(T^*/2 + \epsilon z(\phi_1))$$

From here on, the dynamics of the system, i.e. the return to anti-phase, are governed by the firing map in equation (4.7) with ϕ^0 serving as the initial condition when iterating the map.

Because the size of the perturbation ϵ is small, we can do a Taylor series expansion of $\Delta\phi(T^*/2 - \epsilon z(\phi_1))$ about $\epsilon = 0$ to obtain

$$(4.17) \quad \phi^0 = T^*/2 + \Delta\phi(T^*/2) + \epsilon z(\phi_1)[1 + \Delta\phi'(T^*/2)] + O(\epsilon^2)$$

$$(4.18) \quad = \phi^* + \tilde{\phi}^0,$$

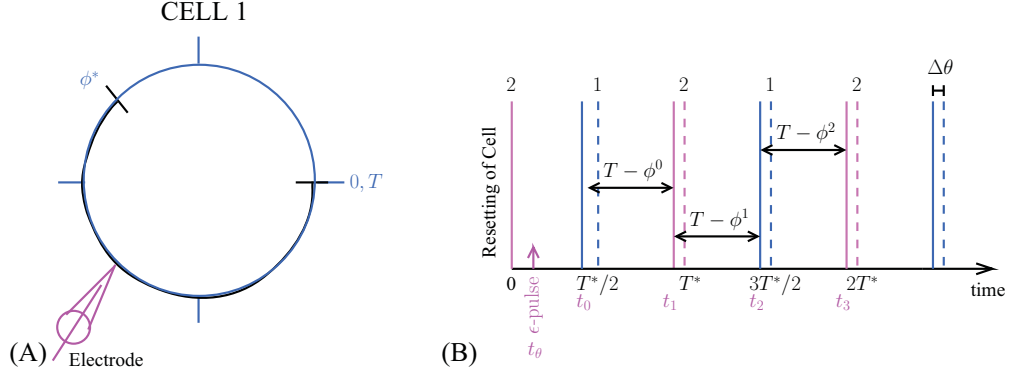


FIGURE 4.8. Scenario 2: $\phi^* < \phi_1 < T$. The ϵ -pulse is given to cell 1 when cell 1 is leading cell 2. The firing times are denoted by vertical lines with the number of the firing cell above them. The unperturbed firing times are denoted by dotted lines. The perturbed firing times are denoted by solid lines. The difference between where cell 1 would have fired and where it did fire after the ϵ -pulse is recorded as the change in phase, $\Delta\theta$.

where we have used $\phi^* = T^*/2 + \Delta\theta(T^*/2)$ (equation (4.12)). Thus, for scenario 1, i.e. for perturbations of the HCO when the phase of cell 1 is $0 < \phi_1 < T^*/2$

$$(4.19) \quad \tilde{\phi}^0 \approx \epsilon z(\phi_1)[1 + \Delta\phi'(T^*/2)].$$

4.3.2. Scenario 2: Cell 1 is leading. At time 0, we let cell 1 begin at phase $\phi_1 = \phi^*$ and cell 2 begin at phase $\phi_2 = 0$ (see figure 4.6B). The perturbation is given to cell 1 between time $0 < t_\theta < T^*/2$, where the phase of cell 1 is between $\phi^* < \phi_1 < T$ (figure 4.8A). Note that this scenario will give the HCO PRC for phases $T^*/2 < \theta < T^*$. We shift it here for convenience in calculating the PRC. Figure 4.8B shows the firing times for scenario 2, similar to figure 4.7B. The perturbation causes cell 1 to instantaneously shift its phase by $\epsilon z(\phi_1)$. Instead of firing at time $T^*/2$, cell 1 fires at time

$$(4.20) \quad t_0 = T^*/2 - \epsilon z(\phi_1).$$

At this time, cell 2, which is now at phase $T^*/2 - \epsilon z(\phi_1)$, receives an inhibitory synaptic pulse from cell 1 that instantaneously shifts its phase by $\Delta\phi(T^*/2 - \epsilon z(\phi_1))$. Thus, immediately after cell 1 has fired and been reset, the phase of cell 2 is

$$(4.21) \quad \phi^0 = T^*/2 - \epsilon z(\phi_1) + \Delta\phi(T^*/2 - \epsilon z(\phi_1))$$

$$(4.22) \quad = T^*/2 + \Delta\phi(T^*/2) - \epsilon z(\phi_1)[1 + \Delta\phi'(T^*/2)] + O(\epsilon^2)$$

$$(4.23) \quad = \phi^* + \tilde{\phi}^0,$$

where we have used the same argument as in scenario 1. Thus, for scenario 2, i.e. for perturbations of the HCO when the phase of cell 1 is $\phi^* < \phi_1 < T$

$$(4.24) \quad \tilde{\phi}^0 \approx -\epsilon z(\phi_1)[1 + \Delta\phi'(T^*/2)].$$

4.3.3. Timing. For the two scenarios, we now have the initial firing time t_0 and the initial conditions for the firing map ϕ^0 .

$$(4.25) \quad \begin{array}{ll} \text{Scenario 1:} & t_0 = T^*/2 & \tilde{\phi}^0 = \epsilon z(\phi_1)[1 + \Delta\phi'(T^*/2)] \\ \text{Scenario 2:} & t_0 = T^*/2 - \epsilon z(\phi_1) & \tilde{\phi}^0 = -\epsilon z(\phi_1)[1 + \Delta\phi'(T^*/2)]. \end{array}$$

To calculate the PRC of the HCO, we take the difference in firing times from the perturbed and unperturbed system (denoted by $\Delta\theta$ in figures 4.7 and 4.8). If no perturbation is given to the system, then the firing times during steady state oscillations are

$$(4.26) \quad t_k^{UP} = (k+1)\frac{T^*}{2}, \quad k \in \mathbb{Z},$$

where UP stands for ‘unperturbed’. Following the perturbation, the time intervals between firings are given by $T - \phi^k$ (as shown in figures 4.7 and 4.8). Thus, the firing times of the perturbed system are

$$(4.27) \quad t_k = t_0 + \sum_{i=0}^{k-1} (T - \phi^i)$$

$$(4.28) \quad = t_0 + \sum_{i=0}^{k-1} (T - (\phi^* + \tilde{\phi}^i))$$

$$(4.29) \quad = t_0 + k(T - \phi^*) - \tilde{\phi}^0 \sum_{i=0}^{k-1} [h'(\phi^*)]^i = t_0 + k\frac{T^*}{2} - \tilde{\phi}^0 \frac{1 - [h'(\phi^*)]^k}{1 - h'(\phi^*)}$$

$$(4.30) \quad = t_0 + k(T^*/2) - \tilde{\phi}^0 \frac{1 - [-1 - \Delta\phi'(T^*/2)]^k}{2 + \Delta\phi'(T^*/2)}.$$

We have used the linearized firing map (equation (4.14)) in (4.28) and (4.29), as well as the fact that $\sum_{i=0}^{k-1} [h'(\phi^*)]^i$ is a geometric series with $|h'(\phi^*)| < 1$ (equation (4.9)).

The change in phase $\Delta\theta^k$ of the HCO is given by the change in firing times $t_k^{UP} - t_k$.

$$(4.31) \quad \Delta\theta^k = t_k^{UP} - t_k$$

$$(4.32) \quad = T^*/2 - t_0 + \tilde{\phi}^0 \frac{1 - [-1 - \Delta\phi'(T^*/2; -\alpha)]^k}{2 + \Delta\phi'(T^*/2; -\alpha)}.$$

Note that $\Delta\theta^k$ is the $k/2^{th}$ order PRC, i.e. the PRC after $k/2$ firings in the system. The PRC of the HCO is the asymptotic change in phase that results from the perturbation, $\lim_{(k \rightarrow \infty)} \Delta\theta^k$. If the stability condition for the anti-phase state is met (equation (4.10)), then $0 < |-1 - \Delta\phi'(T^*/2)| < 1$ and as $k \rightarrow \infty$, $[-1 - \Delta\phi'(T^*/2)]^k \rightarrow 0$. The resulting PRC of the HCO is

$$(4.33) \quad \Delta\theta = T^*/2 - t_0 + \frac{\tilde{\phi}^0}{2 + \Delta\phi'(T^*/2)}.$$

Equation 4.33 depends on t_0 and $\tilde{\phi}^0$, which were derived in sections 4.3.1 and 4.3.2.

4.3.4. Analytically derived PRC of HCO. To obtain the PRC for the HCO, we combine results in sections 4.3.1 - 4.3.3 as follows. Consider the HCO oscillating at steady state. At time $t = 0$, let cell 1 be at phase $\phi_1 = 0$ and cell 2 at phase $\phi_2 = \phi^*$. If the perturbation is given to cell 1 between times $0 < t_\theta < T^*/2$, then cell 1 is lagging behind cell 2 and the PRC of the HCO is found using t_0 and $\tilde{\phi}_0$ from scenario 1. If the pulse is given to cell 1 between times $T^*/2 < t_\theta < T^*$, then cell 1 is leading cell 2 and the PRC of the HCO is found using t_0 and $\tilde{\phi}_0$ from scenario 2, using an appropriate shift in phase. Combining the two scenarios and normalizing by the size of the perturbation ϵ , we get the piecewise defined PRC of the HCO.

$$(4.34) \quad \Delta\theta = \begin{cases} z(t_\theta) \frac{1 + \Delta\phi'(T^*/2)}{2 + \Delta\phi'(T^*/2)}, & 0 \leq t_\theta < T^*/2 \\ z(t_\theta - (T^*/2 - \phi^*)) \frac{1}{2 + \Delta\phi'(T^*/2)}, & T^*/2 \leq t_\theta < T^*. \end{cases}$$

Equation 4.34 shows that the PRC for the HCO is a product of the single cell PRC and an attenuation factor. When using the synaptic PRC $\Delta\phi$, the HCO PRC $\Delta\theta$ is continuous at $T^*/2$, but $\Delta\theta'$ can be discontinuous at $T^*/2$. In each half of the PRC, the attenuation factor is a function of the slope of the synaptic PRC at anti-phase ($\Delta\phi'(T^*/2)$). Recall that $\Delta\phi'(T^*/2)$, as well as T^* and ϕ^* , are determined by $z(\phi)$ and α (see section 4.1.1).

Note that the attenuation factor in the first half differs from that in the second half only in the numerator. Recall that we have assumed $-2 < \Delta\phi'(T^*/2) < 0$, so the extra term in the first half of the PRC leads to greater attenuation than the second half. For large α , $\Delta\phi$ is the distance between where a pulse is given and the zero of $z(\phi)$. Therefore, as the coupling strength α increases, $\Delta\phi'(T^*/2) \rightarrow -1$. This means the attenuating factor in the first half of the PRC goes to 0 and the attenuating factor in the second half goes to 1. Therefore, for sufficiently strong and fast coupling in the HCO, external input arriving in the first half of the period will have little or no effect on the timing of the HCO, and input arriving in the second half of the period will cause a shift in phase determined solely by the single cell PRC. Also note that as $\alpha \rightarrow 0$, $\phi^* \rightarrow T/2$ and $T^*/2 \rightarrow T/2$. Therefore, as $\alpha \rightarrow 0$, $\Delta\phi \rightarrow -\alpha z(\phi) \rightarrow 0$ and $\Delta\theta \rightarrow z(t_\theta)/2$.

4.3.5. $k/2^{th}$ order PRC of HCO. The analytic PRC of the HCO is the infinitesimal PRC, or iPRC, for the HCO. It is derived by taking the $\lim_{k \rightarrow \infty} \Delta\theta^k$, where $\Delta\theta^k$ is the $k/2^{th}$ order PRC.

(4.35)

$$\Delta\theta^k = \begin{cases} z(t_\theta)[1 + \Delta\phi'(T^*/2)]^{\frac{1-[-1-\Delta\phi'(T^*/2)]^k}{2+\Delta\phi'(T^*/2)}}, & 0 < t_\theta < T^*/2 \\ z(t_\theta - (T^*/2 - \phi^*)) \left(1 - [1 + \Delta\phi'(T^*/2)]^{\frac{1-[-1-\Delta\phi'(T^*/2)]^k}{2+\Delta\phi'(T^*/2)}}\right), & T^*/2 < t_\theta < T^*. \end{cases}$$

4.4. Application to sinusoidal PRCs

In this section, we use $z(\phi) = \beta - \sin(\phi + \sin^{-1}(\beta))$ with $T = 2\pi$ and $\beta \in [-1, 1]$ as the single cell PRC. $z(\phi)$ is defined so that $z(0) = z(T) = 0$, as is the case for most neuronal PRCs. The following examples compare the analytic PRC of the HCO to the numerically generated PRC of the HCO for a range of synaptic strengths α and various values of β . The parameter β can be thought of as the single cell skewness factor of the PRC, but note that it also changes the average of the PRC [ZS09]. Note that $\beta \in [-1, 1]$ does not guarantee that the HCO is in anti-phase, as the stability condition for anti-phase in equation (4.10) must be met, as well.

In figure 4.9, $\alpha = 1$ and $\beta = 0.5$, and in figure 4.10, $\alpha = 4$ and $\beta = 0.2$. Figures 4.9A and 4.10A show the synaptic PRC (blue) and the convolution of the synaptic strength and

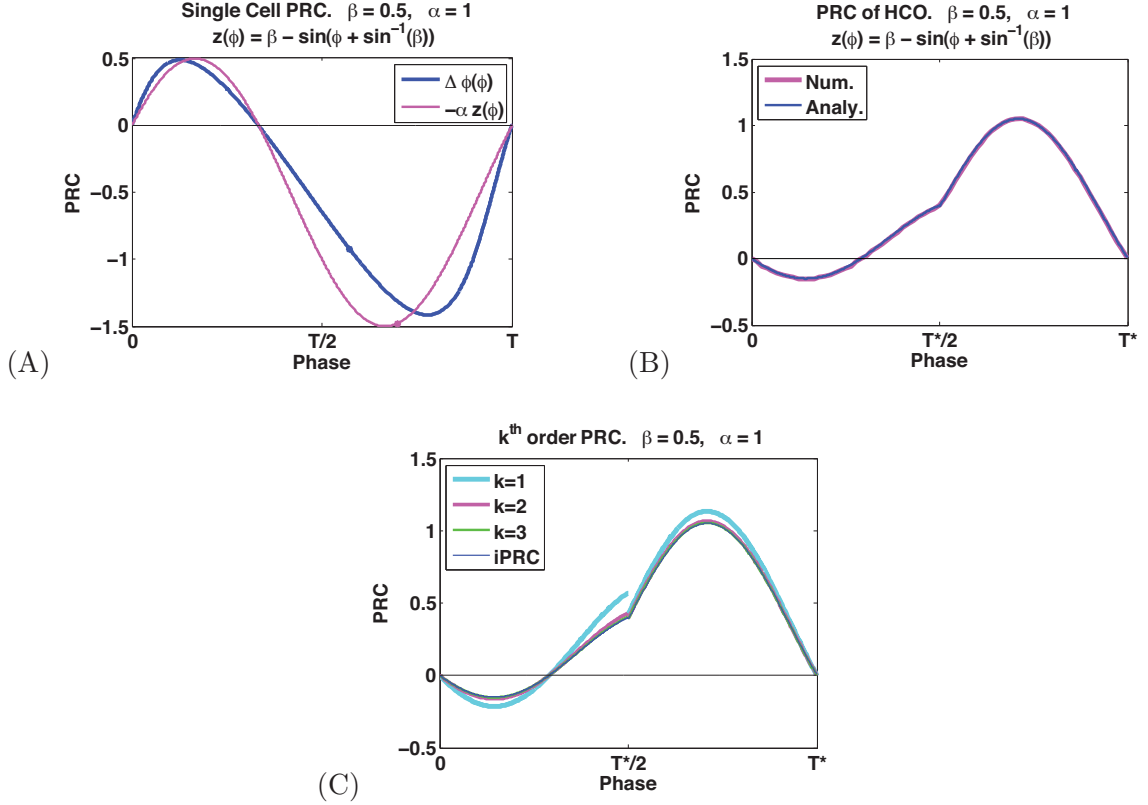


FIGURE 4.9. $\alpha = 1$ and $\beta = 0.5$. (A) $-\alpha z(\phi)$ and $\Delta\phi(\phi; -\alpha)$. (B) Numerical and analytic PRC of the HCO. (C) k^{th} order PRC.

single cell iPRC (pink). In figure 4.9A, the shape of the synaptic PRC $\Delta\phi(\phi)$ is similar to $-\alpha z(\phi)$, but the positive and negative peaks of $\Delta\phi(\phi)$ are further skewed towards phases 0 and T . In figure 4.10A, this skew is dramatic, because α is much larger. In figure 4.9A and 4.10A, anti-phase $T^*/2$ is shown with a blue dot on the synaptic PRC.

We compare the synaptic PRC to the single cell iPRC because important differences occur if the correct limit to the delta function is not taken. If, in section 4.1, the standard δ -function was used to replace the synaptic conductance, this alternate phase model would have $-\alpha\delta(\phi_j)z(\phi_i)$ as the coupling term instead of $\delta(\phi_j)\Delta\phi(\phi_i)$, i.e. the two models use different PRCs. The differences are dramatic. If $-\alpha\delta(\phi_j)z(\phi_i)$ is the coupling term, the anti-phase state $T^*/2$ is different (pink dot on single cell iPRC). Upon inspection it is clear that that the slopes of the two curves at their respective anti-phase states are very different, which can lead to very different HCO PRCs. The consequences of this are discussed in chapter 7.

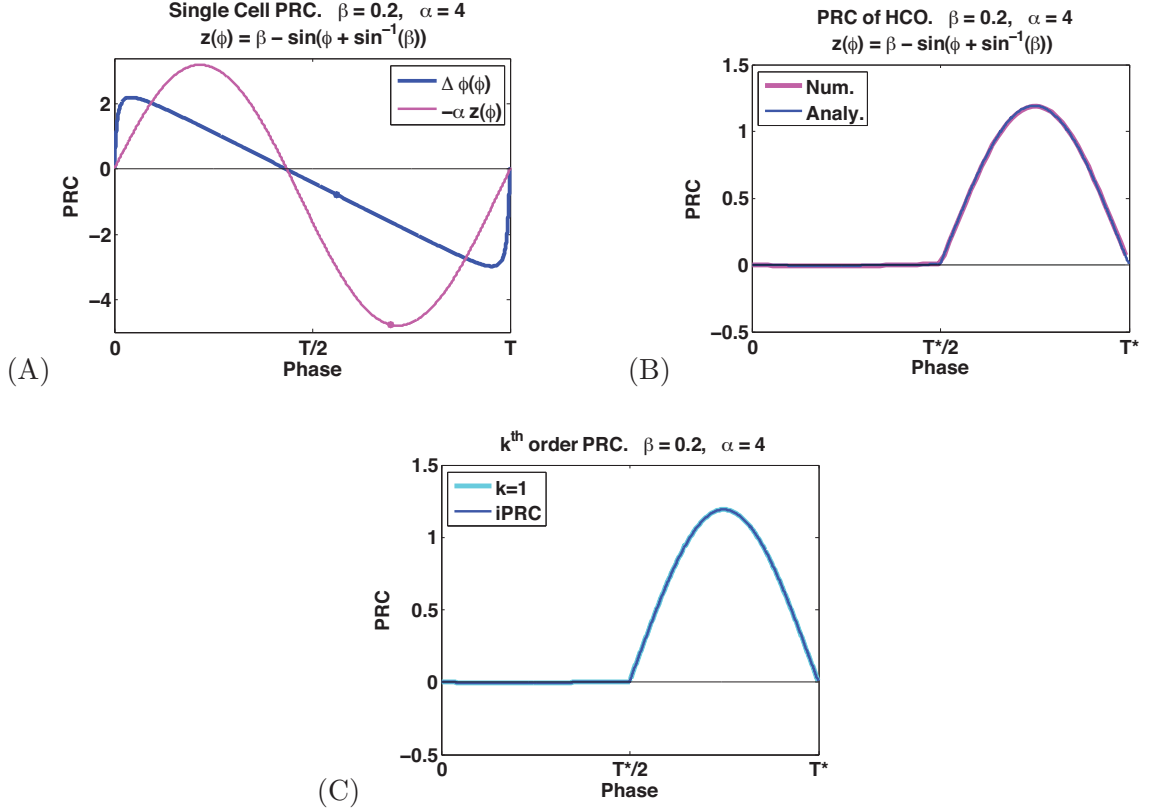


FIGURE 4.10. $\alpha = 4$ and $\beta = 0.2$. (A) $-\alpha z(\phi)$ and $\Delta\phi(\phi; -\alpha)$. (B) Numerical and analytic PRC of the HCO. (C) k^{th} order PRC.

4.4.1. Attenuation. Recall that the slope of the synaptic PRC at anti-phase $\Delta\phi'(T^*/2)$ determines the amount of attenuation in each half of the PRC of the HCO, as in equation (4.34). The attenuation in each half of HCO PRC is shown in figure 4.11, as indicated by the form of $\Delta\theta$ (equation 4.34). For all β , as the coupling strength α increases, $\Delta\phi'(T^*/2) \rightarrow -1$, and the attenuation of the PRC goes to zero in the first half and one in the second half. The numerical and analytical HCO PRCs are compared in figures 4.9B and 4.10B. In figure 4.9B, the qualitative shape of the HCO PRC is similar to the single cell PRC $z(\phi)$, but the amplitude is decreased due to the attenuation. The discontinuity in $\Delta\theta'$ at $T^*/2$ is due to the change in attenuation between the two halves of the HCO PRC. In figure 4.10B, α is significantly larger than in figure 4.9B. In figure 4.11 we see that when $\alpha = 4$ and $\beta = 0.2$, the attenuation in the first half of the HCO PRC is almost zero and in the second half is almost 1. That is exactly what we see in figure 4.10B, as indicated by the form of $\Delta\theta$ (equation 4.34). For these parameters, external input arriving in the first half of the period will have no effect on the timing of the HCO.

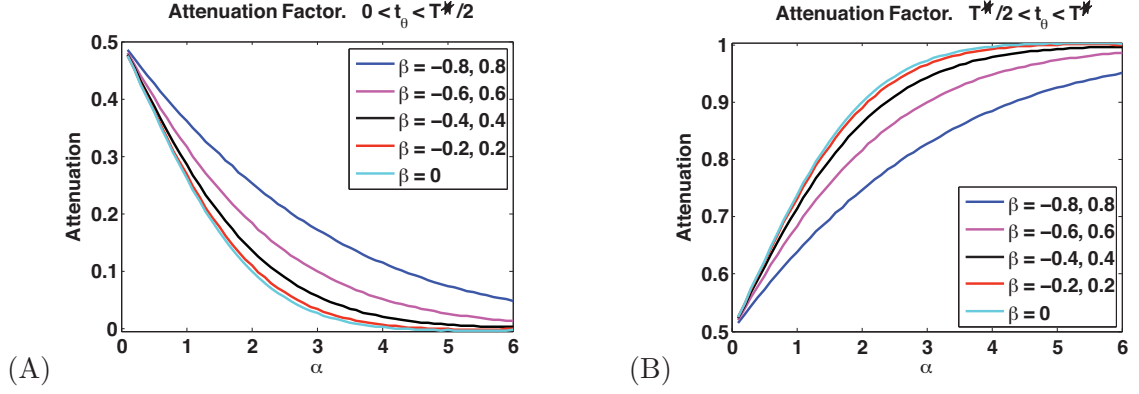


FIGURE 4.11. Attenuation factors for the PRC of the HCO (equation (4.34)). (A) First half of the PRC ($0 < t_\theta < T^*/2$). (B) Second half of the PRC ($T^*/2 < t_\theta < T^*$).

4.4.2. Convergence rate. The analytically derived PRC of the HCO is the infinitesimal PRC, or iPRC, for the HCO. It is derived by taking the $\lim_{k \rightarrow \infty} \Delta\theta^k$, where $\Delta\theta^k$ is the k^{th} order PRC. Letting $k \rightarrow \infty$ ensures that the HCO has returned to steady state oscillations. In the interim, there is a ringing effect in the HCO. For example, say cell 1 is about to fire when it receives a stimulus and as a result fires sooner. The change in firing time causes a phase shift in cell 2 making it fire at a new time. This causes another phase shift in cell 1, and so on. This ringing effect lasts longer when the coupling between the two cells is weak. We note that in order to study phase-locking in a chain of HCOs using the TWCO, the ringing effect must be small, i.e. the PRC of the HCO must converge close enough to the iPRC before another input to the HCO arrives.

In figures 4.9C, 4.10C, 4.12, and 4.13, we look at how long it takes the k^{th} order PRC $\Delta\theta^k$ to approach the analytic iPRC $\Delta\theta$. We examine the convergence using the norm of the difference between the k^{th} order PRC and the iPRC, normalized by the iPRC:

$$(4.36) \quad \text{norm}(k) = \frac{\|\Delta\theta^k(t_\theta) - \Delta\theta(t_\theta)\|_2}{\|\Delta\theta(t_\theta)\|_2},$$

where $\|\cdot\|_2$ is the standard ℓ^2 -norm. Figures 4.9C and 4.10C show the k^{th} order PRCs compared to the iPRC. We say the k^{th} order PRC has converged when $\text{norm}(k) < 10^{-2}$, which was chosen arbitrarily. Note that this is a strict constraint because it gives a 1% difference between the two functions. When $\beta = 0.5$ and $\alpha = 1$ (figure 4.9C), the k^{th} order PRC converges 2 HCO periods after the perturbation. When $\beta = 0.2$ and $\alpha = 4$

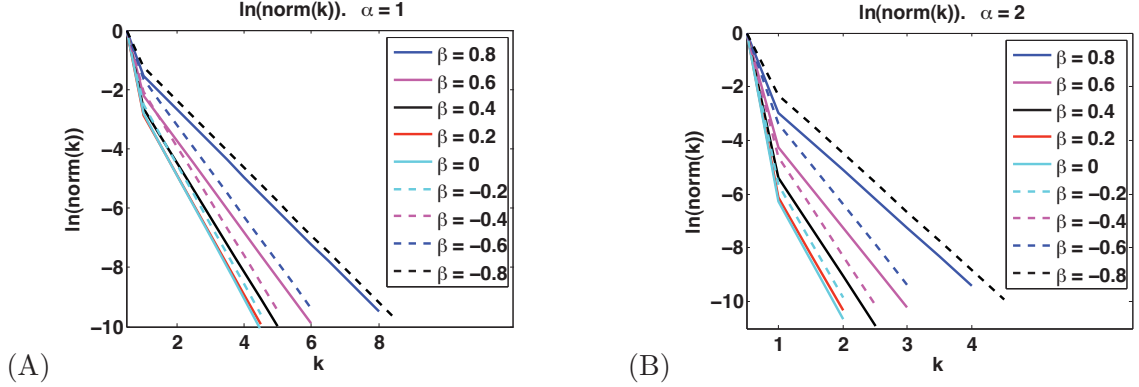


FIGURE 4.12. Natural logarithm of the norm in equation (4.36). k is the number of HCO oscillations. (A) $\alpha = 1$ and (B) $\alpha = 2$.

(figure 4.10C), the k^{th} order PRC converges after 1 HCO period. The dependence of the convergence on α and β are shown in figures 4.12 and 4.13.

The convergence rate of the k^{th} order PRC is determined by the slope of the firing time map at the fixed point, $h(\phi^*)$, which measures the rate of relaxation back to the anti-phase oscillation following the perturbation. If $|h'(\phi^*)| < 1$ the firing map will be stable and the k^{th} order PRCs will always converge to the iPRC. The smaller $|h'(\phi^*)|$ is, the faster the k^{th} order PRCs will converge. The convergence rate is

$$(4.37) \quad |h'(\phi^*)| = |-1 - \Delta\phi'(T^*/2)|,$$

which depends on the slope of the synaptic PRC at $T^*/2$ and therefore indirectly on α . We know that as α increases, $\Delta\phi'(T^*/2) \rightarrow -1$. Therefore, as α increases, $|h'(\phi^*)| \rightarrow 0$, which increases the convergence rate. As $\alpha \rightarrow 0$, $\Delta\phi \rightarrow 0$ and $h'(\phi^*) \rightarrow -1$, which decreases the convergence rate. This is exactly what we see in figures 4.12 and 4.13. In figure 4.12, the log of the norm in equation (4.36) is plotted as a function of the number periods it takes to converge. Here, linearity implies exponential convergence. In figure 4.13, we see that $-1 < h'(\phi^*) < 0$, which means the k^{th} order PRCs oscillate around the iPRC as they converge to it. Figures 4.12 and 4.13 also show the dependence of the convergence rate on β . The closer the single cell PRC is to $-\sin(\phi)$ ($\beta = 0$), the faster the convergence. This is because the slope at anti-phase is closest to -1 when $\beta = 0$. As $|\beta|$ increases, $-\sin(\phi)$ shifts and the slope at anti-phase moves toward -2 or 0 .

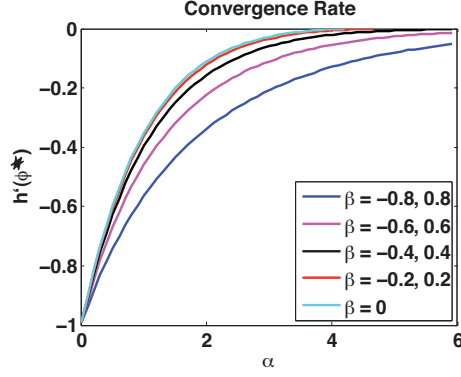


FIGURE 4.13. Convergence rate of the k^{th} order PRC (equation (4.35)) for various α and β .

As previously mentioned, the convergence rate of the approximation must be fast when studying phase-locking in a chain of HCOs using the TWCO. These results indicate that if α is large and/or $|\beta|$ is small, then a sufficiently fast convergence rate is expected. If α and β are such that the approximations to the iPRC sufficiently converge before the next input to the HCO, then we can use the TWCO to derive the phase-locked states. Phase-locking is discussed in chapter 6.

4.4.3. Exponential synapses. In figures 4.14 and 4.15, we numerically generate the PRC of the HCO using the idealized phase model with exponential synapses (equation 4.1) and compare the numerical PRC to the analytically derived PRC as the time constant for decay τ increases. In figure 4.14, $\alpha = 1$ and $\beta = 0.5$. In figure 4.15, $\alpha = 4$ and $\beta = 0.2$. When $\tau = .001$, $\tau \ll T = 1$ and the synaptic decay is nearly instantaneous (figure 4.14A & 4.15A). In this case, the analytically derived PRC closely approximates numerical PRC, indicating that the analytically derived PRC is a good approximation to the actual PRC for models that contain synapses with a fast decay time. Note that this is not the case if the standard δ -function is used to calculate the analytic PRC. When $\tau = .3$, (figures 4.14B & 4.15B), the synaptic conductance decays to approximately zero within half of the HCO period. In figure 4.14B, the analytic PRC closely approximates numerical PRC, and in figure 4.15B, the analytic approximation begins to deviate from the numerical PRC, due to the increased coupling strength α . When $\tau = .7$ (figures 4.14C & 4.15C), the synaptic conductance decays to approximately zero within one period, and the analytic PRC varies further from the numerical PRC. The analytically derived PRC still captures the qualitative shape of the numerically derived PRCs with slow synaptic coupling in the HCO. In both

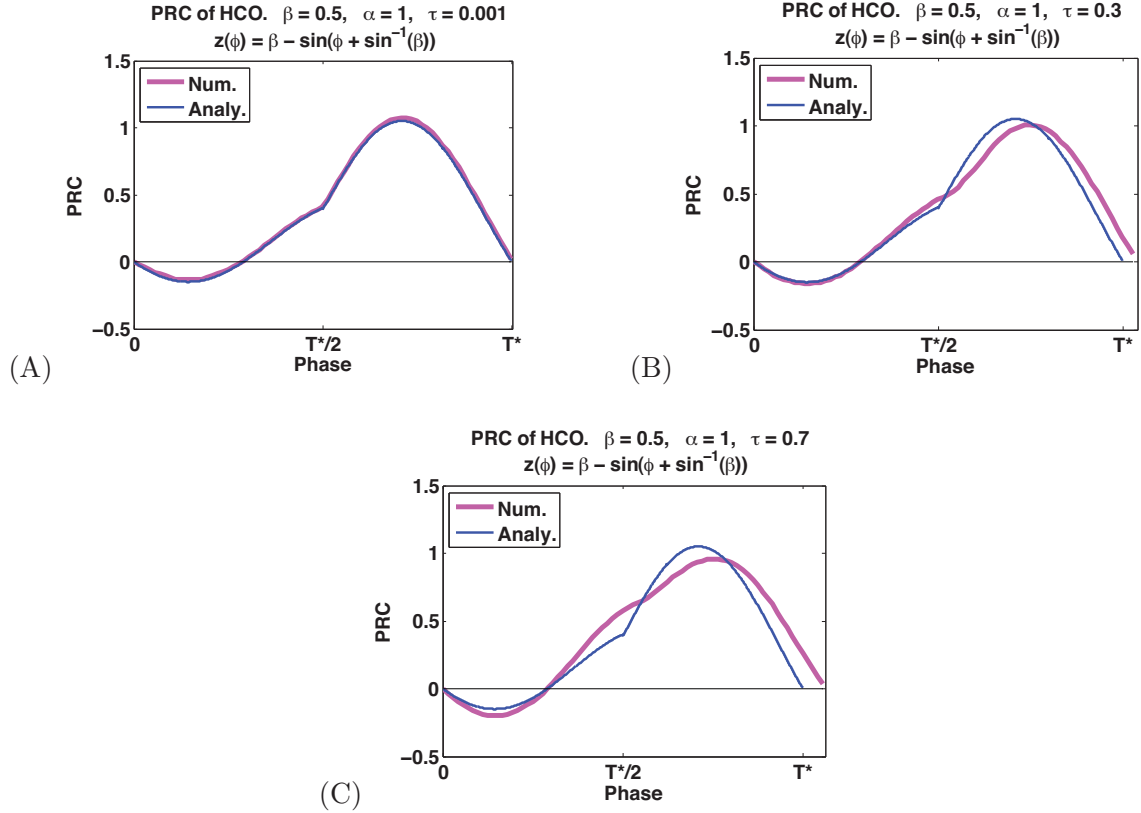


FIGURE 4.14. Comparing the analytic HCO PRC to the idealized phase model with exponential synapses when $\alpha = 1$ and $\beta = 0.5$. (A) $\tau = .001$. Very fast decay. (B) $\tau = .3$. Synapse decays within one period. (C) $\tau = .7$. Synaptic conductance sums.

figures, the period of the phase model with exponential synapses is larger than the δ -pulse coupled phase model due to the increase in the synaptic time constant. Figure 4.14 indicates that the analytic PRC can be used as a good approximation the numerical PRC for a wide range of synaptic time constants when the coupling between the two cells is not very strong. However, if the coupling between the two cells is strong as in figure 4.15, the analytic PRC is only a good quantitative approximation for small synaptic time constants and a good qualitative approximation for larger synaptic time constants.

4.5. Summary

- When the cells in the HCO are described by one-variable phase models and coupled with δ -function synapses, the PRC of the HCO is a product of the single cell PRC and an attenuation factor. Considering the results in chapter 3, we see that the HCO PRC often has the same qualitative shape as the single cell PRC and might be the product of the single cell PRC with an attenuation factor.

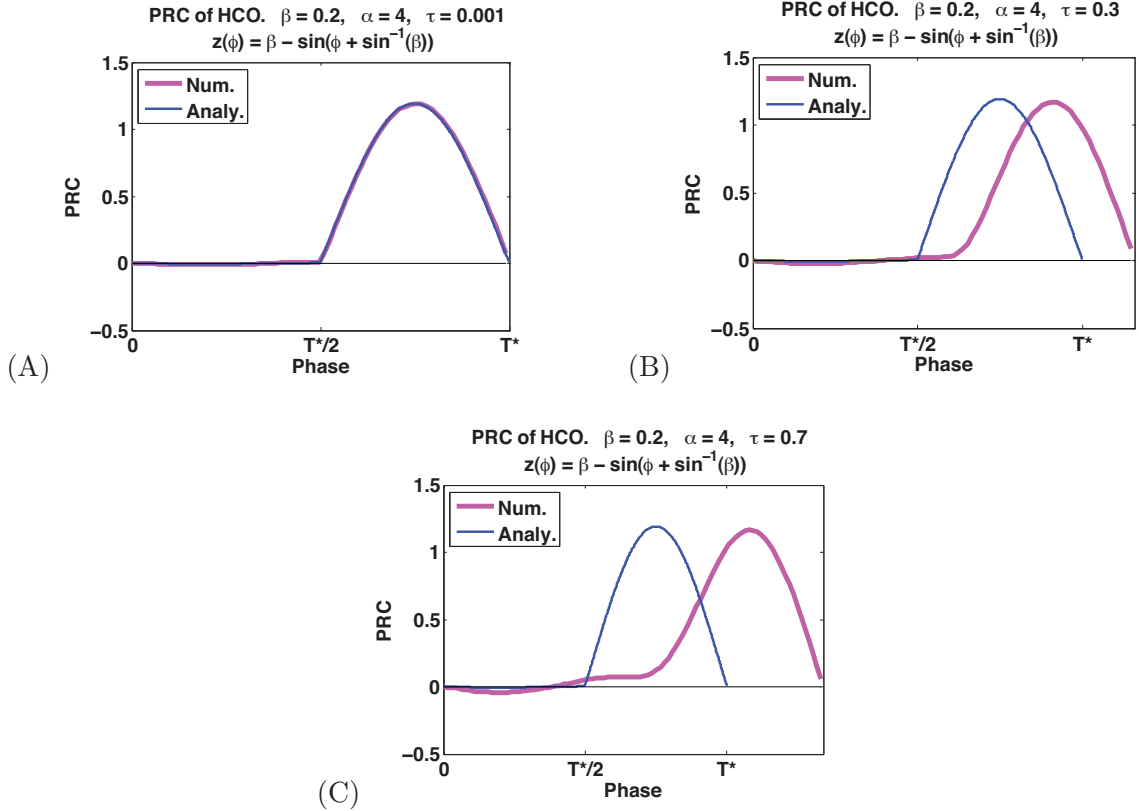


FIGURE 4.15. Comparing the analytic HCO PRC to the idealized phase model with exponential synapses when $\alpha = 4$ and $\beta = 0.2$. (A) $\tau = .001$. Very fast decay. (B) $\tau = .3$. Synapse decays within one period. (C) $\tau = .7$. Synaptic conductance sums.

- The analytically derived PRC of the HCO with δ -function synapses is a good qualitative and quantitative approximation to the PRC of the HCO with exponential synapses with sufficiently fast decay. The analytic PRC is also a good qualitative approximation to the PRC of the HCO with exponential synapses with slower decay.
- This work differs from that in Ko & Ermentrout [KE09]. Ko & Ermentrout derive the PRC of the HCO by delivering small pulses to both cells in the HCO at the same time. We deliver the pulse to only one cell in the HCO. If we added the HCO PRC generated from delivering the pulse cell 1 to the HCO PRC generated from delivering the pulse to cell 2, the result would be equivalent to stimulating both cells simultaneously, i.e. it would be directly comparable to Ko & Ermentrout. In most cases in this and the previous chapter, this would result in a HCO PRC that

is much smaller, and contains less phase information. The resulting PRCs would give less robust phase-locking results.

CHAPTER 5

Phase Response Properties of Half-Center Oscillators using Leaky Integrate-and-Fire Models

In this chapter, we use the leaky integrate-and-fire (LIF) model to describe the intrinsic dynamics of the cells within the HCO and derive an analytic expression for the PRC of the HCO. The LIF model describes the subthreshold dynamics of a cell equipped only with a leakage conductance and an external applied current. It is relatively easy to analytically compute the iPRC for the LIF model (see section A.3 in appendix). In the HCO, two LIF cells are coupled through either δ -function synapses or exponential synapses with sufficiently fast decay (as in chapter 4). The simplicity of the LIF HCO model allows for greater analytic tractability compared to the general phase model when the effects of slower synapses between the cells are included. Therefore, analyzing the LIF HCO with exponential synapses gives insight into how the decay rate of the synapses effect the PRCs.

5.1. General form of PRC for HCO

In this section, we derive a general form for the iPRC of a HCO modeled with two intrinsically oscillating LIF cells coupled through reciprocal inhibition. We introduce the model with exponential synaptic coupling, but note that δ -function coupling can be thought of as taking $\lim_{\tau \rightarrow 0} s(t)$, where τ is the rate of decay of the synaptic current. We assume that within one-half HCO period, the synapses have decayed sufficiently fast.

The equations governing the HCO are

$$\begin{aligned}
 (5.1) \quad & \frac{dV_1}{dt} = I - V_1 - \alpha s_2(t) && \text{if } V_1 = 1, V_1 \rightarrow 0; \\
 & \frac{dV_2}{dt} = I - V_2 - \alpha s_1(t) && \text{if } V_2 = 1, V_2 \rightarrow 0; \\
 & \frac{ds_1}{dt} = \frac{-s_1}{\tau} && \text{if } V_1 = 1, s_1 = 1/\tau \\
 & \frac{ds_2}{dt} = \frac{-s_2}{\tau} && \text{if } V_2 = 1, s_2 = 1/\tau
 \end{aligned}$$

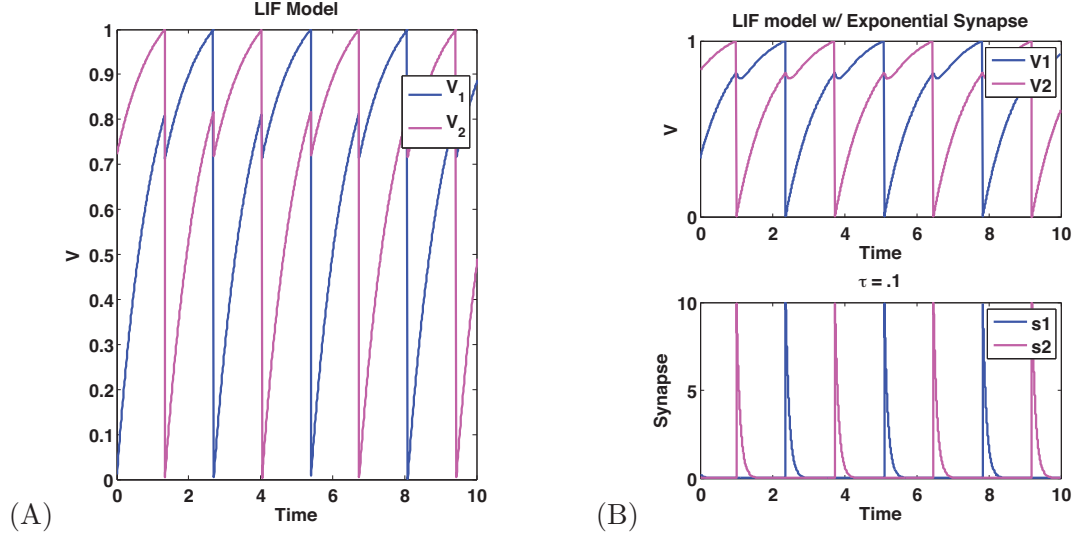


FIGURE 5.1. The voltage trace for the HCO where each cell is modeled with the LIF model. The two cells oscillate in anti-phase. $\alpha = 0.1$ and $I = 1.1$. (A) The cells are coupled through δ -function synapses. (B) The cells are coupled through exponential synapses, $\tau = 0.1$.

where V_i is the membrane potential of cell i and I is a constant applied current. The term $\alpha s_i(t)$ is the synaptic current, where α is the synaptic strength and $s_i(t)$ describes the synaptic waveform. If $\alpha > 0$, the synapse is inhibitory, and if $\alpha < 0$, the synapse is excitatory. In this chapter, we consider only inhibitory synapses ($\alpha > 0$). The parameter τ describes the rate of decay of the exponential synapse. If $I > 1$, then each cell oscillates intrinsically with single cell period $T = \ln(I/(I - 1))$. The associated iPRC of the single LIF cell is $z(t) = e^t/I$, $t \in (0, T)$ [LR03] (see appendix for derivation). Figure 5.1 shows an example of the dynamics in this model. Figure 5.1A shows the voltage trace of cells 1 and 2 during steady state oscillations when $\alpha = .1$, $I = 1.1$ when $s(t)$ is modeled with δ -functions, i.e. $\lim_{\tau \rightarrow 0} s(t)$. Figure 5.1B shows the voltage trace of cells 1 and 2 when the cells are coupled through exponential synapses and $\tau = 0.1$. When $V_i = 1$, cell i fires an action potential and triggers a synaptic current into cell j and V_i is reset to 0. For exponential synapses, when cell i fires, the synaptic current is instantaneously increased to $\alpha(1/\tau)$ and then decreases exponentially with time constant τ . Note that the model synapses are non-summing. For the parameters that we consider, the two cells oscillate in anti-phase creating a HCO [SKM94] [WR92].

The following subsections define a firing map for this model, which we use to derive the PRC for the HCO, similar to chapter 4.

5.1.1. Firing map. To derive the firing map, assume that cell 1 begins at $V_1(t^k) = 0$ and cell 2 at $V_2(t^k) = V^k$, i.e. cell 1 is lagging and cell 2 is leading. Superscript represents the number of firings that have occurred in the system since time 0, i.e. t^k is the time of the k^{th} spike. For synapses with sufficiently fast decay, we assume that $s_1(t^k) = 1/\tau$ and $s_2(t^k) = 0$. Let $V_A(t; 0)$ and $V_B(t; V^k)$ be the half-cycle solution for the LIF HCO model (equation 5.1) with these ‘initial’ conditions for cell 1 and cell 2, respectively.

$$(5.2) \quad V_A(t; 0) = I(1 - e^{-t})$$

$$(5.3) \quad V_B(t; V^k) = I(1 - e^{-t}) + \frac{\alpha}{\tau - 1} (e^{-t} - e^{-t/\tau}) + V^k e^{-t}.$$

Let $\Delta t^k = t^{k+1} - t^k$. The next firing in the system occurs when the leading cell (cell 2) reaches $V_B(\Delta t^k; V^k) = 1$. By solving this last equation for V^k or t^k , we obtain $V^k = G(\Delta t^k)$ or $\Delta t^k = G^{-1}(V^k)$, respectively. The functions G and G^{-1} can be found analytically or numerically depending on τ . We define $F(t) = V_A(t; 0)$ and find the voltage V^{k+1} of the lagging cell (cell 1) at Δt^k by $V^{k+1} = F(\Delta t^k)$. The firing time map is thus

$$(5.4) \quad \Delta t^{k+1} = G^{-1}(V^{k+1}) = G^{-1}(F(\Delta t^k))$$

Note that there is a corresponding map for voltages $V^{k+1} = F(G^{-1}(V^k))$. Sections 5.2 and 5.3 find specific forms for $G(t)$ and $F(t)$ for δ -function synapses and exponential synapses.

5.1.2. Fixed point of the firing map corresponds to anti-phase. Here, we consider the fixed point of the firing map (5.4) along with conditions for its stability using $F(t)$ and $G(t)$. Suppose $\Delta t^k = T^*/2$ is the fixed point of the firing map

$$(5.5) \quad T^*/2 = G^{-1}(V^*) = G^{-1}(F(T^*/2)).$$

The fixed point corresponds to anti-phase oscillations in the HCO where the time interval between subsequent firings is $T^*/2$ (i.e. T^* is the period of the steady anti-phase oscillation of the HCO). V^* corresponds to the voltage of the lagging cell when the leading cell fires during anti-phase oscillations. During anti-phase oscillations, cells fire at times $k\frac{T^*}{2}$, $k \in \mathbb{Z}$. $T^*/2$ and V^* can be found analytically for δ -function synapses, and numerically for exponential synapses by solving equation (5.5).

5.1.3. Linearization of the firing map and stability of fixed points. As in chapter 4, we give small perturbations to the HCO to determine the PRC of the HCO. Therefore, we can linearize the firing map to obtain a good approximation of the full map when these small perturbations are given. The linear map can be solved exactly for the change in phase that results from the perturbation.

Let $\Delta t^k = T^*/2 + \Delta \tilde{t}^k$, i.e. $\Delta \tilde{t}^k$ is a small perturbation away from the steady state, $T^*/2$. Substituting this into the firing map (equation (5.4)) and linearizing, we obtain

$$(5.6) \quad \Delta \tilde{t}^{k+1} \approx \left[\frac{F'(T^*/2)}{G'(T^*/2)} \right] \Delta \tilde{t}^k$$

where we have used

$$(5.7) \quad \left[(G^{-1})'(F(t)) \right] \Big|_{t=T^*/2} = \frac{F'(T^*/2)}{G'(T^*/2)},$$

which follows from $F(T^*/2) = V^*$ and $(G^{-1})'(V^*) = \frac{1}{G'(T^*/2)}$. If $\Delta t^0 = \Delta \tilde{t}^0 + T^*/2$ is the initial condition for the firing map, then

$$(5.8) \quad \Delta \tilde{t}^k = \Delta \tilde{t}^0 \left[\frac{F'(T^*/2)}{G'(T^*/2)} \right]^k.$$

It follows that the fixed point $T^*/2$ is stable when

$$(5.9) \quad -1 < \frac{F'(T^*/2)}{G'(T^*/2)} < 1.$$

Sections 5.2 and 5.3 find specific values for $T^*/2$, V^* , $F'(T^*/2)$, and $G'(T^*/2)$ for δ -function synapses and exponential synapses.

5.1.4. Calculate PRC of HCO. We calculate the PRC of the HCO by giving small pulses of size ϵ ($\epsilon \ll 1$) to cell 1 at various phases (t_θ) in the period of the HCO during stable anti-phase oscillations. We take $\Delta \tilde{t}^0$ as the change in firing time of cell 1 following the perturbation. If Δt^0 is the firing time of cell 1 following the perturbation, then

$$(5.10) \quad \Delta t^0 = T^*/2 + \Delta \tilde{t}^0.$$

Once we know the small perturbation $\Delta \tilde{t}^0$, we can use the linearized firing map to find each subsequent firing times. When finding $\Delta \tilde{t}^0$, there are two scenarios to consider. In scenario

1, the pulse is given to cell 1 while cell 1 is lagging, and in scenario 2, the pulse is given to cell 1 while cell 1 is leading. We denote the phase of the HCO by θ , and the time of the perturbation used to measure the PRC by t_θ ($0 < t_\theta < T^*$).

5.1.5. Scenario 1: $0 < t_\theta < T^*/2$. For this scenario, we let cell 1 begin at $V_1(0) = 0$ and cell 2 begin at $V_2(0) = V^*$, i.e. cell 1 is lagging and cell 2 is leading. If the perturbation is given to cell 1 between time $0 < t_\theta < T^*/2$, then the next cell to fire is cell 2 at time $T^*/2$. At this time, cell 1 has moved to

$$(5.11) \quad V^0 = V_A(T^*/2; 0) + \epsilon e^{t_\theta - T^*/2} = V^* + \epsilon e^{t_\theta - T^*/2}$$

where $\epsilon e^{t_\theta - T^*/2}$ is the phase response of cell 1 to the small perturbation given at t_θ . After cell 2 is reset at $t = T^*/2$, cell 1 is the leading cell until it fires when

$$(5.12) \quad V_B(\Delta t^0; V^0) = 1.$$

5.1.6. Scenario 2: $T^*/2 < t_\theta < T^*$. For this scenario, we let cell 1 begin at $V_1(T^*/2) = V^*$ and cell 2 begin at $V_2(T^*/2) = 0$, i.e. cell 1 is leading and cell 2 is lagging. If the perturbation is given to cell 1 between time $T^*/2 < t_\theta < T^*$, then the next cell to fire is cell 1 when

$$(5.13) \quad V_B(\Delta t^0; V^*) + \epsilon e^{t_\theta - \Delta t^0} = 1$$

where $\epsilon e^{t_\theta - \Delta t^0}$ is the phase response of cell 1 to the perturbation given at t_θ . Δt^0 is found analytically for δ -function synapses in section 5.2 and numerically for exponential synapses in section 5.3. $\Delta \tilde{t}^0$ is found from equation (5.10).

5.1.7. Timing. To calculate the PRC of the HCO, we take the difference in firing times from the perturbed and unperturbed system (denoted by $\Delta\theta$). If no perturbation is given to the system, then the firing times during steady state oscillations are

$$(5.14) \quad t_{UP}^k = (k+1) \frac{T^*}{2}, \quad k \in \mathbb{Z}$$

where UP stands for ‘unperturbed’. When the ϵ -pulse is given to cell 1, the new firing times are

$$(5.15) \quad t^k = \Delta t^0 + \sum_{i=0}^{k-1} \Delta t^{i+1}$$

$$(5.16) \quad t^k = \Delta t^0 + \sum_{i=0}^{k-1} G^{-1}(F(\Delta t^i))$$

$$(5.17) \quad t^k \approx \Delta t^0 + \sum_{i=0}^{k-1} G^{-1}(F(T^*/2 + \epsilon \Delta \tilde{t}^i))$$

$$(5.18) \quad t^k \approx \Delta t^0 + \sum_{i=0}^{k-1} [G^{-1}(F(T^*/2)) + \epsilon \Delta \tilde{t}^i F'(T^*/2)(G^{-1})'(F(T^*/2))]$$

$$(5.19) \quad t^k \approx \Delta t^0 + kG^{-1}(F(T^*/2)) + \epsilon F'(T^*/2)(G^{-1})'(F(T^*/2)) \sum_{i=0}^{k-1} \Delta \tilde{t}^i$$

$$(5.20) \quad t^k \approx \Delta t^0 + k \frac{T^*}{2} + \epsilon \frac{F'(T^*/2)}{G'(T^*/2)} \Delta \tilde{t}^0 \sum_{i=0}^{k-1} \left[\frac{F'(T^*/2)}{G'(T^*/2)} \right]^i$$

$$(5.21) \quad t^k \approx (k+1) \frac{T^*}{2} + \epsilon \Delta \tilde{t}^0 + \epsilon \frac{F'(T^*/2)}{G'(T^*/2)} \Delta \tilde{t}^0 \frac{1 - \left[\frac{F'(T^*/2)}{G'(T^*/2)} \right]^k}{1 - \frac{F'(T^*/2)}{G'(T^*/2)}}.$$

We used the linearized firing map (equation (5.8)) in (5.17)-(5.20), and solved the summation in (5.21).

5.1.8. $k/2^{th}$ order PRC of HCO. The change in phase $\Delta\theta^k$ is given by the change in firing times $t_{UP}^k - t^k$, normalized for the size of the ϵ -pulse.

$$(5.22) \quad \Delta\theta^k = \Delta \tilde{t}^0 \left(-1 - \frac{1 - \left[\frac{F'(T^*/2)}{G'(T^*/2)} \right]^k}{\frac{G'(T^*/2)}{F'(T^*/2)} - 1} \right).$$

$\Delta\theta^k$ is the $k/2^{th}$ order PRC, i.e. the PRC after $k/2$ firings. Note that $\Delta\theta^k$ has the same form as in chapter 4.

5.1.9. Semi-Analytic PRC of HCO. The PRC of the HCO is the asymptotic change in phase shift that results from the perturbation, $\lim_{k \rightarrow \infty} \Delta\theta^k$. If the stability condition

for the anti-phase state is met (equation (5.9)), then the resulting PRC of the HCO is

$$(5.23) \quad \Delta\theta = \Delta\tilde{t}^0 \left(-1 - \frac{1}{\frac{G'(T^*/2)}{F'(T^*/2)} - 1} \right).$$

Equation (5.23) is analytic or semi-analytic, depending on τ .

5.2. δ -function synapses

In this section, we consider the limiting case of $\tau \rightarrow 0$, i.e. the two LIF cells are coupled with δ -function synapses. To find the PRC of the HCO we first find the half-cycle solutions $V_{LC}(t; 0)$ and $V_{LC}(t; V^k)$ as well as functions $G(t)$ and $F(t)$. We then find the stable fixed point $T^*/2$ and the corresponding voltage V^* . Finally, we find $\Delta\tilde{t}^0$ and combine the information to get the $k/2^{th}$ order PRC and infinitesimal PRC of the HCO.

Half-cycle solution. The equations governing the HCO coupled with δ -function synapses are

$$(5.24) \quad \begin{aligned} \frac{dV_1}{dt} &= I - V_1 - \alpha\delta(V_2) & \text{if } V_1 = 1, V_1 \leftarrow 0; & & V_1(0) = 0 \\ \frac{dV_2}{dt} &= I - V_2 - \alpha\delta(V_1) & \text{if } V_2 = 1, V_2 \leftarrow 0; & & V_2(0) = V^k - \alpha. \end{aligned}$$

The half-cycle solution is

$$(5.25) \quad V_A(t; 0) = I(1 - e^{-t})$$

$$(5.26) \quad V_B(t; V^k - \alpha) = I(1 - e^{-t}) + (V^k - \alpha)e^{-t}.$$

Note that as $\tau \rightarrow 0$ in equation (5.2), $\frac{\alpha}{\tau-1}(e^{-t} - e^{-t/\tau}) \rightarrow -\alpha e^{-t}$.

G(t) and F(t). We find functions $G(t)$ and $F(t)$ as described in section 5.1.1. We then find $G'(t)$ and $F'(t)$ to use in the PRC for the HCO. We find V^k from $V_B(t; V^k - \alpha) = 1$ and call this function $G(t)$.

$$(5.27) \quad G(t) = (1 - I)e^t + \alpha + I.$$

Then

$$(5.28) \quad G'(T^*/2) = (1 - I)e^{T^*/2}.$$

Let $F(t) = V_A(t; 0)$. Then

$$(5.29) \quad F(t) = I(1 - e^{-t}),$$

and

$$(5.30) \quad F'(T^*/2) = Ie^{-T^*/2}.$$

$T^*/2$, V^* , and $\Delta\tilde{t}^0$. We use the firing map $T^*/2 = G^{-1}(F(T^*/2))$ where $F(T^*/2) = V^*$ to solve for V^* and $T^*/2$.

$$(5.31) \quad T^*/2 = \ln\left(\frac{I - (V^* - \alpha)}{I - 1}\right)$$

$$(5.32) \quad V^* = \frac{1}{2}((\alpha + 2I) - \sqrt{(\alpha + 2I)^2 - 4I(1 + \alpha)}).$$

For scenario 1, we use

$$(5.33) \quad V_B(\Delta t^0; V^* + \epsilon e^{t_\theta - T^*/2}) = 1$$

to find Δt^0 .

$$(5.34) \quad \begin{aligned} \Delta t^0 &= \ln\left(\frac{I - (V^* - \alpha) - \epsilon e^{t_\theta - T^*/2}}{I - 1}\right) \\ &\approx \ln\left(\frac{I - (V^* - \alpha)}{I - 1}\right) - \epsilon e^{t_\theta - T^*/2} \frac{1}{I - (V^* - \alpha)} \\ &\approx T^*/2 - \epsilon e^{t_\theta - T^*/2} \frac{1}{I - (V^* - \alpha)} \end{aligned}$$

where we have linearized about $\epsilon = 0$. Since $\Delta t^0 = T^*/2 + \epsilon \Delta\tilde{t}^0$,

$$(5.35) \quad \Delta\tilde{t}^0 = -e^{t_\theta - T^*/2} \frac{1}{I - (V^* - \alpha)}.$$

For scenario 2, we use

$$(5.36) \quad V_B(\Delta t^0; V^*) + \epsilon e^{t_\theta - \Delta t^0} = 1$$

to find Δt^0 .

$$\begin{aligned}
 (5.37) \quad \Delta t^0 &= \ln \left(\frac{I - (V^* - \alpha) - \epsilon e^{t_\theta}}{I - 1} \right) \\
 &\approx \ln \left(\frac{I - (V^* - \alpha)}{I - 1} \right) - \epsilon e^{t_\theta} \frac{1}{I - (V^* - \alpha)} \\
 &\approx T^*/2 - \epsilon e^{t_\theta} \frac{1}{I - (V^* - \alpha)}
 \end{aligned}$$

where we have linearized about $\epsilon = 0$. Since $\Delta t^0 = T^*/2 + \epsilon \Delta \tilde{t}^0$,

$$(5.38) \quad \Delta \tilde{t}^0 = -e^{t_\theta} \frac{1}{I - (V^* - \alpha)}.$$

$k/2^{th}$ order PRC of HCO.

$$(5.39) \quad \Delta \theta^k = \begin{cases} e^{-T^*/2} \cdot \frac{e^{t_\theta}}{I} \cdot \frac{I}{I - (V^* - \alpha)} \left(1 + \frac{1 - \left[\frac{Ie^{-T^*}}{(1-I)} \right]^k}{Ie^{-T^*} - 1} \right), & 0 < t_\theta < T^*/2 \\ \frac{e^{t_\theta}}{I} \cdot \frac{I}{I - (V^* - \alpha)} \left(1 + \frac{1 - \left[\frac{Ie^{-T^*}}{(1-I)} \right]^k}{Ie^{-T^*} - 1} \right), & T^*/2 < t_\theta < T^*. \end{cases}$$

Analytically derived PRC of HCO.

$$(5.40) \quad \Delta \theta = \begin{cases} e^{-T^*/2} \cdot \frac{e^{t_\theta}}{I} \cdot \frac{I}{I - (V^* - \alpha)} \left(1 + \frac{1}{Ie^{-T^*} - 1} \right), & 0 < t_\theta < T^*/2 \\ \frac{e^{t_\theta}}{I} \cdot \frac{I}{I - (V^* - \alpha)} \left(1 + \frac{1}{Ie^{-T^*} - 1} \right), & T^*/2 < t_\theta < T^*. \end{cases}$$

Equations (5.39) and (5.40) show that the PRC of the HCO is a product of the single cell PRC and an attenuation factor, as in chapter 4. In each half of the PRC, the attenuation factor is a function of the applied current I , the synaptic strength α , the fixed point $T^*/2$, and the corresponding voltage V^* . Recall that T^* and V^* are parameterized by I and α . Note that the attenuation factor in the first half has an extra term $e^{-T^*/2}$. Figure 5.2 shows the attenuation of each half of the HCO PRC when the LIF cells are coupled with δ -function synapses. The extra term in the first half of the HCO PRC leads to greater attenuation in the first half compared to the second half.

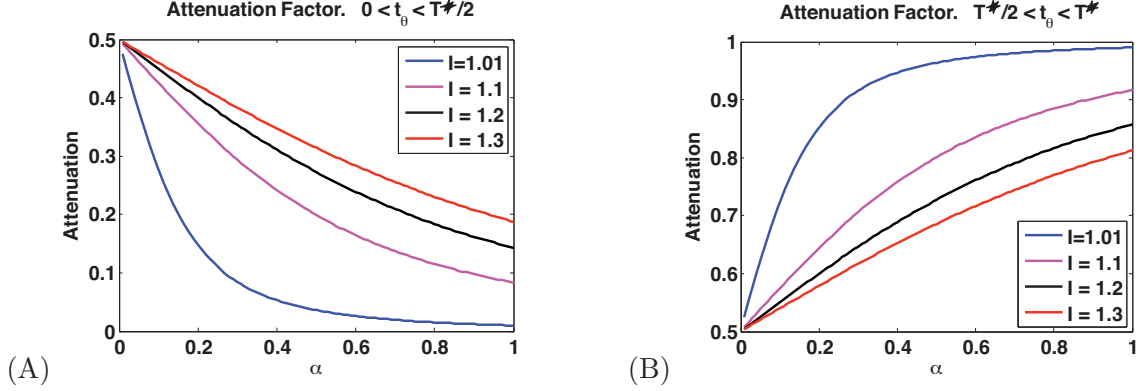


FIGURE 5.2. Attenuation factors for the PRC of the HCO with δ -function synapses (equation (5.40)). (A) First half of the PRC ($0 < t_\theta < T^*/2$). (B) Second half of the PRC ($T^*/2 < t_\theta < T^*$).

5.3. Exponential synapses

In this section we consider exponential synapses with sufficiently fast decay, i.e. τ is such that

$$(5.41) \quad \int_0^{T^*/2} e^{-t/\tau} dt \geq pT^* \implies \frac{\tau}{T^*} \leq \frac{1}{-2 \ln(1-p)},$$

i.e. within one-half HCO period, $p\%$ or more of the synaptic current has been triggered. For instance, if $p = 95\%$, then the rate of decay relative to the HCO period is $\tau/T^* \leq 17\%$. As $p \rightarrow 1$, τ/T^* decreases. To find semi-analytical solutions for the PRC of the HCO, we first use the half-cycle solutions $V_A(t; 0)$ and $V_B(t; V^k)$ to find functions $G(t)$ and $F(t)$. We find V^* , T^* , \tilde{t}^0 , and \tilde{V}^0 numerically to get the $k/2^{\text{th}}$ order PRC and the infinitesimal PRC of the HCO.

Half-cycle solution ($\tau \neq 1$).

$$(5.42) \quad V_A(t; 0) = I(1 - e^{-t})$$

$$(5.43) \quad V_B(t; V^k) = I(1 - e^{-t}) + \frac{\alpha}{\tau - 1} (e^{-t} - e^{-t/\tau}) + V^k e^{-t}$$

G(t) and F(t). Solve $V_B(t; V^k) = 1$ for V^k and call this function $G(t)$.

$$(5.44) \quad G(t) = e^t + I(1 - e^t) - \frac{\alpha}{\tau - 1} (1 - e^{t(\frac{\tau-1}{\tau})})$$

$$(5.45) \quad G'(T^*/2) = (1 - I)e^{T^*/2} + \frac{\alpha}{\tau} e^{T^*/2(\frac{\tau-1}{\tau})}$$

Let $F(t) = V_A(t)$

$$(5.46) \quad F(t) = I(1 - e^{-t})$$

$$(5.47) \quad F'(T^*/2) = Ie^{-T^*/2}$$

$T^*/2$, V^* , and Δt^0 . We use the firing map $T^*/2 = G^{-1}(F(T^*/2))$ where $F(T^*/2) = V^*$ to solve for V^* and $T^*/2$. This is done numerically because the $e^{-t/\tau}$ term makes it impossible to solve analytically.

For scenario 1, i.e. small perturbations delivered to cell 1 in the first half of the HCO cycle ($0 \leq t_\theta < T^*/2$), we use

$$(5.48) \quad V_B(\Delta t^0; V^* + \epsilon e^{t_\theta - T^*/2}) = 1$$

to find Δt^0 numerically.

For scenario 2, i.e. small perturbations delivered to cell 1 in the second half of the HCO cycle ($T^*/2 \leq t_\theta < T^*$), we use

$$(5.49) \quad V_B(\Delta t^0; V^*) + \epsilon e^{t_\theta - \Delta t^0} = 1$$

to find Δt^0 numerically. We find Δt^0 from equation (5.10).

5.4. Examples

In this section we explore how the PRC of the HCO depends on the single cell intrinsic dynamics and synaptic coupling within the HCO. Figure 5.3A shows the single cell PRC for $\alpha = .1$ and $I = 1.1$. Figure 5.3B shows the analytical PRC (dark blue), the numerically generated PRC (pink), and the k^{th} order PRCs of the HCO with δ -function synapses. Figure 5.4A,B shows the same data for the HCO with exponential synapses when $\tau = 0.3$ ($\tau/T^* = 10.7\%$) and $\tau = 0.5$ ($\tau/T^* = 17.5\%$). Comparing the PRCs of the HCOs to the single cell PRC, we see that the qualitative shape is similar, but there is attenuation in both halves of the PRC. Figure 5.2 shows how this attenuation depends on α and I for δ -function synapses only.

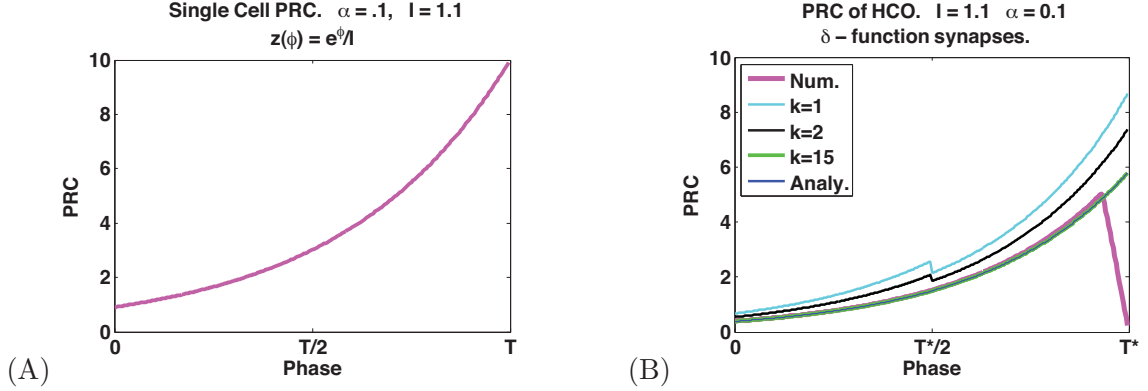


FIGURE 5.3. Single cell PRC and PRC of HCO with δ -function synapses. $\alpha = .1$ and $I = 1.1$. (A) Single cell PRC. (B) Numerically generated PRC, analytic PRC, and k^{th} order PRC of the HCO.

When $\tau = 0.3$, the synapse decays according to condition (5.41), i.e. the synapse decays sufficiently fast. When $\tau = 0.5$ and larger, the synapse does not obey equation (5.41), but the analytic HCO PRC is still a close approximation to the numerically generated PRC. Note that condition (5.41) ensures the synapse will decay sufficiently fast and the analytically derived PRC will be a good approximation to the numerically derived PRC. However, this condition can be relaxed substantially. In fact, the analytic HCO PRC using δ -function synapses also gives a close approximation to the numerically generated HCO PRC for larger values of τ because only small quantitative differences appear in the HCO PRC, as for the phase model. This implies that the PRC of the LIF HCO with δ -function synapses is a good approximation to the PRC of the LIF HCO with synapses that decay within one-half HCO period.

Figures 5.5, and 5.6 show the convergence rate of the $k/2^{th}$ order PRCs for various α . We determine the rate of convergence using the norm from chapter 4, equation (4.36). We say the k^{th} order PRC has converged when this norm is less than 1×10^{-2} . The convergence rate of the approximation is determined by the slope of the firing map at the fixed point. If $|F'(T^*/2)/G'(T^*/2)| < 1$ then the fixed point will be stable, but the smaller this ratio is, the faster the approximations will converge. If the cells in the HCO are coupled with δ -function synapses, then

$$(5.50) \quad \frac{F'(T^*/2)}{G'(T^*/2)} = \frac{I}{(1-I)} e^{-T^*}.$$

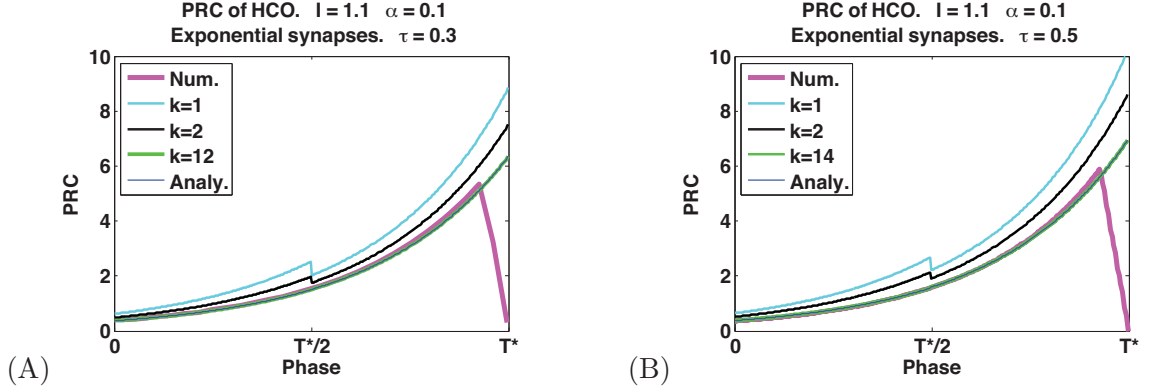


FIGURE 5.4. PRC of HCO with exponential synapses. $\alpha = .1$ and $I = 1.1$. Numerically generated PRC, analytic PRC, and k^{th} order PRC of the HCO. (A) $\tau = 0.3$. (B) $\tau = 0.5$.

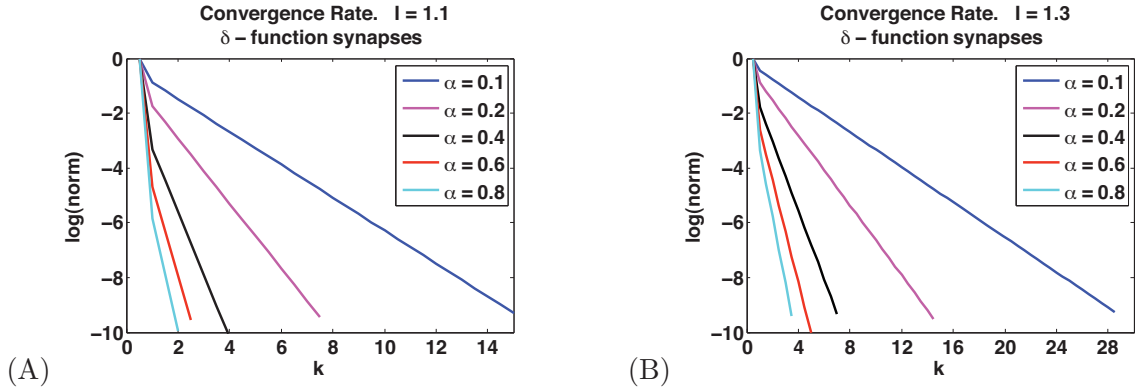


FIGURE 5.5. Convergence rate of the k^{th} order PRC (equation (5.22)) for a range of synaptic strengths α when the cells are coupled with δ -function synapses. (A) $I = 1.1$ and (B) $I = 1.3$.

If the cells are coupled with non-summing exponential synapses, then

$$(5.51) \quad \frac{F'(T^*/2)}{G'(T^*/2)} = \frac{Ie^{-T^*}}{(1-I) + \frac{\alpha}{\tau}e^{\frac{\tau-1}{\tau}}}.$$

In equations (5.50) - (5.51) we see that the convergence rate depends on α . As α increases, T^* increases, and the convergence rate decreases. This is clear in figures 5.5, and 5.6 as well. We can also see that as I increases, the convergence rate decreases. Finally, as τ increases, T^* increases and the convergence rate increases. As τ increases, the synapses decay slower, which makes the HCO more sensitive to perturbations. The increased sensitivity is most notable in the second half of the period. This translates to a larger amplitude in the PRC of the HCO.

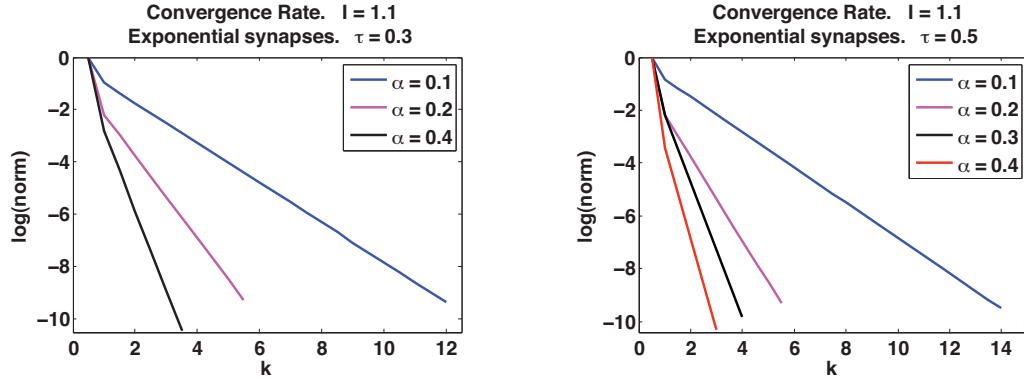


FIGURE 5.6. Convergence rate of the k^{th} order PRC (equation (5.22)) for a range of synaptic strengths α when the cells are coupled with non-summing exponential synapses. (A) $I = 1.1$ and (B) $I = 1.3$.

5.5. Summary

- When the cells in the HCO are described by the LIF model and coupled with δ -function synapses or exponential synapses, the PRC of the HCO is a product of the single cell PRC and an attenuation factor, as in chapter 4.
- As opposed to the phase model in chapter 4, using the LIF model in the HCO allowed us to find a semi-analytic solution to the HCO PRC when the cells are coupled with exponential synapses with sufficiently fast decay.
- The analysis in this chapter can be extended to synapses with slower decay and summing synapses by using higher order firing maps.

CHAPTER 6

Phase Locking Dynamics in a Chain of Half-Center Oscillators

In this chapter, we use numerical simulations and the theory of weakly coupled oscillators (TWCO) to study the phase-locking properties of short chains of idealized HCOs. The dynamics of the cells in each HCO are described by either coupled one-variable phase models (as in chapter 4) or leaky integrate-and-fire neurons (as in chapter 5). The chain of four HCOs models the crayfish swimmeret system.

As described in chapter 2, activity in the isolated neural circuit of crayfish swimmeret system is controlled by four pairs of CPGs, with one CPG per hemisegment. The CPGs are coupled through ascending and descending intersegmental interneurons to create a distributed system of coupled non-linear oscillators. The isolated nervous system can exhibit fictive swimming, with power stroke and return stroke motor neurons in each segment firing in anti-phase. The system demonstrates a phase lag of 25% between segments, with the most posterior segments leading the rhythm. As few as two segments can reproduce this characteristic phase lag.

Here, we model the chain of CPGs from one segment to four segments. We model the intersegmental connectivity with a square pulse $I(\phi_i)$, i.e. the current has instantaneous activation and deactivation. In equation (6.1), dc represents the duty cycle of the coupling, and ϕ_i is the phase of HCO i .

$$(6.1) \quad I(\phi_i) = \begin{cases} 0.2, & \text{for } 0 \leq \phi_i < dc \cdot T^* \\ 0, & \text{for } dc \cdot T^* \leq \phi_i < T^*. \end{cases}$$

Recently, the gradient of intersegmental synaptic strengths have been elucidated [SHM09]. We incorporate this information into the amplitude of the square pulse (see figure 6.1).

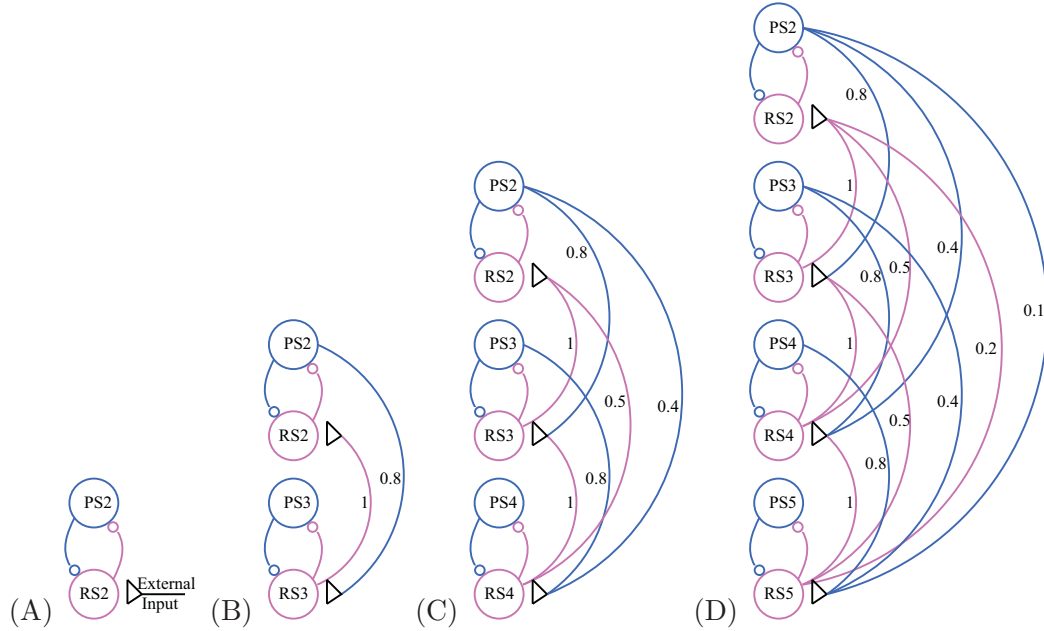


FIGURE 6.1. Schematic diagram of the intersegmental coupling and strengths for (A) one (B) two (C) three and (D) four segments. Labels on connections indicate relative strengths.

In this chapter, the duty cycle of intersegmental input is altered and found to play an important role in determining the ability of chains of HCOs to phase-lock.

6.1. Intersegmental Connectivity

Figure 6.1 shows a schematic diagram of the intersegmental coupling and strengths for one, two, three, and four segments. The one segment “network” is an externally forced HCO; the other cases are synaptically coupled HCOs. Note the two asymmetries in the coupling: First, in these models, ascending connections originate from return-stroke (RS) neurons and descending connections originate from the power-stroke (PS) neurons in their home segment. All connections project to the RS neurons in their target segment. Second, ascending projections are stronger than their descending counterparts. There is a gradient of strengths with nearest neighbor connections being the strongest and the farthest connections having the weakest strength [SHM09] (the relative coupling strengths are shown in figure 6.1).

6.2. Numerical simulations in a chain of HCOs

The following numerical simulations use the δ -pulse-coupled HCO phase model (equation 4.6) described in chapter 4 and the δ -pulse-coupled HCO LIF model (equation 5.1

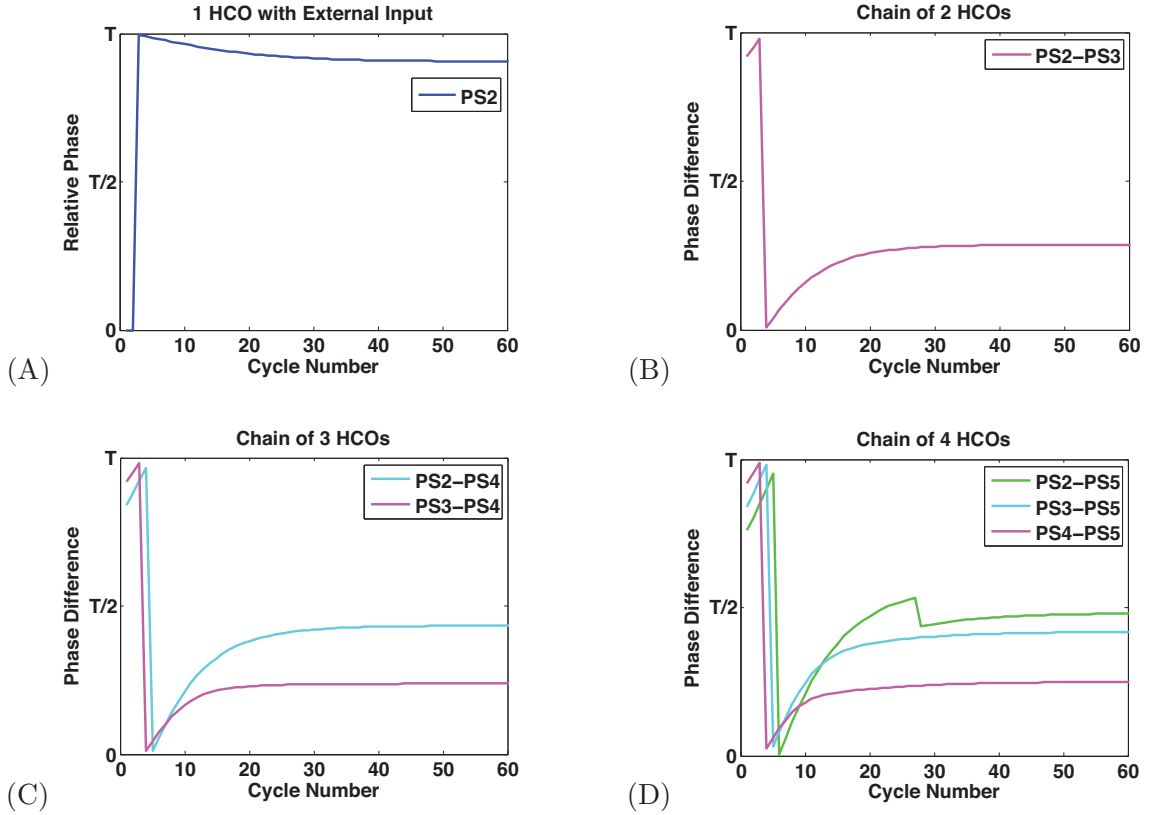


FIGURE 6.2. Numerical simulations in chain lengths of (A) one segment, (B) two segments, (C) three segments, (D) four segments. (A) Cycle number represents the number of cycles in the external input. The phase of the PS neuron is shown relative to the external input. (B-D) Cycle number represents the number of cycles in the most posterior PS neuron in the chain. The phase of each PS neuron in the chain is taken at the beginning of each cycle. The phase difference between each segment and the most posterior segment in the chain is shown. Each segment is modeling using the phase model from chapter 4. $\beta = 0.25$, $\alpha = 2$ and duty cycle is $0.5T^*$.

with $\tau \rightarrow 0$) described in chapter 5. The connectivity between the HCOs is described in section 6.1. Figures 6.2, 6.3, and 6.4 examine the phase-locking dynamics that occur in chain lengths of one through four segments. Figures 6.2 and 6.3 use the phase model HCO from chapter 4 and figure 6.4 uses the LIF HCO model from chapter 5. In panels (A), cycle number represents the number of cycles in an external T^* -periodic input. The phase of the PS neuron is shown relative to the external input. In panels (B)-(D), cycle number represents the number of cycles in the most posterior PS neuron in the chain. The phase of each PS neuron in the chain is taken at the beginning of each cycle when the most posterior segment is reset to 0. The phase difference between each segment and the most posterior segment in the chain is shown.

In figure 6.2, we use $\beta = 0.25$ and $\alpha = 2$. Recall that β describes the single cell skewness factor of the single cell PRC and α is the synaptic strength between the cells in the HCO. The duty cycle of intersegmental connections is $0.5T^*$, i.e. the synapse is ‘on’ for one-half HCO period and ‘off’ for one-half HCO period. Here, cycle number is equivalent to time progressing. With these parameters, the system phase-locks for each chain length. In figure 6.2A, the phase of the PS neuron is shown relative to the external input. The phase delay is almost one period. This shows that the HCOs are capable of phase-locking with an external force of the same period as the HCO. It also suggests that in a chain of HCOs with nearest-neighbor ascending-only coupling, there would be a quick wave moving from anterior to posterior followed by a period of silence. In figure 6.2B, phase-locking is shown for a chain length of 2 segments. The phase lag between segments is approximately 25%. This is the same phase delay seen in the crayfish swimmeret system. When the chain length increases to 3 segments in figure 6.2C, the phase lag between the two most posterior segments remains at 25%, and the phase lag between the two anterior segments decreases to slightly less than 25%. However, when the chain length is increased to four segments in figure 6.2D, the phase lag between segments 4 and 5 is substantially less than 25% and the phase-lag between segments in the chain is not constant. The phase lag between segments decreases from 25% moving anteriorly, i.e. as the length of the chain increases, there is no apparent predictable behavior in the phase difference between segments.

In figure 6.3, the duty cycle of intersegmental connections is $0.9T^*$. With the increased duty cycle, phase-locking is still possible in chain lengths of 1 and 2 segments, but is no longer possible in chain lengths of 3 and 4 segments. This demonstrates that phase-locking in short chain lengths does not imply that phase-locking will persist in longer chains. In figure 6.3A, the phase lag is 50% and in figure 6.3B, the phase lag between segments is slightly greater than 75%. Neither exhibit a phase lag close to the 25% phase lag seen in the crayfish. In figure 6.3C, the phase lag between segments exhibits periodic oscillations. In figure 6.3D, the phase lag between segments demonstrates very complex behavior with no phase-locking and no periodic activity.

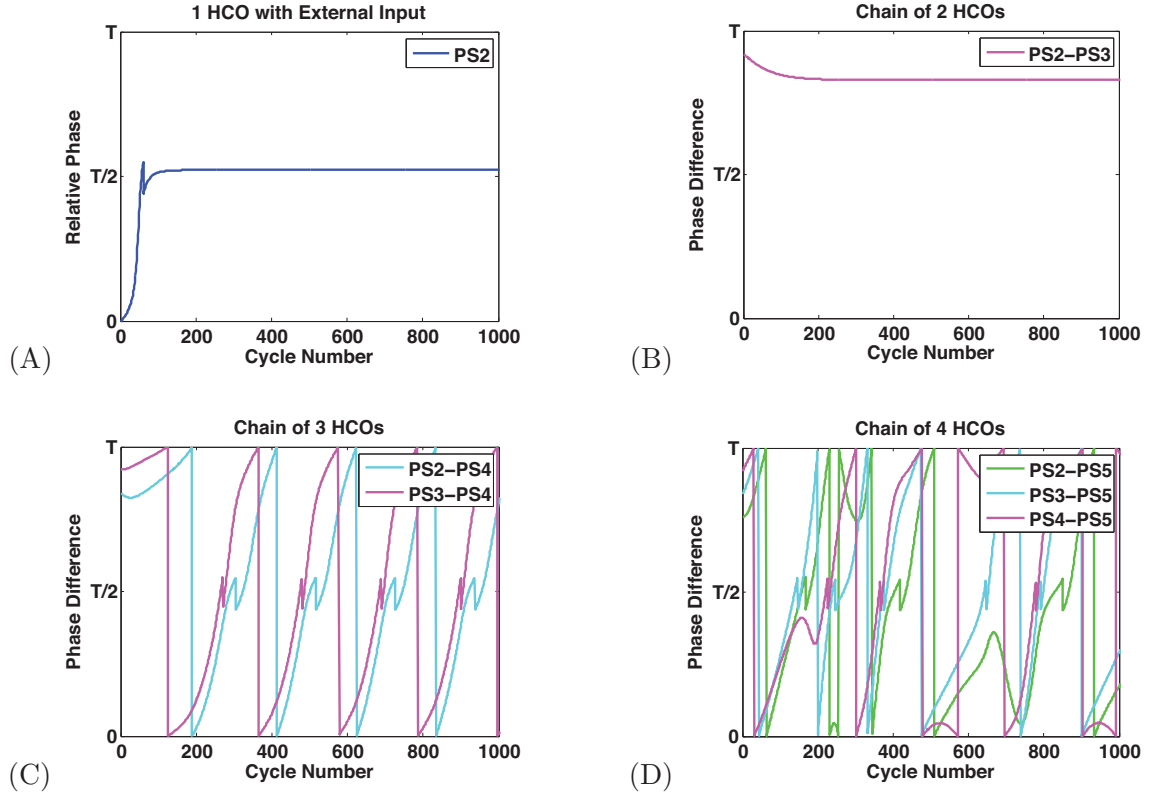


FIGURE 6.3. Numerical simulations in chain lengths of (A) one segment, (B) two segments, (C) three segments, (D) four segments. (A) Cycle number represents the number of cycles in the external input. The phase of the PS neuron is shown relative to the external input. (B-D) Cycle number represents the number of cycles in the most posterior PS neuron in the chain. The phase of each PS neuron in the chain is taken at the beginning of each cycle. The phase difference between each segment and the most posterior segment in the chain is shown. Each segment is modeling using the phase model from chapter 4. $\beta = 0.25$, $\alpha = 2$ and duty cycle is $0.9T^*$.

For the phase model HCO, duty cycle of coupling was found to play the biggest role in phase-locking ability. Figure 6.5 details the phase-locking ability of each chain length for various skewness factors (β) and synaptic strengths (α). ‘Yes PL’ means the chain does phase-lock and ‘No PL’ means the chain does not phase-lock. A duty cycle of $0.5T^*$ maintains the best phase-locking ability for all chain lengths, skewness factors and synaptic strengths explored.

In figure 6.4, the LIF model from chapter 5 is used. We use parameters $I = 1.1$, $\alpha = 1$ and a duty cycle of $0.5T^*$. With these parameters, phase-locking only exists in the chain of two segments. In figure 6.4A, the phase of the PS neuron is shown relative to the external input. The PS neuron does not phase-lock with external input. In figure 6.2B, phase-locking is shown for a chain length of 2 segments. We see that the phase lag between segments is approximately 75%, very different from the phase lag of 25% seen in the crayfish. When

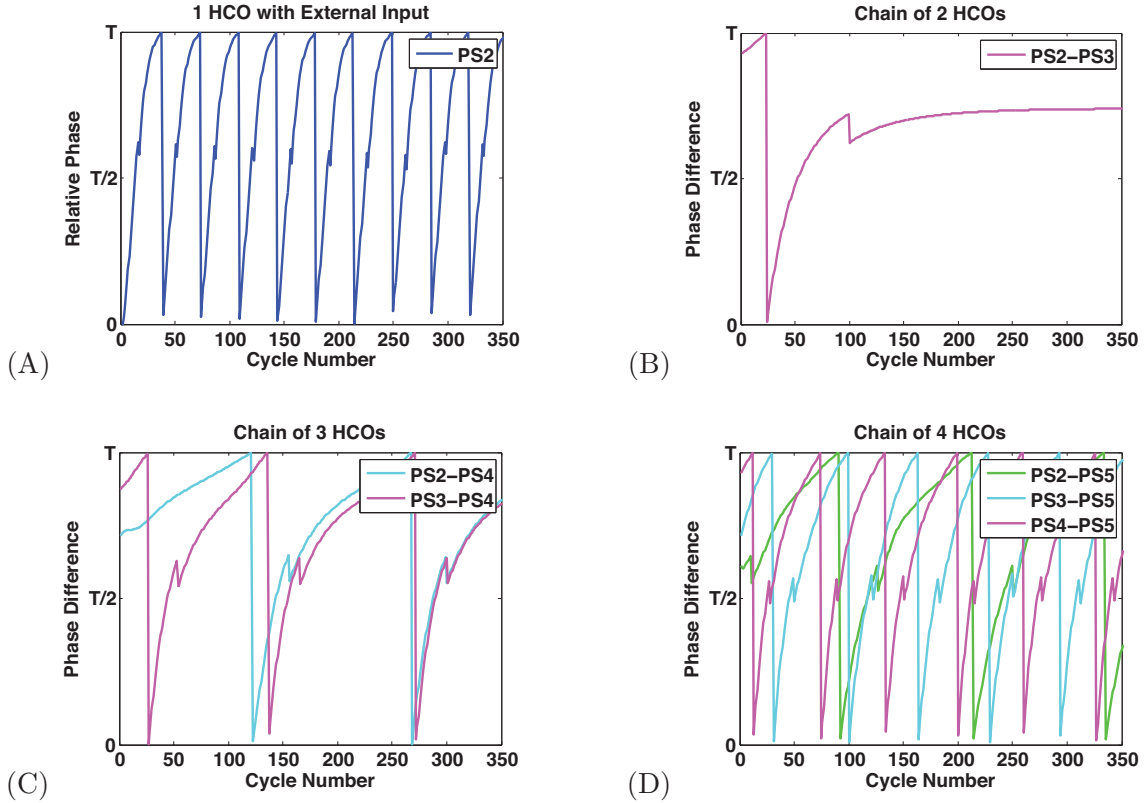


FIGURE 6.4. Numerical simulations in chain lengths of (A) one segment, (B) two segments, (C) three segments, (D) four segments. (A) Cycle number represents the number of cycles in the external input. The phase of the PS neuron is shown relative to the external input. (B-D) Cycle number represents the number of cycles in the most posterior PS neuron in the chain. The phase of each PS neuron in the chain is taken at the beginning of each cycle. The phase difference between each segment and the most posterior segment in the chain is shown. Each segment is modeling using the LIF model from chapter 5. $\alpha = 0.1$, $I = 1.1$ and duty cycle is $0.5T^*$.

the chain length increases to three and four segments in figure 6.4C and 6.4D, phase-locking is lost. These figures further demonstrate that there is no apparent predictable behavior in the phase lag between segments for different chain lengths. Furthermore, phase-locking is not seen for different duty cycles, applied currents, or synaptic strengths. This suggests that the LIF HCO model is not a good model for the crayfish swimmeret system because it can not replicate the phase-locking ability.

6.3. Applying the theory of weakly coupled oscillators (TWCO)

The TWCO uses singular perturbation methods to separate the properties of the circuit controlling each module (the local oscillators) from the properties of the coordinating information arriving from other modules (the coupling between oscillators). A phase response

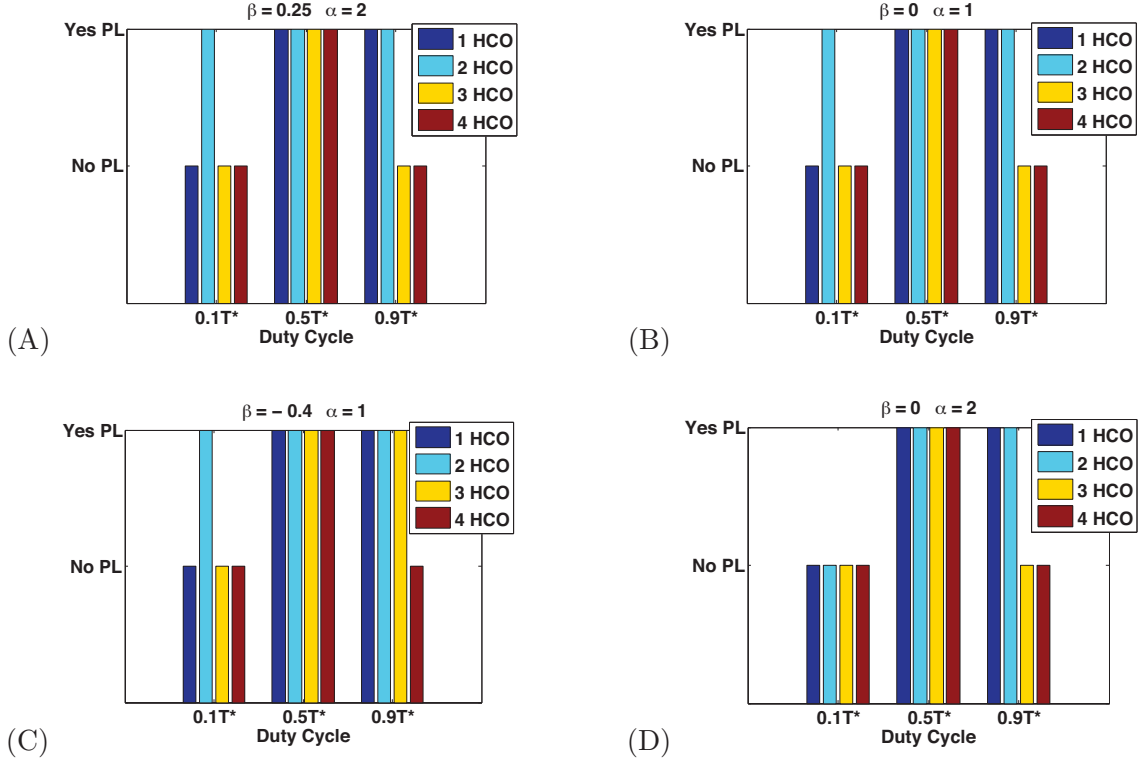


FIGURE 6.5. Bar graphs detailing phase-locking in various chain lengths for duty cycles of $0.1T^*$, $0.5T^*$, and $0.9T^*$. 'Yes PL' means the chain does phase-lock. 'No PL' means the chain does not phase-lock. Each segment is modeling using the phase model from chapter 4. (A) $\beta = 0.25$ and $\alpha = 2$. (B) $\beta = 0$ and $\alpha = 1$. (C) $\beta = -0.4$ and $\alpha = 1$. (D) $\beta = 0$ and $\alpha = 2$.

curve (PRC) quantifies the phase shifts of an oscillator in response to an abrupt perturbation as a function of the phase at which the perturbation occurs. When the perturbation from coupling between oscillators is not too large, the dynamics of the oscillators can be completely captured by their phase and their PRCs. This reduces the dimension of the system and allows the analysis of phase-locking to be more tractable. We apply the TWCO to the coupled HCO system in which each HCO is an oscillatory unit, not the single cells.

Equation (6.2) describes how the relative phase of HCO i (i.e. the phase of the oscillator relative to the unperturbed oscillator) changes over time as a function of the phase response curve of HCO i , $z(\phi_i)$, and the input coming into the HCO from the other oscillators I . For the four segment system,

$$(6.2) \quad \frac{d\phi_i}{dt} = \frac{1}{T^*} \int_0^{T^*} z(\tilde{t} + \phi_i) \sum_{j=1}^4 w_{j,i} I \left(\tilde{t} + \phi_j + d_{j,i} \frac{T^*}{2} \right) d\tilde{t}, \quad i = 1, \dots, 4$$

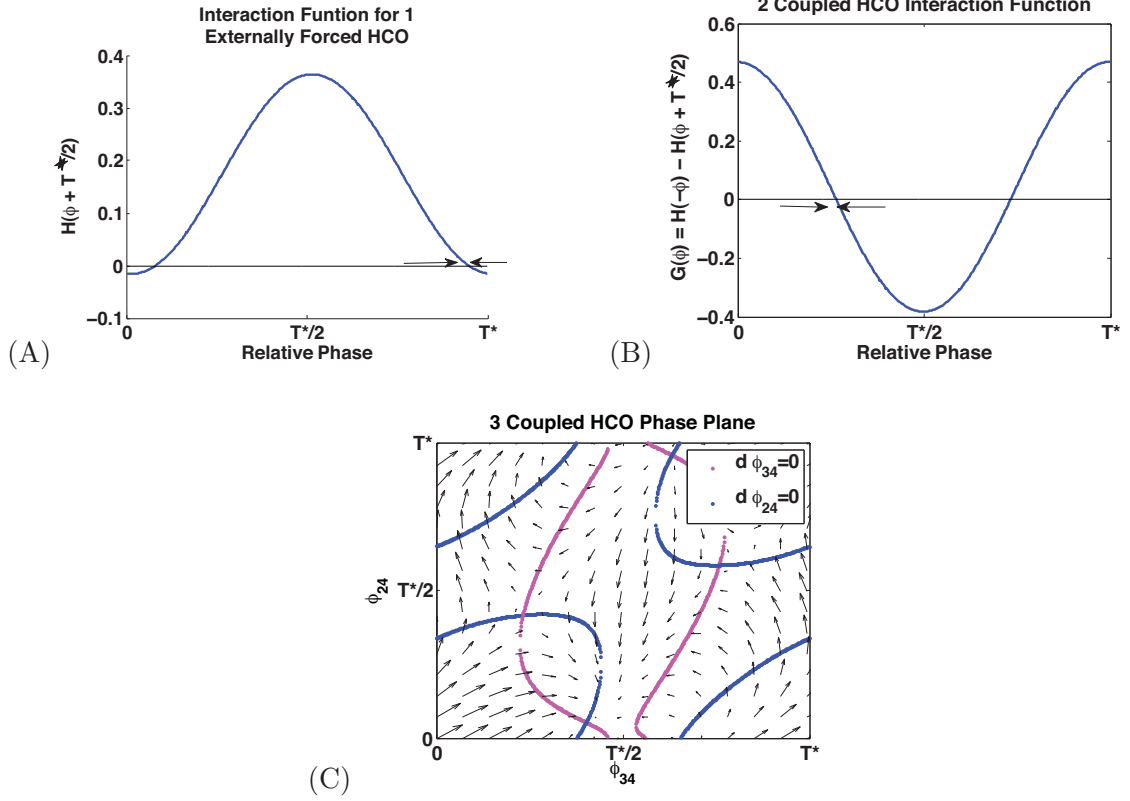


FIGURE 6.6. Phase differences using the TWCO for chain lengths of one through three segments. (A) Phase-locking of PS neuron relative to external input. Arrows indicate phase-locked states. (B) Phase-locking between PS neurons in a chain length of two segments. Arrows indicate phase-locked states. (C) Phase-locking between PS neurons in a chain of length three segments, shown on the phase-plane. Each segment is modeling using the phase model from chapter 4. $\beta = 0.25$, $\alpha = 2$ and duty cycle is $0.5T^*$.

where

$$(6.3) \quad I(\phi_i) = \begin{cases} 0.2, & \text{for } 0 \leq \phi_i < \text{dc} \cdot T^* \\ 0, & \text{for } \text{dc} \cdot T^* \leq \phi_i < T^*. \end{cases}$$

The coefficient $w_{j,i}$ represents the relative strength of the connection from segment j to segment i , and $d_{j,i}$ represents the phase shift present in descending projections. The values for $w_{j,i}$ and $d_{j,i}$ are shown in (6.4) and (6.5), respectively.

$$(6.4) \quad [w_{j,i}] = \begin{pmatrix} 0 & .8 & .4 & .1 \\ 1 & 0 & .8 & .4 \\ .5 & 1 & 0 & .8 \\ .2 & .5 & 1 & 0 \end{pmatrix}.$$

$$(6.5) \quad [d_{j,i}] = \begin{pmatrix} 0 & 1 & 1 & 1 \\ 0 & 0 & 1 & 1 \\ 0 & 0 & 0 & 1 \\ 0 & 0 & 0 & 0 \end{pmatrix}.$$

Note that by considering all phases relative to the phase of the most posterior HCO in the chain, we can reduce the system by one variable, e.g.

$$(6.6) \quad \begin{aligned} & \frac{d\phi_2}{dt} - \frac{d\phi_4}{dt} = \frac{d\phi_{2,4}}{dt} \\ & = \frac{1}{T^*} \int_0^{T^*} z(\tilde{t} + \phi_2) \left(0.8I \left(\tilde{t} + \phi_1 + \frac{T^*}{2} \right) + I(\tilde{t} + \phi_3) + 0.5I(\tilde{t} + \phi_4) \right) \\ & \quad - z(\tilde{t} + \phi_4) \left(0.1I \left(\tilde{t} + \phi_1 + \frac{T^*}{2} \right) + 0.4I \left(\tilde{t} + \phi_2 + \frac{T^*}{2} \right) + 0.8I \left(\tilde{t} + \phi_3 + \frac{T^*}{2} \right) \right) d\tilde{t} \end{aligned}$$

Let $s = \tilde{t} + \phi_2$ where $\phi_{1,4} = \phi_1 - \phi_4$, $\phi_{3,4} = \phi_3 - \phi_4$, and $\phi_{2,4} = \phi_2 - \phi_4$. Then $\tilde{t} + \phi_1 = s - \phi_{2,4} + \phi_{1,4}$, $\tilde{t} + \phi_3 = s - \phi_{2,4} + \phi_{3,4}$, and $\tilde{t} + \phi_4 = s - \phi_{2,4}$. Then equation (6.6) becomes

$$\begin{aligned} & \frac{d\phi_{2,4}}{dt} = \frac{1}{T^*} \int_0^{T^*} z(s) \left(0.8I \left(s - \phi_{2,4} + \phi_{1,4} + \frac{T^*}{2} \right) + I(s - \phi_{2,4} + \phi_{3,4}) + 0.5I(s - \phi_{2,4}) \right) \\ & - z(s - \phi_{2,4}) \left(0.1I \left(s - \phi_{2,4} + \phi_{1,4} + \frac{T^*}{2} \right) + 0.4I \left(s + \frac{T^*}{2} \right) + 0.8I \left(s - \phi_{2,4} + \phi_{3,4} + \frac{T^*}{2} \right) \right) ds \end{aligned}$$

Figures 6.6, 6.7 and 6.8 use the TWCO to examine the phase-locking dynamics in chain lengths of one through three segments for the phase model HCO and LIF HCO model used earlier. Panels (A) show the interaction function for the PS neuron in one segment. Panels (B) show the interaction function for two segments. The zeros in the curves correspond to phase-locked states. Negative (positive) slopes at the zeros correspond to stability (instability) of the phase-locked state. Panels (C) show phase-plane for chain lengths of 3 segments. The blue (pink) curve is the nullcline to the following equation, which describes the phase difference between segments two and four (three and four).

The intersection point(s) of the pink and blue nullclines are the fixed points, or phase-locked states for the chain of 3 HCOs. The gradient of the direction field shows the basic stability for each fixed point. Phase-locking in a chain length of 4 segments requires a 3-D figure,

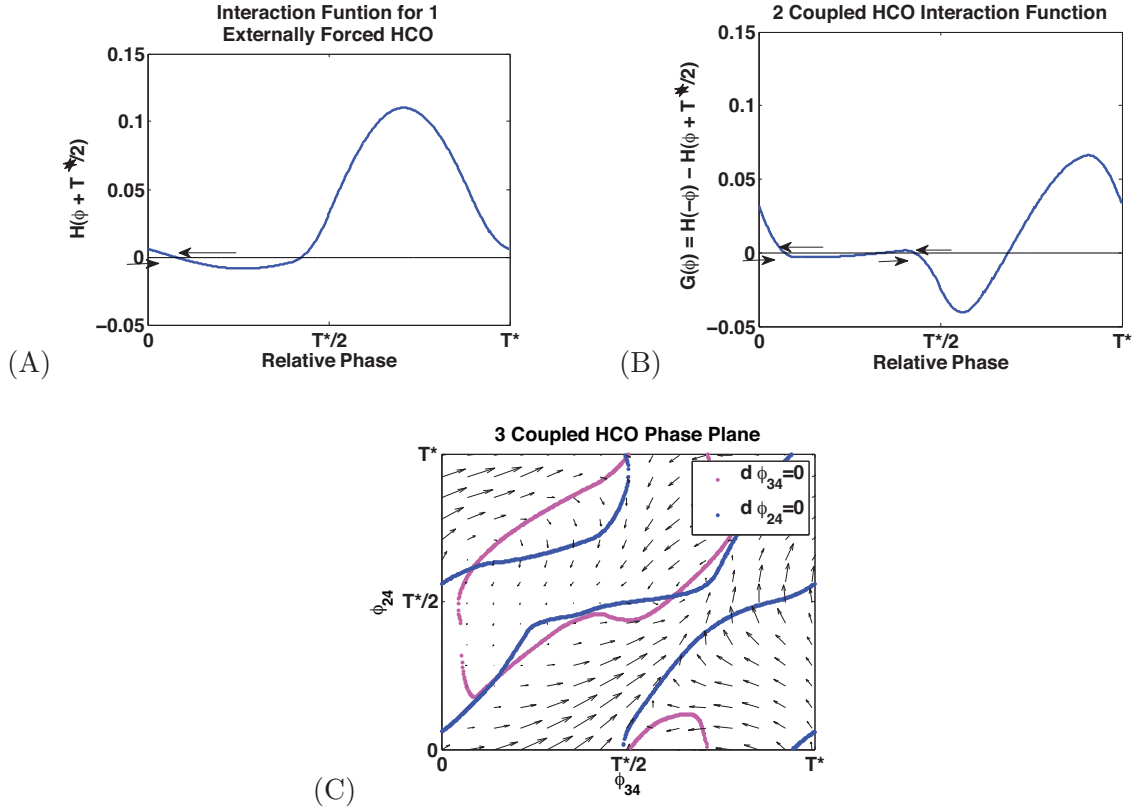


FIGURE 6.7. Phase differences using the TWCO for chain lengths of one through three segments. (A) Phase-locking of PS neuron relative to external input. Arrows indicate phase-locked states. (B) Phase-locking between PS neurons in a chain length of two segments. Arrows indicate phase-locked states. (C) Phase-locking between PS neurons in a chain of length three segments, shown on the phase-plane. Each segment is modeling using the phase model from chapter 4. $\beta = 0.25$, $\alpha = 2$ and duty cycle is $0.9T^*$.

which would be difficult to visualize. Figures 6.6 and 6.7 use the phase model HCO from chapter 4 and figure 6.8 uses the LIF HCO model from chapter 5.

Figure 6.6 uses the same parameters as figure 6.2 with $\beta = 0.25$, $\alpha = 2$ and a duty cycle of $0.5T^*$. The interaction function in figure 6.6A shows that the PS neuron is phase-locked with the external input with a phase lag of slightly less than 100%. This is in agreement with simulations of the full model (figure 6.2A). The interaction function in figure 6.6B shows that in a chain of 2 HCOs, the segments are phase-locked with a phase lag of approximately 25%. This is predicted by the numerical simulations in figure 6.2B. In the phase plane in figure 6.6C, the gradient of the direction field shows that the only stable phase-locked state is near $(\phi_{34}, \phi_{24}) = (T^*/2, 0)$. This corresponds to synchrony between segments 2 and 4, and a 50% phase difference between segments 3 and 4. This is not what is seen in figure

6.2C, where the phase difference between segments 3 and 4 is 25% and the phase difference between segments 2 and 4 is near 50%.

Figure 6.7 uses the same parameters as figure 6.3 with $\beta = 0.25$, $\alpha = 2$ and a duty cycle of $0.9T^*$. The interaction function in figure 6.7A shows that the PS neuron is phase-locked with the external input with a phase lag of approximately 10%. This does not agree with simulations of the full model (figure 6.3A) where the PS neuron is phase-locked with the external input with a phase lag of 50%. The interaction function in figure 6.7B shows the existence of two possible phase-locked states in a chain of 2 HCOs. The segments can be phase-locked with a phase delay of approximately 10% or 50%. This is not predicted by the numerical simulations in figure 6.3B, where the phase lag between segments is slightly greater than 75%. In the phase plane in figure 6.7C, the gradient of the direction field shows that there is no stable fixed point, which is predicted by the numerical simulations in figure 6.3C.

Figure 6.8 uses the same parameters as figure 6.4 with $I = 1.1$, $\alpha = 0.1$ and a duty cycle of $0.5T^*$. The interaction function in figure 6.8A shows that the PS neuron does not phase-lock with the external input. This is in agreement with simulations of the full model (figure 6.4A). The interaction function in figure 6.8B shows that in a chain of 2 HCOs, the segments are phase-locked with a phase delay of approximately 30%. This is not predicted by the numerical simulations in figure 6.4B, where the phase lag between segments is approximately 75%. In the phase plane in figure 6.8C, it appears there is a stable phase-locked state is near $(V_{34}, V_{24}) = (T^*/2, T^*/8)$. This corresponds to a phase difference of 50% between segments 3 and 4, and a phase difference of approximately 12% between segments 2 and 4. This is not predicted by numerical simulations in figure 6.4C, where there is no phase-locked state.

The TWCO was not able to provide any additional insight into the mechanisms underlying phase-locking in a chain of HCOs. Perhaps the coupling was out of the sufficiently weak regime. Regardless, the benefit of using the TWCO is the structure of the equations. Looking at equation 6.3, it is unclear how the PRC combines with the coupling to give phase-locking. This is largely a result of the asymmetries in the coupling mentioned in section 6.1.

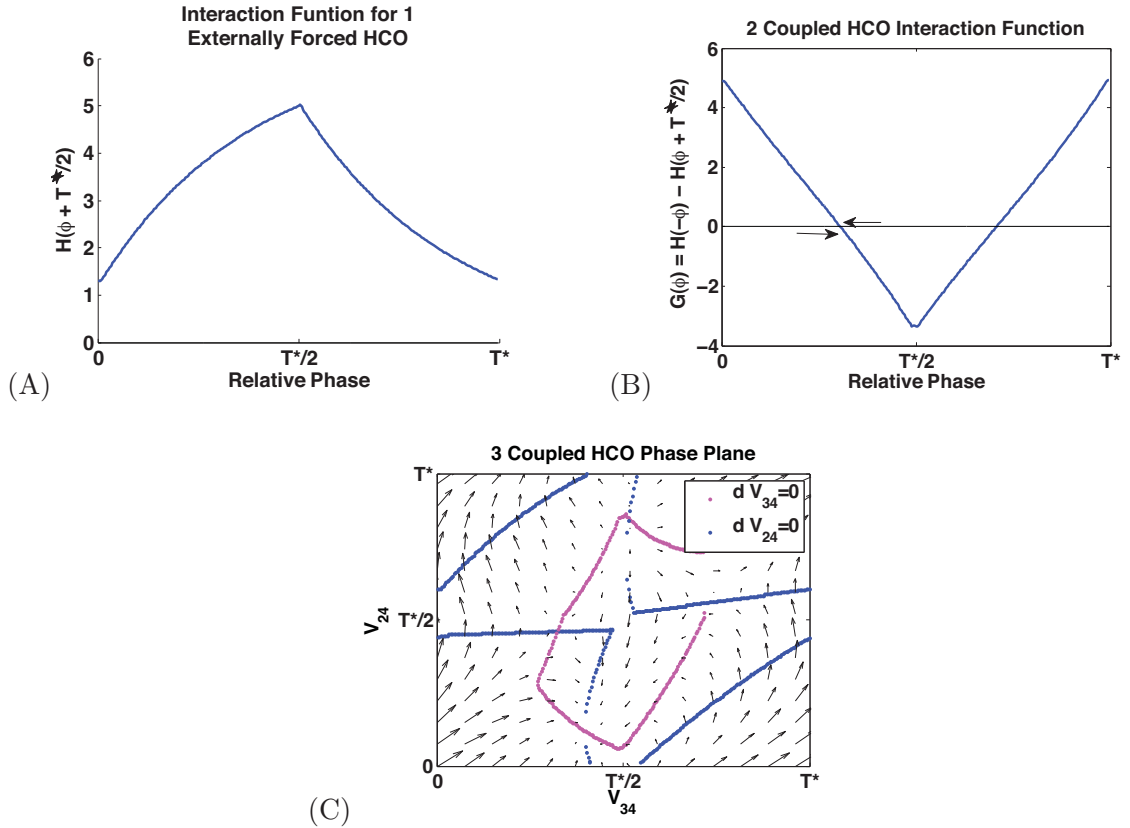


FIGURE 6.8. Phase differences using the TWCO for chain lengths of one through three segments. (A) Phase-locking of PS neuron relative to external input. (B) Phase-locking between PS neurons in a chain length of two segments. Arrows indicate phase-locked states. (C) Phase-locking between PS neurons in a chain of length three segments, shown on the phase-plane. Each segment is modeling using the LIF model from chapter 5. $\alpha = 0.1$, $I = 1.1$ and duty cycle is $0.5T^*$.

6.4. Summary

- In chains of HCOs with cells described by one-variable phase models with sinusoidal PRCs, phase-locking depends strongly on the duty cycle of input to each HCO. A duty cycle of $0.5T^*$ appears to give the best phase-locking of all parameter sets. If the duty cycle is larger, the input from coupling connections is almost constant. If the duty cycle is smaller, the input provides very little phase information. Perhaps a duty cycle of $0.5T^*$ gives the best phase-locking because it provides the most phase information to and from other oscillators.
- When the dynamics of the cells within the HCO are described by leaky integrate-and-fire neurons, even a duty cycle of $0.5T^*$ did not guarantee phase-locking in all chain lengths simultaneously. This implies that the LIF model is probably not a useful model for studying phase-locking behavior in the crayfish. One possible

reason is that the LIF model has a non-periodic, positive PRC. Perhaps reliable phase-locking requires a biphasic PRC.

- It is clear that stable phase-locking in a chain of a certain length does not predict stable phase-locking in a chain of a different length. This implies that the mechanisms underlying phase-locking in a chain of two segments in the crayfish may act in different ways to generate phase-locking in the full system of four segments.
- Results from numerical simulations do not always match results from the TWCO. The discrepancies may be due to the intersegmental coupling strength. However, the TWCO is usually a good approximation for non-weak coupling unless the system is sensitive, i.e. it takes a few cycles for the system to return to steady state after a brief pulse. More work must be done to see if there are these types of sensitivities in the system.
- The TWCO separates changes in intersegmental coupling from changes in HCO intrinsic properties. More work may be done to study phase-locking with different, more realistic, connectivity schemes and HCO PRCs.
- The desired phase lag of 25% existed for one parameter set only (sinusoidal PRCs with $\beta = 0.25$, $\alpha = 2$ and duty cycle of $0.5T^*$). More work must be done to determine how to achieve phase-locking in all chain lengths, how to maintain a phase lag of 25% between segments, and how to take results from shorter chains to make predictions about behavior in longer chains.
- Perhaps phase-locking in the crayfish swimmeret system stems from a sinusoidal HCO PRC with an intersegmental connectivity duty cycle of $0.5T^*$ between segments.

CHAPTER 7

Addendum: Analysis of HCO phase models

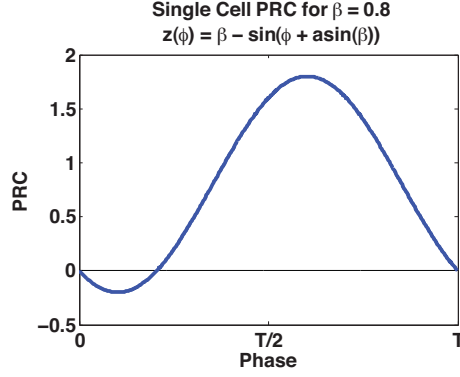
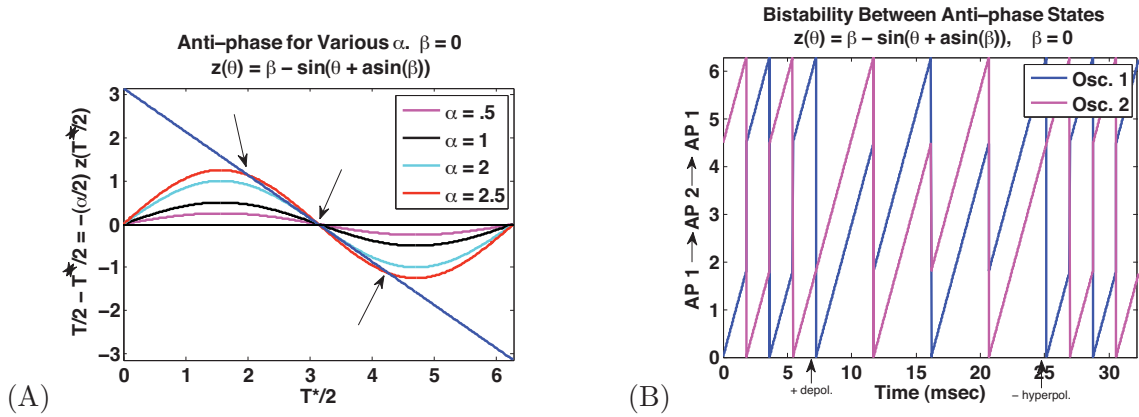
When studying phase models, the “instantaneous” Dirac-delta function is often used as an approximation to continuous synaptic currents with fast decay [KE09] [GE02]. In this chapter, we show that, for coupled phase models, this approximation does not match the limit of current-based synapses to the δ -function except in the weak coupling limit. We show why this is the case and determine a “corrected” δ -function coupling for phase models that provides the correct limit.

7.1. HCO phase model with standard δ -function synapses

Consider the half-center oscillator (HCO) model introduced first in chapter 4. The dynamics of each cell within the HCO are described with a single equation describing the evolution of the phase of the cell during oscillations and its response to input. The state of each cell is completely described by its phase in the oscillation ϕ ($\phi \in [0, T]$), where T is the intrinsic period of the cell. The response to input is given in a phase dependent manner by its PRC, $z(\phi)$. The cells are coupled by “standard” δ -function synapses. When a cell reaches phase $\phi = T$ (equivalent to $\phi = 0$), it “fires” and elicits an instantaneous synaptic current in the postsynaptic cell. The equations governing the HCO phase model are

$$(7.1) \quad \begin{aligned} \frac{d\phi_1}{dt} &= 1 - \alpha \delta(\phi_2) z(\phi_1(t)), & \text{if } \phi_1 = T, \phi_1 \rightarrow 0 \\ \frac{d\phi_2}{dt} &= 1 - \alpha \delta(\phi_1) z(\phi_2(t)), & \text{if } \phi_2 = T, \phi_2 \rightarrow 0 \end{aligned}$$

where ϕ_i is the phase of cell i . The term $\alpha\delta(\phi_i)$ is the synaptic current, where α is the synaptic strength and $\delta(\phi_i)$ is the Dirac-delta function. In this chapter, we consider only inhibitory synapses ($\alpha > 0$). Each cell is assumed to have an identical PRC $z(\phi_i)$ and identical period T . In this chapter, we use $z(\theta) = \beta - \sin(\theta + \arcsin(\beta))$. Figure 7.1 shows the single cell PRC for $\beta = 0.8$.

FIGURE 7.1. Single cell PRC for $\beta = 0.8$. $T = 2\phi$.FIGURE 7.2. (A) The value of $T^*/2$ is shown for various α and β values. Notice that for a certain range of α , there exists two physical anti-phase solutions for $\beta = 0$. (B) Bistability between the two anti-phase solutions for $\beta = 0$, $\alpha = 3$.

We define T^* as the period of the steady-state anti-phase oscillation of the HCO. During steady state anti-phase oscillations, each inhibitory synaptic pulse arrives at phase $\phi_i = T^*/2$. T^* is a combination of the intrinsic period and the phase shift due to the coupling,

$$(7.2) \quad T^* = T + \alpha z(T^*/2).$$

See chapter 4 for details. Figure 7.2A shows the number of possible anti-phase states of the HCO for various α . They are found by rearranging equation (7.2).

$$(7.3) \quad T/2 - T^*/2 = -\alpha/2 z(T^*/2).$$

Figure 7.2 shows a special case, when $\beta = 0$. In figure 7.2A, the blue line is $T/2 - T^*/2$. The sinusoidal curves are $-(\alpha/2)z(T^*/2)$ for various α , i.e. scaled PRCs. The intersection point of the scaled PRCs with the blue diagonal line correspond to the anti-phase states of the

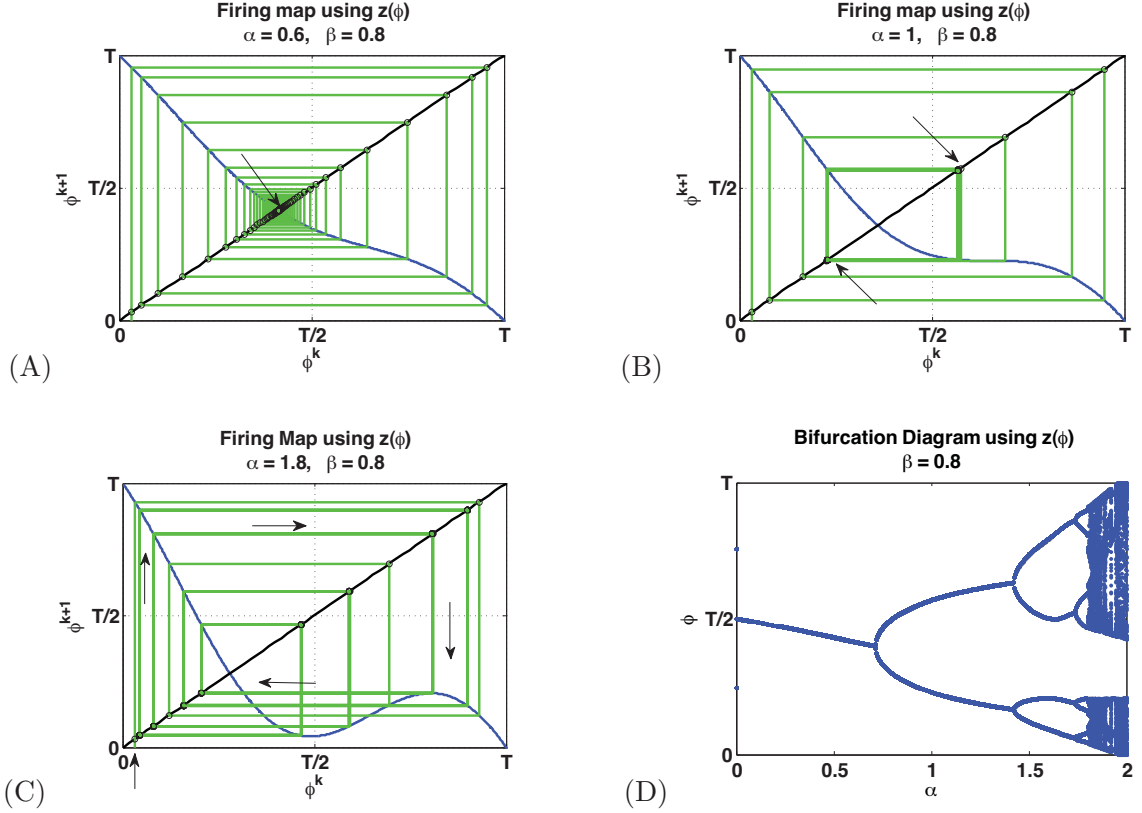


FIGURE 7.3. Cobweb diagram for the firing map in equation (7.4) when $\beta = 0.8$ and (A) $\alpha = 0.5$, (B) $\alpha = 1$, and (C) $\alpha = 1.8$. (D) Bifurcation diagram showing the number of fixed points and cycles of the system (7.1) as α increases.

system. When inhibitory coupling is sufficiently weak, the sole anti-phase state $T^*/2 = \pi$ is stable. As α increases, the number of anti-phase states increases from 1 to 3. That is, near $\alpha = 2.5$, $T^*/2 = \pi$ becomes unstable and the two new stable anti-phase states appear through a supercritical pitchfork bifurcation. Figure 7.2B shows an example of the bistability in the anti-phase solution for $\beta = 0$, $\alpha = 3$. Beginning in one anti-phase state, a precisely timed depolarizing perturbation causes the system to switch to the other stable anti-phase state. When a precisely timed hyperpolarizing perturbation is given, the system transitions back to the first anti-phase state.

Following the same logic as in section 4.2, we define the firing map for the HCO phase model with δ -function synapses (system (7.1)). This map completely captures the unperturbed firing dynamics of the HCO system.

$$(7.4) \quad \phi^{k+1} = (T - \phi^k) - \alpha z(T - \phi^k).$$

Note that fixed points of this map correspond to anti-phase oscillations in the HCO.

Figure 7.3A-C shows cobweb diagrams for the firing map when $\beta = 0.8$. In figure 7.3A, $\alpha = 0.6$ and the map has one stable fixed point. In figure 7.3B, $\alpha = 1$ and the map has a period-2 orbit. In figure 7.3C, $\alpha = 1.8$ and the map displays chaotic behavior, never converging to one fixed point or periodic orbit. The bifurcation diagram of the map in figure 7.3D shows the fixed points and cycles of the system (7.1) as α increases ($\beta = 0.8$). For $\alpha < .7$ there is one fixed point, which corresponds to a stable anti-phase state. Near $\alpha = .7$, there is a period doubling bifurcation, after which there is a period-2 orbit corresponding to an asynchronous periodic state. The period doubling cascade [OM09] [Str94] continues as α increases, eventually leading to chaos near $\alpha = 1.8$.

7.2. HCO phase model with exponential synapses

As previously mentioned, δ -function synapses are often used in phase models as an approximation to continuous synaptic currents with fast decay. If, instead of the δ -function, we use exponential synapses in the HCO phase model, the governing equations become

$$(7.5) \quad \begin{aligned} \frac{d\phi_1}{dt} &= 1 - \alpha s_2(t) z(\phi_1(t)) && \text{if } \phi_1 = T, \phi_1 \rightarrow 0 \\ \frac{d\phi_2}{dt} &= 1 - \alpha s_1(t) z(\phi_2(t)) && \text{if } \phi_2 = T, \phi_2 \rightarrow 0 \\ \frac{ds_1}{dt} &= \frac{-s_1}{\tau} && \text{if } \phi_1 = 0, s_1 = s_1 + (1/\tau) \\ \frac{ds_2}{dt} &= \frac{-s_2}{\tau} && \text{if } \phi_2 = 0, s_2 = s_2 + (1/\tau) \end{aligned}$$

where α is the synaptic strength and $s_i(t)$ describes the synaptic waveform. The parameter τ describes the rate of decay of the synaptic current.

When $\tau = 0.001$, the synaptic waveform approximates the δ -function on the timescale $O(T)$. The bifurcation diagram in figure 7.4 shows the number of stable anti-phase states for system (7.5) with exponential synapses when $\tau = 0.001$. If the δ -function were indeed a good approximation to synaptic currents with very fast decay, then figure 7.4 should be very similar to figure 7.3D. Clearly, there are striking qualitative differences: there is only

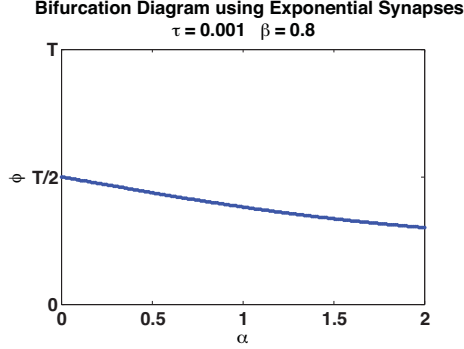


FIGURE 7.4. Bifurcation diagram showing the number of stable anti-phase states for system (7.5) as α increases. $\tau = .001$

one stable anti-phase state for system (7.5) when $\tau = 0.001$ despite changes in α , and there is no period-doubling bifurcation into chaos.

Figure 7.5 illustrates the mechanisms underlying the differences between the system's dynamics with δ -function synapses and continuous synapses (in this case exponential synapses). Suppose that the cells in the HCO are coupled with δ -function synapses (figure 7.5A) and an inhibitory perturbation into one cell arrives at phase ϕ_A . The cell responds according to the PRC and jumps to phase $\phi_B = \phi_A - \alpha z(\phi_A)$, i.e. only the phase at which the perturbation was received is taken into account. Now consider that the cells in the HCO are coupled with continuous synapses (figure 7.5B). To demonstrate the cell's response to input, we approximate the continuous synaptic current by discretizing time with small Δt . If the inhibitory perturbation into one cell arrives at phase ϕ_A , the cell responds according to the PRC and jumps to phase $\phi_A - \alpha \Delta t z(\phi_A)$. The cell continues to respond according to the PRC and makes small jumps approaching phase ϕ_B , where $z(\phi_B) = 0$. Once the cell reaches phase ϕ_B , it can not move on because a perturbed cell cannot move past a zero in the single cell PRC. Here, each phase between ϕ_A and ϕ_B is taken into account. Simply replacing the synaptic conductance ($s(t)$) with a δ -function in system (7.1), creates a discontinuity in time where the phase response of the cell at any phase other than the phase where it receives the inhibitory pulse are ignored. Continuous synaptic currents do not do this. This implies that the standard δ -function is the incorrect limit to synaptic currents with very fast decay.

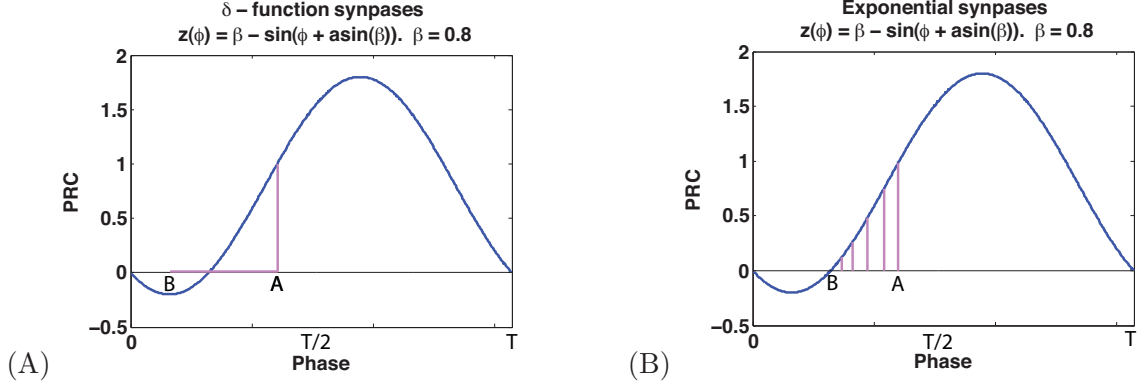


FIGURE 7.5. Differences in how the cells in the HCO respond when coupled with δ -function synapses (A) or exponential synapses (B). $\alpha = 1$.

7.3. The correct limit to synaptic currents with fast decay

In order to determine the correct limit to synaptic currents with fast decay, we systematically reduce system (7.5) by approximating the synaptic coupling term $\alpha s(t)z(\phi(t))$ with a new function in the case where the time constant for synaptic decay is very small, i.e. the synapses are very fast ($\tau \ll T$). When $\tau \ll T$, $s_j(t) = \frac{1}{\tau}e^{-t/\tau} \gg 1$ ($j = 1, 2$) on the short time scale (when $t \ll \tau$). This is a reasonable approximation because $\tau \ll T$ indicates that the synapses decay very fast, and there is little-to-no synaptic conductance remaining at larger values of t . If α and $z(\phi)$ are such that $\alpha s(t)z(\phi(t)) \gg 1$ when $t \ll \tau$, we can approximate $\frac{d\phi_i}{dt}$ by

$$(7.6) \quad \frac{d\phi_i}{dt} \approx -\alpha s(t)z(\phi_i(t)) = -\frac{\alpha}{\tau}e^{-t/\tau}z(\phi_i(t)).$$

Let ϕ_i^0 be the phase of cell i when a synaptic current is delivered to it, and let $\phi_i + \Delta\phi$ be the phase of cell i when the synaptic current is approximately zero. Integrating the differential equation in (7.6),

$$(7.7) \quad \int_{\phi_i^0}^{\phi_i^0 + \Delta\phi} \frac{d\phi}{z(\phi)} \approx -\frac{\alpha}{\tau} \int_0^\infty e^{-t/\tau} dt.$$

We can integrate to infinity on the right-hand side because we are considering very fast decay, so the exponential decays to zero almost immediately. The right-hand side integrates to $-\alpha$,

$$(7.8) \quad \int_{\phi_i^0}^{\phi_i^0 + \Delta\phi} \frac{d\phi}{z(\phi)} \approx -\alpha.$$

Let $Z(\phi)$ be the antiderivative of $\frac{1}{z(\phi)}$, then

$$(7.9) \quad Z(\phi_i^0 + \Delta\phi) - Z(\phi_i^0) \approx -\alpha.$$

We solve the nonlinear algebraic equation (7.9) for the phase response of the single cell with the synapse, $\Delta\phi(\phi_i^0)$. Note that $\Delta\phi(\phi)$ describes a phase response curve for the synaptic input, i.e. the phase shift caused by a current of strength α delivered at a particular phase ϕ . It takes into account the phase response at all phases between where the perturbation was initiated and “terminated”. This ensures that the cell cannot move past a zero in the single cell PRC. We call $\Delta\phi(\phi)$ the synaptic phase response curve.

The above argument reduces system (7.1) to an alternate δ -pulse-coupled HCO phase model

$$(7.10) \quad \begin{aligned} \frac{d\phi_1}{dt} &= 1 + \delta(\phi_2)\Delta\phi(\phi_1) \\ \frac{d\phi_2}{dt} &= 1 + \delta(\phi_1)\Delta\phi(\phi_2). \end{aligned}$$

The basic dynamics of this system are qualitatively the same as system (7.1). The phase of each cell increases linearly according to its intrinsic dynamics $\frac{d\phi_i}{dt} = 1$ until the phase of a cell i reaches T . At phase T , cell i is reset to 0 and an instantaneous pulse of strength α is delivered to cell j . The phase of cell j is immediately shifted by $\Delta\phi(\phi_j)$, instead of simply $-\alpha z(\phi_j)$ as in system (7.1).

As before, we define the firing map for the alternate HCO phase model (system (7.10)).

$$(7.11) \quad \phi^{k+1} = (T - \phi^k) + \Delta\phi(T - \phi^k).$$

Figure 7.6A shows a cobweb diagram for this firing map when $\alpha = 1.8$, $\beta = 0.8$. The map converges to a unique fixed point, whereas the map for the standard δ -function displayed chaotic behavior (figure 7.3A). The bifurcation diagram in figure 7.6B shows the fixed points and cycles for system (7.1) as α increases ($\beta = 0.8$). For all α , there is only one stable anti-phase state. This diagram is indistinguishable from the bifurcation diagram for exponential synapses when $\tau = .001$ (figure 7.4), indicating that the alternate δ -function is the correct limit to synaptic currents with very fast decay.

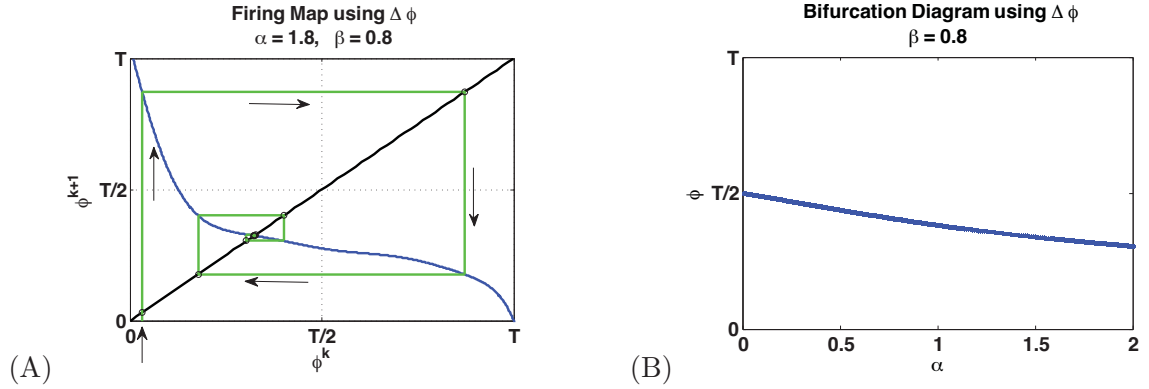


FIGURE 7.6. (A) Cobweb diagram for the firing map in equation (7.11) when $\alpha = 1.8$ and $\beta = 0.8$. (B) Bifurcation diagram showing the number of stable anti-phase states for system (7.10) as α increases.

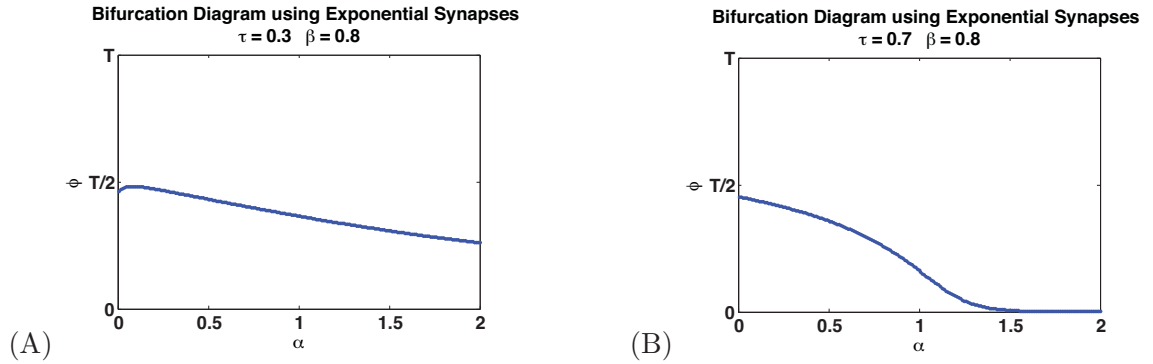


FIGURE 7.7. Bifurcation diagram showing the number of stable anti-phase states for system (7.5) as α increases. (A) $\tau = .3$ (B) $\tau = .7$

The bifurcation diagrams in figure 7.7 show the fixed points and cycles for system (7.5) with more slowly decaying synapses. In figure 7.7A, $\tau = 0.3$ and in figure 7.7B, $\tau = 0.7$ (both are non-summing synapses). As τ increases, the bifurcation diagrams deviate from figures 7.6B and 7.4, but the qualitative dynamics are captured and the number of anti-phase states remains at 1. There is no period doubling cascade to chaos because the synaptic PRC $\Delta\phi$ cannot cross a zero of $z(\phi)$, which means we cannot get a non-monotonic map as in figure 7.3. Note that when $\tau = 0.7$ and $\alpha \approx 1.5$, the system transitions from anti-phase behavior to synchrony. The transition to synchrony is probably a bifurcation and not a smooth transition, but we did not run the simulation long enough to see this.

7.4. Summary

When the standard δ -function is used in networks of phase models as an approximation to synapses with very fast decay, the results from the approximation can differ significantly from the original model (as in figures 7.3D and 7.4). Therefore, when approximating synapses with very fast decay in phase models, the alternate δ -function found in section 7.3 should be used instead of the standard δ -function. Note that the reduction explicitly uses exponential synapses, but it is identical for any synaptic current that is delivered sufficiently fast. That is, the reduction does not depend on the shape of the input, it only depends on the total charge and the assumption that the input decays very fast.

CHAPTER 8

Crayfish Conclusion

The crayfish swimmeret system can serve as a useful tool to investigate the cellular mechanisms that underlie phase maintenance over a range of locomotor frequencies from both an experimental and modeling approach. Working in collaboration with the Mulloney lab, we have been able to construct and analyze mathematical models of the crayfish neural circuitry, and in doing so, we have begun to uncover the mechanisms underlying phase maintenance during locomotion.

8.1. Summary

The goal of this work is to begin to identify the biophysical mechanisms and dynamical structures underlying phase-locking in the crayfish swimmeret system. The theory of weakly coupled oscillators (TWCO) is a useful tool because it allows us to study phase-locking in two steps. The TWCO combines information about the phase response curve (PRC) of the individual oscillators with information about the coupling between oscillators to determine the phase-locking in the system. Therefore, we study the intrinsic properties of the oscillators (chapters 3 - 5) separately from the connectivity and synaptic dynamics between oscillators (chapter 6) to develop a greater understanding of phase-locking in the crayfish swimmeret system.

Chapters 3 - 5 explored how the phase response properties of HCOs are determined from the intrinsic cellular properties and synaptic properties within the HCO. In chapter 3, a numerical study using a modified Morris-Lecar HCO model demonstrated the difficulty in understanding how changes in parameters can lead to changes in the HCO PRC. Chapter 4 examined an analytically tractable phase model and chapter 5 examined the leaky integrate-and-fire model. In both chapters, the PRC of the HCO is found to be a product of the single cell PRC and a piecewise constant attenuating factor. In the case of the phase model, the attenuating factor depends on slope of the synaptic PRC at anti-phase, which is derived

from the single cell PRC (see chapter 4). In the case of the leaky integrate-and-fire model, the attenuating factor depends on the applied current, which scales the single cell PRC, and synaptic strength. These results imply that the PRC of a more realistic conductance-based HCO is related to the single cell PRCs by a constant attenuating factor. In fact, one approximation to the PRC of a physiological HCO is simply the PRC of a single cell within the HCO.

Chapter 6 is a preliminary study of phase-locking in a chain of HCOs. Using the phase model from chapter 4, we found that phase-locking depends strongly on the duty cycle of input to each HCO and that there is no predictable behavior between chains lengths. In other words, phase-locking in a chain of three segments does not imply that a chain of two or four segments will also exhibit phase-locking. This implies that the mechanisms underlying phase-locking in the crayfish swimmeret system for chain of two segments are not necessarily the same mechanisms underlying phase-locking in the full swimmeret system of four segments. Furthermore, using the leaky integrate-and-fire model from chapter 5, we found no parameter set that allowed phase-locking in all four chain lengths simultaneously. Therefore, the LIF model is not a useful model for studying phase-locking behavior in the crayfish.

8.2. Future Modeling and Experimental Work

This work is a starting point towards a greater understanding of the mechanisms underlying coordinated limb movement during locomotion in the crayfish swimmeret system. We use idealized models of HCOs where the cells are described by either Morris-Lecar neurons, LIF neurons or one-variable phase models. Coupling between the cells is either δ -function pulse coupling or current-based exponential synapses with very fast decay. The intersegmental circuitry is modeled as a square-pulse with a direct synapse from presynaptic to postsynaptic cell.

Future modeling efforts can expand this work by studying conductance-based models with biophysical details related to the crayfish swimmeret system. Experimentally, PRCs can be generated from the oscillatory system of non-spiking local interneurons. This data will allow modelers to either modify the Morris-Lecar type equations by adding relevant currents, or

replace them with a more appropriate model. The coupling between the cells can also be expanded to more realistic, conductance-based synapses. Then phase-locking between segments can be studied using numerical simulations and the TWCO.

Models can also focus on the implications of including ComInt 1 in a model of the intersegmental circuitry. Recent experiments have shown that ComInt 1 receives monosynaptic connections from coordinating neurons in other modules (see figure 2.2). ComInt 1 neurons then integrate and transmit this information to their home module through graded potentials. This novel circuitry has not been studied in the context of phase-locking of coupled oscillators and may have non-intuitive consequences. By developing and analyzing a mathematical model of this intersegmental circuit, one can clarify how ComInt 1 is connected to its home module and as a result gain insight into how this circuitry assists in maintaining a constant intersegmental phase despite changes in frequency.

Finally, one may model the asymmetric coupling between modules via ascending and descending coordinating neurons. Smarandache and Mulloney recently found that the ascending and descending intersegmental coordinating neurons synapse onto ComInt 1 with different synaptic strengths, but it is still unknown what effect this has on the response of the non-spiking local interneurons. One can use a network model to generate PRCs as a way to test the effects of varying synaptic current strengths and timing of inputs from ascending and descending coordinating neurons to compare with experimentally generated PRCs.

APPENDIX A

A.1. Morris Lecar Model

A.1.1. Morris Lecar Model used for Crayfish Modeling. The modified Morris-Lecar network model of the crayfish CPG presented in Jones et al. [JMKK03]. In the original model of Jones et al., there were three local interneurons forming the CPG: 1A, 1B, and 2. Here, we use only two local interneurons 1 and 2 when modeling the HCO. The model parameters are identical for each of the two cells. All parameters are taken to be the same as in Jones et al. except the local synaptic conductance, which is taken to be 0.1 mS/cm² rather than 0.5 mS/cm². This change is made to counter the effect of going from a three-cell interneuron circuit to a two-cell circuit.

$$(A.1) \quad C \frac{dV_i}{dt} = I_{app} - (I_L + I_{Ca} + I_K + I_{syn})$$

$$(A.2) \quad \frac{dn_i}{dt} = \epsilon_1 \lambda_n(V_i)(n_\infty(V_i) - n_i)$$

$$(A.3) \quad \frac{ds_j}{dt} = \frac{\epsilon_2}{k} \cdot \frac{s_\infty(V_j) - s_j}{1 - s_\infty(V_j)}$$

$$(A.4) \quad I_L = g_L(V_i - E_L)$$

$$(A.5) \quad I_{Ca} = g_{Ca} m_\infty(V_i)(V_i - E_{Ca})$$

$$(A.6) \quad I_K = g_K n_i(V_i - E_K)$$

$$(A.7) \quad I_{syn} = g_{syn} s_j(V_i - E_{syn})$$

$$(A.8) \quad \lambda(V_i) = \cosh\left(\frac{V_i - A_3}{2A_4}\right)$$

$$(A.9) \quad n_\infty(V_i) = \frac{1}{2}\left(1 + \tanh\left(\frac{V_i - A_3}{A_4}\right)\right)$$

$$(A.10) \quad m_\infty(V_i) = \frac{1}{2}\left(1 + \tanh\left(\frac{V_i - A_1}{A_2}\right)\right)$$

$$(A.11) \quad s_\infty(V_j) = \tanh\left(\frac{V_j - V_{TH}}{V_{slope}}\right) \quad \text{if } V_j > V_{TH} \quad \text{else } 0$$

Model Parameters:

$$\begin{array}{llll}
 g_L = 0.2 \text{ mS/cm}^2 & E_L = -60 \text{ mV} & A_1 = -25 \text{ mV} & A_2 = -20 \text{ mV} \\
 g_{Ca} = 0.3 \text{ mS/cm}^2 & E_{Ca} = 100 \text{ mV} & A_3 = -30 \text{ mV} & A_4 = 15 \text{ mV} \\
 g_K = 0.3 \text{ mS/cm}^2 & E_K = -80 \text{ mV} & V_{TH} = -50 \text{ mV} & V_{slope} = 10 \text{ mV} \\
 g_{syn} = 0.1 \text{ mS/cm}^2 & E_{syn} = -60 \text{ mV} & C = 1 \text{ } \mu\text{F/cm}^2 & I_{ext} = 1 \text{ } \mu\text{A/cm}^2 \\
 \epsilon_1 = 0.006 & \epsilon_2 = 0.006 & k = 3 &
 \end{array}$$

Definition of Model Parameters and Variables:

I_{app} = external applied current ($\mu\text{A/cm}^2$)

I_L = leak current ($\mu\text{A/cm}^2$)

I_{Ca} = calcium current ($\mu\text{A/cm}^2$)

I_K = potassium current ($\mu\text{A/cm}^2$)

I_{syn} = synaptic current ($\mu\text{A/cm}^2$)

$g_L, g_{Ca}, g_K, g_{syn}$ = maximal conductance for leak, calcium, potassium, and synaptic currents (mS/cm^2)

$E_L, E_{Ca}, E_K, E_{syn}$ = reversal potentials for leak, calcium, potassium, and synaptic currents (mV)

V_i = membrane potential of cell i (mV)

C = membrane capacitance ($\mu\text{F/cm}^2$)

t = time (msec)

$\epsilon_i \lambda_n(V_i)$ = rate constant of potassium channel opening

ϵ_1 = small parameter that represents the minimum of λ_n

A_1, A_3 = voltages at which one-half of the channels are open at steady state

A_2, A_4 = voltages with reciprocals that are the slopes of the voltage dependence of calcium and potassium channel opening at steady state

$n_\infty(V_i), m_\infty(V_i)$ = fractions of open potassium and calcium channels at steady state

n = fraction of potassium channels that are actually open

s_j = synaptic gating variable controlling the synapse from cell j to cell i

$\epsilon_2/k(1 - s_\infty)$ = rate constant of s_i

$s_\infty(V_j)$ = steady-state synaptic activation value of the postsynaptic cell i as a function of the voltage of the presynaptic cell j

A.2. Linearization of Firing Map

The firing map of the HCO phase model in chapter 4 is

$$(A.12) \quad \phi^{k+1} = T - \phi^k + \Delta\phi(T - \phi^k) = h(\phi^k).$$

We linearize the firing map around the fixed point ϕ^* . Let $\phi^k = \phi^* + \epsilon\tilde{\phi}^k$. $\epsilon\tilde{\phi}^k$ is a small perturbation away from the steady state ϕ^* ($\epsilon \ll 1$). Substituting this into the firing map (equation (A.12)) gives

$$(A.13) \quad \phi^* + \epsilon\tilde{\phi}^{k+1} = h(\phi^* + \epsilon\tilde{\phi}^k).$$

We linearize about $\epsilon = 0$.

$$(A.14) \quad \phi^* + \epsilon\tilde{\phi}^{k+1} = h(\phi^*) + \epsilon\tilde{\phi}^k h'(\phi^*) + O(\epsilon^2)$$

$$(A.15) \quad \epsilon\tilde{\phi}^{k+1} = \epsilon\tilde{\phi}^k h'(\phi^*) + O(\epsilon^2).$$

The coefficients in the ϵ^2 term cannot be ignored if they are on the order of $O(1/\epsilon)$ or greater. The $O(\epsilon^2)$ term is

$$(A.16) \quad \frac{1}{2}[\tilde{\phi}^k]^2 h''(\phi^*) \epsilon^2$$

where

$$(A.17) \quad \tilde{\phi}^k \approx \tilde{\phi}^0 = \pm z(\phi_1)[1 + \Delta\phi'(T^*/2)]$$

where $|1 + \Delta\phi'(T^*/2)| < 1$ is a requirement for anti-phase oscillations. Here, ϕ_1 is the phase of cell 1 when the perturbation used to determine the PRC of the HCO is given. $z(\phi_1)$ is the PRC of cell 1 evaluated at that phase. Also,

$$(A.18) \quad h''(\phi^*) = \Delta\phi''(T - \phi^*) = \Delta\phi''(T^*/2).$$

So,

$$(A.19) \quad \left| \frac{1}{2}[\tilde{\phi}^k]^2 h''(\phi^*) \right| \approx \left| \frac{1}{2} \Delta\phi''(T^*/2) [z(\phi_1)[1 + \Delta\phi'(T^*/2)]]^2 \right| < \frac{1}{2} |\Delta\phi''(T^*/2)| z^2(\phi_1).$$

We want to ensure that

$$(A.20) \quad \frac{1}{2} |\Delta\phi''(T^*/2)| z^2(\phi_1) \ll 1/\epsilon,$$

so the $O(\epsilon^2)$ term can be ignored. Since $z(\phi_1)$ will vary, we require

$$(A.21) \quad \epsilon \ll 2 / (\alpha |\Delta\phi''(T^*/2)| \max[z^2(\phi_1)]).$$

As long as ϵ is ‘small’ and satisfies the above requirement, we may ignore the $O(\epsilon^2)$ term in our expansion and we are left with:

$$(A.22) \quad \tilde{\phi}^{k+1} = \tilde{\phi}^k h'(\phi^*),$$

which has the solution

$$(A.23) \quad \tilde{\phi}^k = [h'(\phi^*)]^k \tilde{\phi}^0.$$

A.3. iPRC for LIF model

The equation governing the single LIF cell is

$$(A.24) \quad \frac{dV}{dt} = I - V, \quad \text{when } V = 1, V \rightarrow 0.$$

If the cell has initial conditions $V(0) = 0$, the cell evolves according to

$$(A.25) \quad V(t) = I(1 - e^{-t}).$$

When $I > 1$, the cell oscillates intrinsically with single cell period

$$(A.26) \quad T = \ln \left(\frac{I}{I-1} \right).$$

We let ϕ denote the phase of the cell, $\phi \in (0, T)$. To find the iPRC, we give an instantaneous ϵ -sized perturbation ($\epsilon \ll 1$) to the cell at phase ϕ which corresponds to time $t = t_\phi$.

Immediately after the perturbation, the cell is at

$$(A.27) \quad V(t_\phi) = I(1 - e^{-t_\phi}) + \epsilon.$$

We use $V(t_\phi)$ as the initial condition to find the new firing time. After the perturbation the cell advances according to

$$(A.28) \quad V(t) = I(1 - e^{-t}) + \epsilon e^{-(t-t_\phi)}.$$

The cell fires at time $T - \Delta\phi$, when $V(T - \Delta\phi) = 1$.

$$(A.29) \quad V(T - \Delta\phi) = I(1 - e^{-(T-\Delta\phi)}) + \epsilon e^{-(T-\Delta\phi-t_\phi)} = 1.$$

Solving for $T - \Delta\phi$,

$$(A.30) \quad T - \Delta\phi = \ln\left(\frac{I - \epsilon e^{t_\phi}}{I - 1}\right).$$

The phase advance is

$$(A.31) \quad \Delta\phi = T - \ln\left(\frac{I - \epsilon e^{t_\phi}}{I - 1}\right)$$

$$(A.32) \quad \Delta\phi = \ln\left(\frac{I}{I - 1}\right) - \ln\left(\frac{I - \epsilon e^{t_\phi}}{I - 1}\right)$$

$$(A.33) \quad \Delta\phi = \ln\left(\frac{I}{I - \epsilon e^{t_\phi}}\right).$$

To find the iPRC, we expand about $\epsilon = 0$,

$$(A.34) \quad \Delta\phi = \epsilon \frac{e^{t_\phi}}{I} + O(\epsilon^2).$$

Therefore, the iPRC is

$$(A.35) \quad z(\phi) = e^\phi / I, \quad \phi \in (0, T).$$

Part 2

Dynamical and Biophysical Mechanisms of Anesthetic Action

Summary

The goal of Part 2 of this thesis is to build mathematical models to study the effects of volatile anesthetic on neural networks in the spinal cord. The network under consideration is composed of excitatory interneurons in the lamprey central pattern generator (CPG), a spinal cord neuronal network responsible for generating rhythmic locomotor movement in vertebrates such as swimming or walking. It is thought that the excitatory interneurons of the CPGs are the main target of the volatile anesthetic isoflurane, leading to immobility under anesthesia. The following chapters will model these interneurons and incorporate the most relevant effects of the volatile anesthetic isoflurane on intracellular conductances using bifurcation analysis and numerical simulations.

Part 2 is broken down as follows:

1. This work develops a mathematical model for the two-pore potassium conductances TREK and TASK based on experimental data, and incorporates these targets of volatile anesthetics into two existing conductance-based models of single neurons.
2. The Butera et al. model [BRS99a] is modified by adding TREK and TASK currents. The Brodin et al. model [BTL⁺91] is reduced to a minimal form that captures the qualitative results of the original model, then modified by adding TREK, TASK and persistent sodium currents.
3. The Butera et al. model is used as a canonical bursting model and the Brodin et al. model as a detailed biophysical model of a lamprey excitatory interneuron. The most important parameters are explored using numerical simulations to gain insight into each model's capabilities, specifically how bursting dynamics change as parameters are varied.
4. A fast-slow decomposition and bifurcation analysis are performed on the reduced models in order to determine the bursting mechanism of the full models and possible transitions between firing states they may exhibit.
5. This work develops an understanding of the possible dynamical changes occurring in the isolated lamprey spinal cord due to the hypothesized mechanisms of volatile anesthetic action and determines possible experiments to further elucidate these mechanisms.

CHAPTER 9

Physiological Background**9.1. Volatile anesthesia in the lamprey spinal cord**

Anesthesia has been used worldwide for over 150 years, yet the underlying physiological mechanisms of their action remain unclear [SPLIB98] [RA04] [UB02] [McC07] [Ors07]. Effective administration of anesthetics may be vastly improved with greater understanding of how anesthesia acts. Desired anesthetic endpoints include amnesia, analgesia, sedation, unconsciousness, and immobility [RA04]. Anesthetics have been shown to modulate activity of a variety of voltage-gated and ligand-gated ion channels. However, the mechanisms by which one or more of these effects produces general anesthesia and the specific sites of action are poorly understood [GH03].

Immobility is an especially important and desired endpoint of anesthesia during surgical procedures. Recent data indicate that anesthetics can produce immobility predominantly through a direct action on the spinal cord [AJC05] [JBH08]. Because the lamprey spinal central pattern generator (CPG) is one of the best-characterized vertebrate neuronal systems in terms of cellular properties and interactions, it makes an excellent experimental model to study anesthetic action (the neural underpinnings of immobility) in the spinal cord. It also has the potential to serve as a “simple” network model to study principles of anesthetic action in higher order networks that underlie consciousness and memory. Experimental studies in both rodents [JBH08] and lamprey suggests that isoflurane acts preferentially at ventral spinal sites where locomotor CPG neurons and motoneurons are situated, but anesthetic effects on specific populations of locomotor interneurons have not been studied [Jin05]. Elucidating the mechanisms that underlie isoflurane’s effect on locomotor interneurons will allow development of safer anesthesia methods. Multiple possible mechanisms have been hypothesized. Inherent difficulty in experimentally identifying locomotor interneurons warrants the aid of mathematical models.

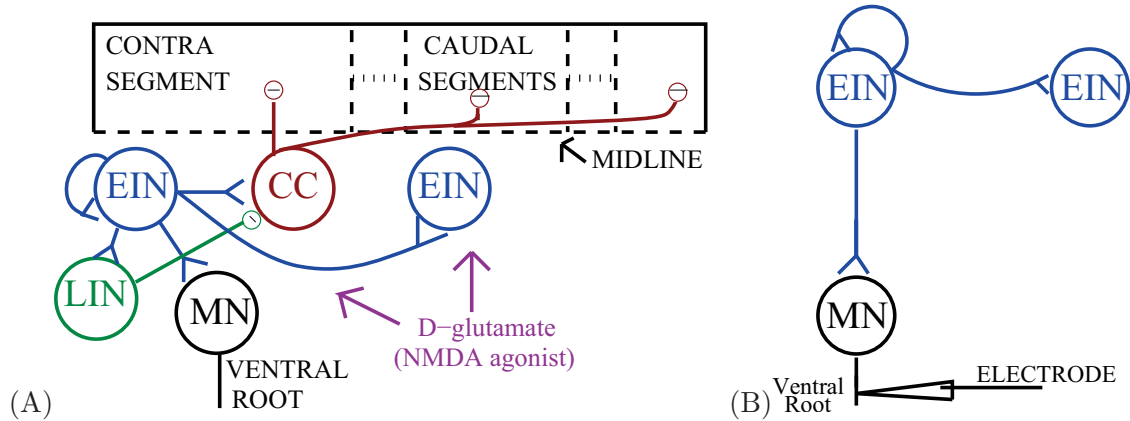


FIGURE 9.1. (A) A proposed model for the single segment locomotor network (Buchanan et al, 1999). Cross commissural inhibitory interneurons (CC interneurons) provide reciprocal inhibition to mediate left-right coordination of rhythmic activity. Lateral inhibitory interneurons (LIN) provide one mechanism for burst termination. Excitatory interneurons (EIN) provide excitatory input to each hemisegment. Large circles represent populations of neurons, the dotted line is the midline, forked terminals are excitatory synapses, small circles are inhibitory synapses. (B) The disinhibited hemisegment. The excitatory interneurons provide the sole input to the motoneurons (MN) once inhibition is blocked. This work ignores the long range EIN connections for simplicity. The trace recordings in figures 9.2B, 9.4B, and 9.5 are electrode recordings of lamprey ventral roots.

The lamprey CPG has been subject to a number of modeling studies (see [LHKG98] and references therein). However, very little modeling work has incorporated sufficient biophysical details in order to study the effects of anesthesia [MBK08] and little to no modeling work of anesthesia has been conducted in conjunction with 'simple' biological preparations. The goal of the following chapters is to construct and analyze mathematical models to examine the effects of anesthesia in the lamprey spinal cord. Mathematical modeling is a useful tool to test anesthetic effects on networks and to facilitate biological experiments. This work was performed in collaboration with Dr. Steven Jinks, Department of Anesthesiology & Pain Medicine, University of California, Davis. Jinks uses the lamprey isolated spinal cord to investigate the immobilizing actions of isoflurane [JAD⁺05]. The aim is to create a model whose dynamics are consistent with experimental data from the lamprey spinal cord under the volatile anesthetic isoflurane and to generate experimentally testable predictions.

9.2. Neural network underlying fictive locomotion in lamprey spinal cord

Central pattern generators generate swimming patterns in lamprey spinal cord. Lampreys swim forward with an undulating motion, contracting muscles on opposite sides of each segment in an alternating left-right pattern, creating a wave of contraction

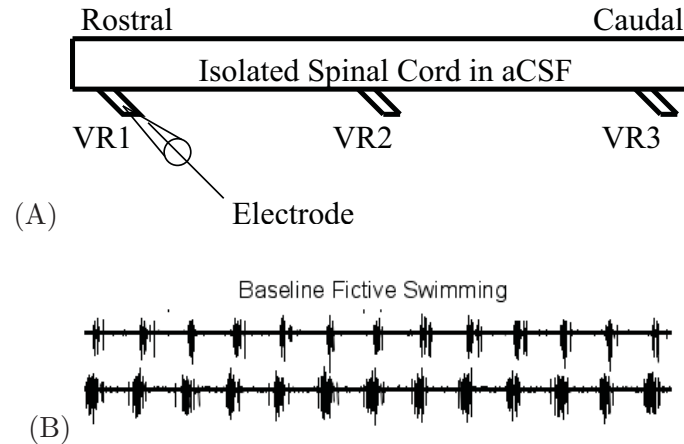


FIGURE 9.2. A sample trace recording (B) with a schematic of the experimental preparation (A). The top recording is from the caudal ventral root and the bottom recording is from the rostral ventral root.

that travels rostrocaudally down their body length [LHKG98]. The swimming pattern is generated by a chain of coupled segmental CPGs in the spinal cord [CG05]. Each CPG is made up of two halves on opposite sides, each with excitatory interneurons (EIN), cross-commissural inhibitory interneurons (CC) and lateral inhibitory interneurons (LIN) with connectivity shown in Figure 9.1A [Buc99]. Also shown are the intersegmental projections of varying distances from CC and EIN interneurons that act to create a phase lag between segments during fictive swimming [WS95]. The motor neurons in each segment receive input from the EINs and project axons through a ventral root to the muscle tissue [CG05].

Bath-application of excitatory amino acid agonists induce fictive swimming in the isolated spinal cord. In experiments, the lamprey spinal cord is isolated and placed in a bath of artificial cerebrospinal fluid. A suction electrode is used on a ventral root to record motor neuron activity, as illustrated in figure 9.2A. Each ventral root contains axons of numerous nearby motor neurons. The suction electrode records the action potentials in these axons.

When activated by bath-application of excitatory amino acids such as glutamate or N-methyl-D-aspartate (NMDA) [WEL⁺92], motor neuron firing patterns in the isolated spinal cord correspond to the pattern of muscle activation seen in the intact lamprey during swimming behavior. For this reason, one calls the motor pattern observed in the isolated spinal cord ‘fictive swimming’. A long-lasting stable ‘fictive’ swimming pattern similar to *in*

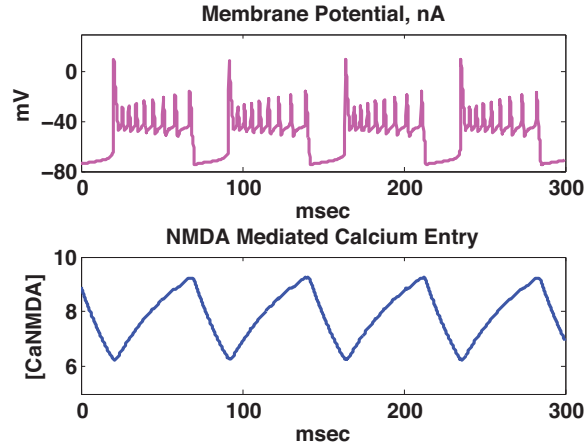


FIGURE 9.3. An example of bursting showing how a slowly changing variable can shape a burst.

in vivo swimming can be induced in the isolated spinal cord by application of NMDA agonists [GMS⁺81] [SGWVD85]. A sample recording is shown in figure 9.2B. Here, bursts describe the ‘average’ behavior of motor neurons, as motor neuron axons project via the ventral root.

Isolated network of excitatory interneurons generate the disinhibited rhythm.

During fictive swimming, a “disinhibited rhythm” can be induced by blocking the inhibitory GABA_A and glycine receptors in the CPG using picrotoxin and strychnine, respectively. As a result, CPG hemisegments in the disinhibited rhythm are no longer coupled via CC interneurons. The LIN interneurons are rendered ineffective, as well. This causes large, low frequency bursts to occur synchronously throughout the spinal cord as the network of EINs are left to generate the CPG rhythm in each segment. The resulting disinhibited rhythm reduces the complexity of the rhythm generating network (figure 9.1B), and permits testing anesthetic effects on excitatory networks alone (figure 9.5A).

Bursting is seen in lamprey CPG. A burst is two or more closely spaced spikes followed by a period of quiescence and generally arises as a result of the interplay between the fast and slow ionic conductances in a neuron [Izh07]. Bursting behavior is seen in a wide range of neurons including the respiratory pacemaker neurons in the pre-Bötzinger complex [BRS99a], leech heart interneurons [ONC95], cat sensorimotor cortical neurons [NAS⁺01], the crayfish swimmeret system (see chapter 2), and lamprey EINs [BG87] [GWD⁺87] [WG87] [HBG89]. Bursting is also seen in ventral root recordings from the disinhibited rhythm of the isolated lamprey spinal cord (figure 9.5A). Since the EINs are capable of

bursting intrinsically and they are connected via excitatory synapses, it is possible that bursts seen in ventral root recordings are due to both intrinsic and network effects. For our purposes, we assume that the intrinsic properties of the EINs are generating the bursts, and we assume that ventral root recordings closely follow EIN activity. Figure 9.3 uses a biophysical model for an isolated lamprey EIN to demonstrate such activity [BTL⁺91]. During the burst, the slowly changing variable, e.g. intracellular calcium, increases (bottom). The fast currents react to the slow change, leading to cessation of the burst (top). During the interburst interval, or quiescent phase, the slow variable decreases until the cell is able to burst again. This will be explained in more detail in section 10.4.

9.3. Isoflurane action on the isolated spinal cord preparation

The volatile anesthetic isoflurane has multiple target sites. Volatile anesthetics are one class of general anesthetic drugs. They are lipophilic, liquid at room temperature and evaporate easily for administration by inhalation. Isoflurane is a typical volatile anesthetic commonly used in an experimental and clinical setting. When isoflurane is applied to the intact lamprey or the isolated lamprey spinal cord, it causes immobility, or cessation of ventral root activity, with similar doses [Jin05]. However, volatile anesthetics are not simple compounds [RA04]. No single ligand-gated ion channel antagonist or synaptic blocker can mimic their effects, indicating more than one mechanism of action [Nas02]. This makes the task of elucidating the mechanisms underlying the effects of isoflurane a difficult task.

Experimentally study the effects of isoflurane on isolated spinal cord preparation. A schematic of how isoflurane is applied to the bath is shown in figure 9.4. The perfusion system for the preparation has an isoflurane vaporizer in line with the gas flow to permit delivery of isoflurane [JAD⁺05]. In a typical preparation, the isolated spinal cord is placed in a bath of artificial cerebrospinal fluid which is then partitioned into rostral, middle, and caudal thirds. Fictive swimming is induced by applying equal concentrations of D-glutamate (an NMDA agonist) to each compartment to activate all glutamatergic receptors. Isoflurane is then delivered only to the middle compartment, and the effect of isoflurane on ventral root activity is observed. This allows one to assess the effects of isoflurane on CPG activity and coordination [JAD⁺05].

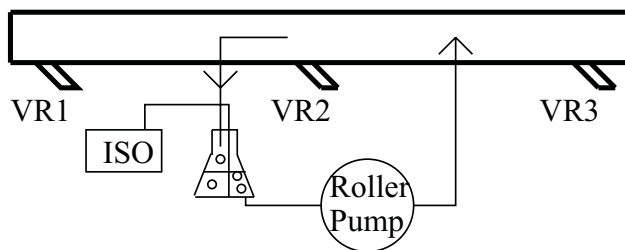


FIGURE 9.4. A schematic of adding isoflurane to the experimental preparation.

Experimental results: isoflurane acts to inhibit EINs via intrinsic and synaptic currents. It was first shown that isoflurane blocks neural activity underlying organized movement in the isolated spinal cord at concentrations similar to those that cause immobility in intact lampreys. Then, in the bath-partitioned preparation, isoflurane was selectively applied to the middle compartment. The neural activity in the ventral root was dose-dependently reduced in all three compartments despite the presence of D-glutamate as a stimulus. The greatest depression of activity occurred in the middle compartment where isoflurane was selectively applied, as expected. More importantly, coordination between outlying anesthetic-free regions is blocked when the middle segment becomes immobile. This demonstrates a direct CPG effect, however, from these results it is not possible to determine how much of isoflurane's immobilizing action is due to direct effects on motor neurons or the CPG. It is conceivable that the majority of isoflurane's immobilizing action is due to direct effects on CPG neurons [Jin05] [JAD⁺05].

It is plausible that isoflurane may lead to immobilization by (1) enhancing inhibitory synapses, (2) depressing recurrent excitatory synapses, or (3) reducing the excitability of EINs directly. To uncover if the inhibitory cell population is fundamental to the effects of isoflurane on the CPG activity, Jinks applied isoflurane to the disinhibited spinal cord preparation during fictive swimming. Preliminary work shows that this set-up does not change the anesthetic requirements for blocking motor output, suggesting that isoflurane may act through direct suppression of the EIN network. Jinks then applied NMDA and AMPA/kainate antagonists to the disinhibited rhythm. The AMPA/kainate antagonists decrease burst frequency, and the NMDA antagonists decrease burst duration and burst frequency. These effects are inconsistent with isoflurane's effect on the disinhibited rhythm.

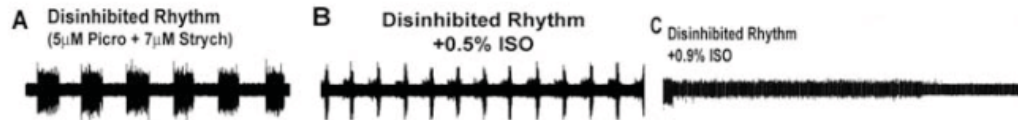


FIGURE 9.5. Effect of isoflurane on the disinhibited rhythm. (A) A disinhibited rhythm was induced by blocking GABA_A and glycine receptors with picrotoxin. The resulting large, low frequency bursts occur synchronously throughout the spinal cord from the lack of intersegmental coupling caused by blocking inhibition. (B) 0.5% isoflurane slowed the disinhibited rhythm by decreasing burst duration (from 21 sec to 2.8 sec) while burst frequency was increased (from .02 Hz to .04 Hz). (C) 0.9% isoflurane caused transient tonic spiking behavior before eliminating the disinhibited rhythm. The concentration needed to abolish the disinhibited rhythm is the same needed to block the normal rhythm.

Transitions in spiking behavior when isoflurane is applied to disinhibited preparation. The effect of isoflurane on the disinhibited rhythm is shown in figure 9.5. Figure 9.5A shows a voltage trace during disinhibited bursting in the absence of isoflurane. When lower isoflurane concentrations, e.g. 0.5% ISO, are added to the rhythm as in Figure 9.5B, the burst duration decreases while burst frequency increases. As step increases in the concentration of isoflurane are taken, e.g. 0.9% ISO as in Figure 9.5C, the bursting behavior transitions to tonic spiking behavior and finally transitions to “silence” when isoflurane takes its full effect. The transition from bursting to tonic spiking behavior as the concentration of isoflurane increases is seen in one-third of the experimental preparations. The remaining preparations show a direct transition from bursting to silence. The low incidence of tonic spiking behavior may result from step increases of isoflurane concentration that are too large to resolve the transition through the tonic firing phase. Another possibility is that isoflurane abolishes EIN activity, but D-glutamate continues to stimulate motoneurons, which as a result exhibit tonic spiking patterns in some preparations. If this is the case, the tonic spiking behavior is not an EIN network property.

Utilize mathematical modeling to understand the biophysical mechanisms underlying isoflurane’s immobilizing action. The full CPG neural network is complicated, but the above experiments suggest that the disinhibited spinal cord preparation captures the essential (predominant) CPG rhythm and the effects of isoflurane on it. The following chapters do not address how coordination in the spinal cord is affected by isoflurane, rather the focus is on how isoflurane establishes immobility in a segment of the spinal cord through its effect on the disinhibited CPG. Figure 9.5 illustrates some of the neural

activity observed in the disinhibited rhythm as the concentration of isoflurane is increased. We use mathematical models to understand what possible targets isoflurane is affecting to get these transitions. The work in this thesis looks for parameter ranges that can easily give both the transition from bursting to silence and the transition from bursting to tonic firing to silence. By studying models and looking for these transitions, we can potentially get insight into what the mechanisms of isoflurane are.

Using a biophysical model, one can more realistically incorporate the hypothesized actions of anesthetics [GH03]. The aim here is to analyze a physiological relevant lamprey spinal model using computer simulation and mathematical analysis in hopes of linking anesthetic modulation of ion channel activity to systems level behavior, specifically immobility. The focus remains on single cell dynamics.

9.4. Previous work on anesthetics

Many studies have used mathematical models to analyze bursting behavior in central pattern generators including those underlying locomotion and respiration [SW96] [WEL⁺92] [HKGL92] [BBR⁺05] [BRS99a]. Some modeling work examines changes in bursting patterns as various parameters are altered, including blocking potassium or sodium conductances to mimic adding TEA or TTX to the system [BTL⁺91], or decreasing the potassium activated calcium conductance to mimic adding 5-HT [WEL⁺92] [HKGL92]. Other models study the dynamical mechanisms involved in burst termination and initiation, as well as possible states (bursting, tonic firing, or silence) that the system may enter depending on parameters [BBR⁺05] [BRS99a]. Similar tactics (i.e. blocking or enhancing relevant ionic conductances) can be utilized to mimic the influences of anesthetics on specific targets. Despite this, there are very few mathematical models that incorporate the effects of anesthesia. This section gives a brief survey of the models that we are aware of.

Effects of propofol on EEG using networks of detailed biophysical cortical cell models. The EEG is commonly used to monitor brain electrical activity during general anesthesia [Ram98]. Under propofol anesthesia at low doses, a ‘paradoxical’ excitation of the network seen through the EEG. The study by McCarthy et al. [MBK08] examines this paradox. They use conductance based models of cortical pyramidal cells and interneurons in

both large and small networks to investigate the effect of propofol-induced GABA_A potentiation. The effects of propofol are modeled by increasing the time constant and amplitude of the synaptic conductance of GABA_A receptors. Their findings suggest that EEG changes associated with ‘paradoxical’ excitation may result from the interplay between the GABA_A and slow potassium M-currents. In their modeling work, this interplay causes a shift from interneuron synchrony at theta frequency to beta frequency anti-synchrony, a mechanism thought to underlie the paradoxical excitation associated with propofol anesthesia.

Effects of propofol and midazolam on GABA_A receptor desensitization modeled using kinetic description of GABA_A. A model by Baker et al. [BPOS02] examines synchronization in a network of cortical interneurons and how the effect of propofol and midazolam on GABA_A receptor desensitization alter this activity. To do this, they construct a model of GABA_A receptor desensitization using kinetic models of ligand-gated ion channels. They alter an existing model of hippocampal CA1 interneurons by incorporating their detailed kinetic description of the GABA_A receptor. This allows for modulation of individual kinetic rates of GABA_A synapses, which alter the time constant and amplitude of inhibitory post-synaptic potentials. Using an isolated single cell, a single cell with an autapse, and a two-cell heterogeneous network, the model predicts a required increase in excitatory input for synchronous behavior under propofol. Under midazolam, however, synchronous behavior occurs for lower levels of excitatory drive. Behaviorally, propofol is used to cause hypnosis and midazolam is used as a sedative-amnestic drug. These results suggest that GABA_A receptor desensitization may contribute to the different behavioral effects of each drug by altering the ability of the networks to synchronize [BPOS02].

Effect of general anesthesia on EEG modeled using cortical mean-field theories. Liley & Steyn-Ross and collaborators [BL05] [LC03] [LB05] [SRSRSL99] [SRSRSW01] [SRSRS04] model general anesthetic effects on the EEG by using a reduction of a cortical mean-field macrocolumn model [LCW99]. The GABA-ergic anesthetic affect that mimics application of propofol is incorporated by increasing the time constant of the inhibitory post-synaptic potential. The model suggests a phase transition in the EEG as unconsciousness is approached under general anesthesia, similar to the paradoxical excitation studied by McCarthy et al. [MBK08]. The model EEG matches experimental evidence for the

biphasic response where brain activity rises at low drug concentrations then falls at higher concentrations.

Effects of volatile and intravenous anesthetics on voltage- and ligand-gated ion channels modeled using biophysical neural models. The study most relevant to the work in this thesis examines anesthetic effects in several mathematical models (Gottschalk & Haney) [GH03]. They use four canonical conductance-based models to examine effects of volatile and intravenous anesthetics. First, the effect of the volatile anesthetic halothane is modeled by decreasing the calcium conductance [HSEL91] in a single compartment model and a two compartment model. The results show that when calcium is the main spike initiating factor in a single compartment, decreasing the calcium conductance will first reduce spike frequency, then terminate the oscillations. In the two compartment model, the dendritic calcium conductance is a somatic burst shaping factor. Decreasing the calcium conductance in this model first prolonged the burst duration, then terminated bursting behavior leaving the soma in tonic spiking mode due its intrinsic currents. This correlates to the lack of burst suppression and lack of isoelectric EEG behavior associated with halothane [BLW64]. Also, the prolonged burst duration is known to occur *in vitro* in the presence of halothane [Pea96].

Secondly, both intravenous (barbiturates, etomidate, propofol, neurosteroids, benzodiazepines) and volatile (isoflurane, halothane, enflurane) anesthetic effects are modeled in an inhibitory neuronal net. The effect of anesthesia is modeled by either increasing the opening rate of GABA_A channels, or decreasing the GABA_A synaptic conductance. The results show that decreasing the GABA_A synaptic conductance leads to an decreased amount of synchrony in a model of the thalamic reticular nucleus network. Curiously, an increase in synchrony is found when the GABA_A synaptic conductance is decreased, or the opening rate of GABA_A is increased in a network of fast-spiking interneurons. The loss of synchrony in the former model might be associated with sedation, amnesia, or decreased levels of consciousness. The increase in synchrony in the latter model might indicate that different components of the CNS contribute in different ways to the behavioral effect of anesthesia [GH03].

All of these studies deal with anesthetic effects on inhibition. In this thesis, we are studying the disinhibited preparation in which inhibition does not play a role, therefore these studies are not relevant to the current work. The McCarthy and Baker studies are not directly relevant to what is proposed here. Although there is evidence that GABA_A receptors play an important role in mediating effects of some intravenous anesthetics, this receptor is not considered a main immobilizing target of volatile anesthetics. The Liley & Steyn-Ross studies are not relevant because we use a detailed model for the proposed work rather than a mean-field cortical model. Furthermore, a biphasic response is not observed in lamprey EINs as the concentration of isoflurane increases.

The Gottschalk & Haney study does pertain to the proposed work in its use of biophysical models to incorporate anesthetic effects by altering relevant parameters. It also points out how altering the same parameter in two different models may lead to dissimilar results, thereby stressing the importance of using a detailed biophysical model of an EIN to study the mechanisms of isoflurane action. However, Gottshalk & Haney also used canonical models, implying that important insights can also come from canonical models that contain enough detail to incorporate the anesthetic effect of interest.

9.5. Isoflurane targets

The following chapters focus on two-pore potassium, persistent sodium, and NMDA channels. Isoflurane is known to enhance the two-pore potassium 'leak' channels TREK and TASK [PHL⁺99] [FDL⁺96], and reduce the persistent sodium channel [SPLIB98]. These channels, although yet to be clearly identified in lamprey excitatory interneurons, have been shown to be present in the spinal cord of mammals such as rats and mice [TSL⁺01], and similar channels are common a broad range of organisms, including yeast, *Drosophila*, *C. elegans*, and mammals. It is also hypothesized that volatile anesthetics block NMDA receptors [DPB⁺07], both explicitly and implicitly via activation of pre- and post-synaptic TREK1 channels [SAD⁺03] [Hon07]. Using both canonical and detailed biophysical models, the following chapters incorporate and study these mechanisms of anesthetic action.

CHAPTER 10

Mathematical Models and the Mechanism of Bursting Using Bifurcation Diagrams

This chapter introduces the two conductance based neuron models used in the following chapter to study the effects of anesthesia. Both models have the ability to exhibit bursting behavior. One is a canonical bursting model [BRS99a] and the other is a biophysical model for a lamprey EIN [BTL⁺91]. Ionic currents relevant to the proposed mechanism of isoflurane action in the lamprey spinal cord are added to the models when needed.

10.1. The Brodin et al. model is a biophysical model of the lamprey EIN

The excitatory interneurons in the lamprey CPG are capable of bursting when exposed to NMDA agonists [WG87]. This EIN behavior has been the basis for a series of models conducted by Grillner and colleagues [EWL⁺91] [BTL⁺91] [KHKA⁺01]. In Ekeberg et al. [EWL⁺91], the basic EIN model containing a soma and three passive dendrites was developed. This model can display a wide range of spiking frequencies (from 10 Hz to 90Hz) over a range of currents (from 1 nA to 7 nA). This model does not exhibit bursting in its normal state. In Brodin et al. [BTL⁺91], the Ekeberg et al. model is expanded by adding an NMDA current to the soma to elicit bursting oscillations. This model can experimentally replicate recorded activity of EINs during constant current injection, Mg^{2+} concentration modifications, and K^+ conductance alterations. It also replicates the experimental burst envelope present in the presence of bath-applied NMDA and tetrodotoxin. The Brodin et al. model is tuned to adequately account for the bursting elicited from EINs by bath-applied NMDA. In Kozlov et al. [KHKA⁺01], the EIN model from Brodin et al. is examined in a network context. One network includes inhibitory interneurons and the other is a single cell with an autapse.

While these EIN models contains biophysical details, the effects of anesthesia have yet to be studied. In this thesis we will study the effects of altering isoflurane target conductances

in a conductance based model of the EIN. The Ekeberg et al. model does not burst and we will only examine isolated cells, therefore the Brodin et al. model is used. It is extended by incorporating the ionic conductances on which isoflurane is thought to act, i.e. the two-pore potassium and persistent sodium conductances. Please see the appendix for a detailed description of this model.

10.2. The Butera et al. model is a minimal bursting model.

While the Brodin et al. model is a biophysical model of an EIN specific to the lamprey system, the bursting model by Butera et al. [BRS99a] was initially developed to analyze bursting interneurons involved in the pre-Bötzing complex. However, it is widely used as a canonical model for bursting neurons. It contains only three state variables, one of which is slow, and therefore lends itself to mathematical analysis (phase plane, and bifurcation analysis). This will be discussed in greater detail in section 10.5. We modify this canonical bursting model by including descriptions of the TREK and TASK channels, and then use it as a starting point for this work. Please see the appendix for a detailed description of this model.

10.3. Hodgkin-Huxley formalism for neuronal models.

Both models described above follow the Hodgkin-Huxley formalism, so the mathematics involved in each take a similar form regardless of their specific ionic currents [KS98a] [KS98b] [Izh07]. Here, we model neurons using single compartment models, which can easily be extended to multi-compartment models. Kirchoff's conservation of current law states that the sum of currents flowing into a neuron must equal the sum of currents flowing out of a neuron. Thus, each model begins with a current balance equation (Equ (10.1)) where $C \frac{dV}{dt}$ is the capacitive current, I_{ion} is the sum of the membrane currents, and I_{app} is an external applied current. The membrane acts as a capacitor and ion channels act as currents, therefore the conservation of current equation is of the form

$$(10.1) \quad C \frac{dV}{dt} = I_{app} - I_{ion},$$

where C is the membrane capacitance (constant), and V is the membrane potential of the neuron being modeled. Each current in I_{ion} is modeled according to Ohm's law. Namely,

for ionic species y , the current I_y is described by

$$(10.2) \quad I_y = \bar{g}_y m^l h^k (V - E_y),$$

where \bar{g}_y is the maximum conductance for the current, $(V - E_y)$ is the driving force and E_y is the reversal potential, or Nernst potential, of the ion carrying the current. The term $m^l h^k$ describes the proportion of open channels in the cell, m models the probability of a channel being in the open state, h models the same for an inactivation state, and l or k may be thought of as the number of activation or inactivation gates in a channel, respectively. Equation (10.2) assumes that gating variables are independent of each other. The gating variables $x = m, h$, are described by first order kinetics.

$$(10.3) \quad \frac{dx}{dt} = \alpha_x(V)(1 - x) - \beta_x(V)x.$$

α_x is the rate constant for the x gates going from the closed to open state and β_x is the rate constant for the x gates going from the open to closed state. Typically, the rate constants are functions of voltage and are usually determined by empirical fits from voltage-clamp experimental data [HH52] [Wil02]. Equation (10.3) may be rewritten as

$$(10.4) \quad \frac{dx}{dt} = \frac{1}{\tau_x(V)}(x_\infty(V) - x)$$

$$(10.5) \quad x_\infty(V) = \frac{\alpha_x(V)}{\alpha_x(V) + \beta_x(V)}$$

$$(10.6) \quad \tau_x(V) = \frac{1}{\alpha_x(V) + \beta_x(V)}$$

where $x_\infty(V)$ is the steady-state gating variable function and $\tau_x(V)$ is the time constant.

10.4. Bursting mechanisms

Most bursting scenarios can be characterized by a separation of fast and slow time scales. Bursting usually results from the interplay between the fast time scales responsible for spiking activity and the slow time scales that modulate the activity [Izh07]. There are many possible mechanisms underlying bursting dynamics in neurons. The following chapter explores the proposed effect of anesthesia on two bursting mechanisms.

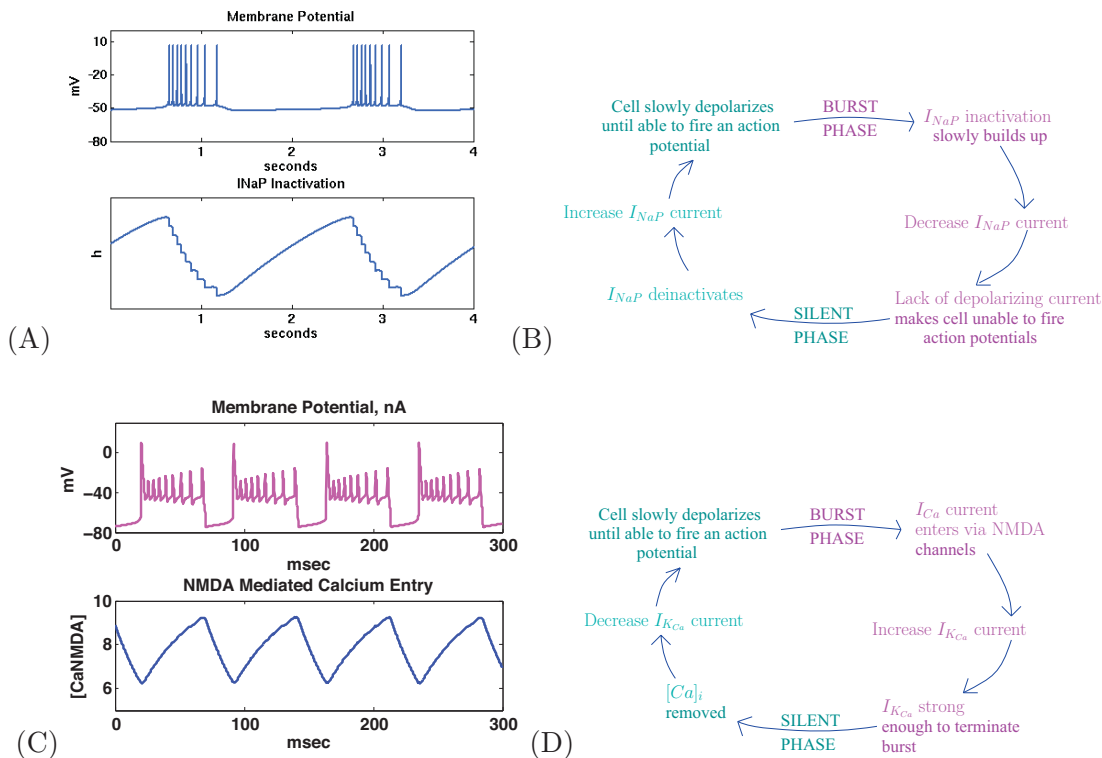


FIGURE 10.1. (A) A sample burst is shown for a model whose bursting is defined by one slow variable. (Modified Butera et al model) (B) A circle diagram describing the exact mechanism for the burst. (C) A biophysical model for a lamprey EIN is used to demonstrate bursting activity. (Modified Brodin et al model) (D) A circle diagram describing the exact mechanism for the burst.

Figure 10.1A shows a sample burst from the canonical bursting model by Butera et al. [BRS99a] along a cycle diagram describing how bursting occurs (figure 10.1B). In this example, the slow time scale is defined by the inactivation of the persistent sodium current. During the burst, the inactivation slowly builds up, decreasing the persistent sodium current. Eventually, the lack of depolarizing current causes the cell to abruptly cease firing. During the interburst interval, or quiescent phase, the persistent sodium current slowly deinactivates causing the cell to depolarize. Eventually the cell depolarizes to a point where it begins to burst again. This will be explained in greater detail in section 10.5.

Figure 10.1C uses the biophysical model for a lamprey EIN by Brodin et al. to demonstrate bursting [BTL⁺91]. A circle diagram explaining the bursting mechanism is shown in figure 10.1D. Here, bursting is induced with bath-applied D-glutamate or NMDA. During the burst, NMDA-mediated calcium slowly enters the cell causing the intracellular concentration of calcium to increase (figure 10.1C bottom). The calcium-activated potassium current

slowly increases as a result. Eventually this outward current is strong enough to abruptly terminate the repetitive oscillations (figure 10.1C top). During the interburst interval, the intracellular calcium is pumped out of the cell. This reduces the strength of the calcium-activated potassium current causing the cell to slowly depolarize until a threshold is reached and it begins to burst again. This will be explained in greater detail in section 11.3.2.

10.5. Understanding bursting through bifurcation analysis

The following analysis explains how to understand the bursting exhibited by the Butera et al. model [BRS99a] using fast-slow time scale decomposition. This is a standard analysis for bursting models, and is also called geometric singular perturbation theory [BBR⁺05] [Izh07] [CB05]. By decomposing the model into its fast and slow subsystems, the complexity is reduced and analysis through bifurcation diagrams is possible. The analysis for the Brodin et al. model [BTL⁺91] is similar.

10.5.1. Basic form for Butera et al. model.

$$(10.7) \quad C \frac{dV}{dt} = -I_{Na} - I_K - I_{NaP} - I_L$$

$$(10.8) \quad I_{Na} = \bar{g}_{Na} m_{\infty}^3(V) (1 - n) (V - E_{Na})$$

$$(10.9) \quad I_K = \bar{g}_K n^4 (V - E_K)$$

$$(10.10) \quad I_{NaP} = \bar{g}_{NaP} m_{\infty,p}(V) h (V - E_{Na})$$

$$(10.11) \quad I_L = \bar{g}_L (V - E_L)$$

$$(10.12) \quad \frac{dh}{dt} = \frac{h_{\infty}(V) - h}{\tau_h(V)}$$

$$(10.13) \quad \frac{dn}{dt} = \frac{n_{\infty}(V) - n}{\tau_n(V)}$$

Please see the appendix for a detailed description of this model.

10.5.2. Fast-slow decomposition. The Butera et al. model is a minimal bursting model, so the bursting behavior can be studied by breaking down the model into fast and slow subsystems. It contains only three state variables: membrane potential V , activation of delayed-rectifier potassium n , and inactivation of persistent sodium h . The time scales for h , V , and n dictate that the evolution of h is much slower than the evolution of V and

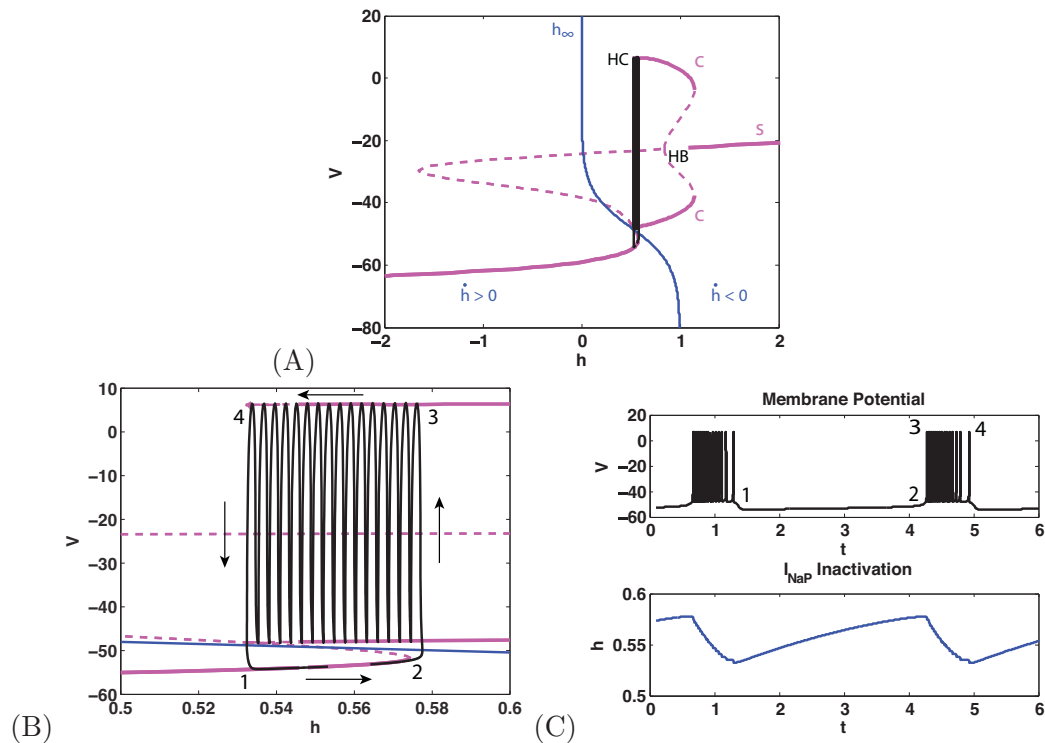


FIGURE 10.2. (A) Schematic of a bifurcation diagram of the fast subsystem of a square wave burster as a slow parameter, h , varies. Solid(dotted) lines correspond to stable(unstable) steady-states. 'S': steady-state curve of fast subsystem, projected onto the V - h plane. 'C': limit cycle steady-state curves. 'HB': Hopf bifurcation. 'HC': Homoclinic bifurcation. ' h_∞ ': superimposed h -nullcline. (B) Closer look at burst trajectory from (A). (C) Voltage trace corresponding to black curve in (A) is shown over time along with change changes in I_{NaP} inactivation parameter, h .

n . That is, τ_h is much greater than τ_n and τ_V ($\tau_h = 10,000$ msec., $\tau_n = 10$ ms, $\tau_V = 1$ ms). Therefore, h may be treated as a parameter on the fast time scale, i.e. h can be held constant on the short time scale, and the fast subsystem consisting of V and n may be analyzed using bifurcation analysis with h as a bifurcation parameter [BBR⁺05]. Then it is possible to examine how the solutions of the full system move along the bifurcation diagram on the slow time scale. A thorough analysis of this type has already been conducted on the Butera model by Butera et al. [BRS99a] and Best et al. [BBR⁺05]. Below, we describe this analysis. A similar analysis is performed on the modified models in the following chapter to study the effects of anesthesia.

Figure 10.2A shows a bifurcation diagram of the Butera et al. fast subsystem where h is the bifurcation parameter. The pink 'S' shaped curve (labeled S) represents the steady-state values for the fast V - n subsystem, projected onto the V - h plane. Solid lines correspond to stable steady-states and dotted lines to unstable steady-states. The upper and lower

branches of ‘S’ consists of focuses or nodes and the middle branch consists of saddle points. Each bend or ‘knee’ of ‘S’ corresponds to a saddle node bifurcation. The pink curves (labeled ‘C’) emanate from the subcritical Hopf bifurcation point on S (labeled ‘HB’), and they represent limit cycle solutions, where solid lines correspond to stable limit cycles and dotted to unstable. The upper and lower solution branches of ‘C’ represent the maximum and minimum voltage oscillation in the limit cycles. The stable limit cycle terminates at a homoclinic bifurcation (labeled ‘HC’), i.e. the limit cycle collides with a saddle point on the middle branch of ‘S’ [Izh07]. For a small range of h (see figure 10.2B), there is bistability between the stable limit cycle solutions and the stable steady-state solutions. This bistability plays a key role in the bursting displayed here.

To understand how the slow dynamics interact with the fast subsystem, the h -nullcline ($h = h_\infty(V)$) is superimposed onto the bifurcation diagram, i.e. the blue line in figure 10.2A. Physiological solutions can only exist between h values of $0 \leq h \leq 1$, but a wider range is shown to give the full picture. When V is below h_∞ , $\dot{h} > 0$ and therefore h is slowly increasing. When V is above h_∞ , $\dot{h} < 0$ and therefore h is slowly decreasing. While h slowly changes, V changes fast enough to bring the dynamics of the full system back to the quasi steady-state. Therefore the full solution adheres to the stable branches of the bifurcation diagram. Figure 10.2B shows an expanded window of figure 10.2A with the trajectory of the bursting dynamics overlaid in black. Figure 10.2C shows the voltage trace corresponding to the trajectory for bursting in the full model over time with points 1-4 corresponding to the same points in (B). The slow variable h , i.e. the persistent sodium current inactivation variable, is also shown to illustrate the time-scale differences between the fast spiking dynamics within the burst and the slowly changing h dynamics.

In figure 10.2B, if the fast subsystem begins on the lower stable branch of ‘S’ (point 1), h increases and the trajectory moves to the right as indicated by black arrows. Once the trajectory passes the saddle-node bifurcation (point 2), the system no longer has a stable quasi steady-state to adhere to. Therefore, the trajectory jumps to the stable limit cycle (point 3) where the fast subsystem oscillates. During these oscillations, V is above h_∞ , so h decreases and the trajectory moves to the left. The slow variable h continues to decrease

until the limit cycle disappears via the homoclinic bifurcation ('HC'). This results in the trajectory falling back down to the lower stable branch of 'S' (point 1). This pattern of bouts of oscillations and quiescence repeats and is known as bursting.

The fact that the transition from silence to oscillations occurs at a different h value than the transition from oscillations to silence is known as *hysteresis* and requires the bistability between the limit cycle and stable steady state in the fast subsystem over a range of h values. The type of bursting described above is called square wave bursting. It is identified by bursts that begin when the resting state vanishes through a saddle node bifurcation and end when the limit cycle vanishes through a homoclinic bifurcation [Izh07] [KS98b]. There are many other types of bursting dynamics associated with different bifurcation diagrams of the fast subsystem [Izh07]. A different type of bursting, called top-hat bursting, is identified by bursts that begin when the resting state vanishes through a saddle-node bifurcation and end when the limit cycle vanishes through a saddle-node bifurcation of limit cycles. The Brodin et al. model displays this type of bursting and is analyzed in the next chapter.

CHAPTER 11

Results

The goal of this chapter is to study the effects of the volatile anesthetic isoflurane using the canonical bursting model of Butera et al. [BRS99a] and a reduced model of the lamprey spinal EIN by Brodin et al. [BTL⁺91]. Recall that as the concentration of isoflurane is increased, the experimental preparation transitions from bursting to tonic firing to silence (figure 9.5). In each model, parameters thought to be affected by isoflurane are altered looking for parameter ranges that give this transition.

11.1. Model for TREK and TASK

Isoflurane is known to enhance the two-pore potassium currents TREK and TASK [PHL⁺99] [FDL⁺96]. However, equations describing their dynamics are not included in the aforementioned models. Therefore, models of the TREK and TASK currents are built here and included in both Butera et al. and Brodin et al. to study the effects of isoflurane on bursting behavior. The equations derived below are based on experimental data from Fink et al. [FDL⁺96] and Patel et al. [PHL⁺99].

TREK and TASK are two-pore potassium currents, which act as outwardly rectifying background leakage currents, i.e. they pass outward current more readily than inward current. Although they are voltage-dependent, they are effectively time-independent [DLF⁺97] [WWBB06]. They are also open near -65mV allowing them to lower the resting membrane potential of the cell [DLF⁺97] [TLSB00]. To generate a model of these currents, experimental data from figure 4B in Fink et al. (using *Xenopus* oocytes) [FDL⁺96] and figure 2B in Patel et al. (using transfected COS cells) [PHL⁺99] are extracted. The data is then fit with exponential curves to capture the nonlinear voltage dependence of each conductance (see figure 11.1). Because each current has the same reversal potential (E_{2P}), the TREK

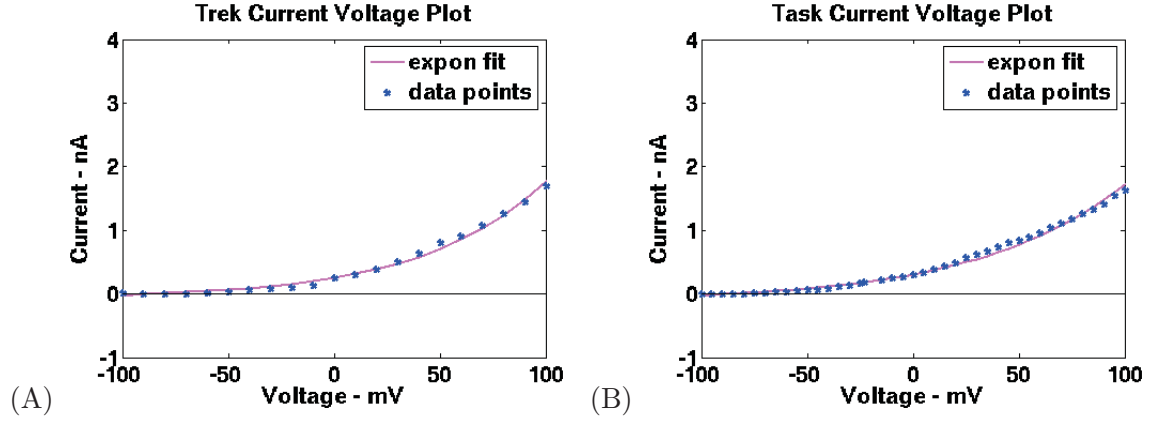


FIGURE 11.1. Extrapolated data points from Fink et al. (A) and Patel et al. (B) shown in blue. The exponential fit to the data is shown in pink. The fit has the same reversal potential as the data.

and TASK conductances are combined into one current equation I_{2P} .

$$(11.1) \quad I_{2P} = (g_{TREK}(V) + g_{TASK}(V))(V - E_{2P})$$

$$(11.2) \quad g_{TREK}(V) = \frac{\beta_{TREK} (.3949 e^{(.0169V)} - .0500)}{(V + 122.2846)}$$

$$(11.3) \quad g_{TASK}(V) = \frac{\beta_{TASK} (.7509 e^{(.0133V)} - .0500)}{(V + 203.7030)}$$

Equations (11.1) - (11.3) define the two-pore potassium current. V is the membrane potential of the cell. $g_{TREK}(V)$ and $g_{TASK}(V)$ are the voltage-dependent conductances of TREK and TASK, respectively. The coefficients β_{TREK} and β_{TASK} are used to modulate the strength of each conductance. The function $S_{2P}(V)$ ($2P$ for two-pore) is introduced to describe the total voltage-dependent conductance for the two-pore potassium current. The coefficient \bar{g}_{2P} is the maximal two-pore potassium conductance.

11.1.1. Normalizing background leakage currents. If the two-pore potassium current, I_{2P} , were simply added to an existing cell model, it would substantially hyperpolarize the cell and increase the input conductance. This would alter the cell's responsiveness to input. Therefore, we must normalize the total background leakage current to ensure that the resting potential and input conductance remain the same regardless of

the magnitude of I_{2P} . To this end, the conductance and reversal potential of the modified background leakage currents must match the original leakage conductance and reversal potential at rest.

Let I_L^* represent the linear leakage current in the modified model. Let E_L^* and g_L^* represent the reversal potential and conductance for I_L^* . If I_{back} represents the total background leakage current in the modified model, then

$$(11.4) \quad I_{2P} + I_L^* = I_{back}$$

$$(11.5) \quad \bar{g}_{2P}S_{2P}(V)(V - E_{2P}) + g_L^*(V - E_L^*) = g_{back}(V - E_{back})$$

$$(11.6) \quad (\bar{g}_{2P}S_{2P}(V) + g_L^*) \left(V - \frac{\bar{g}_{2P}S_{2P}(V)E_{2P} + g_L^*E_L^*}{\bar{g}_{2P}S_{2P}(V) + g_L^*} \right) = g_{back}(V - E_{back})$$

where (11.5) expands the current equations from (11.4), and (11.6) reorganizes the left hand side. To maintain the same leakage conductance and reversal potential at rest ($V = V_{rest}$), g_{back} and E_{back} are matched with the original leakage conductance and reversal potential. This gives restrictions on g_L^* and E_L^* for a chosen value of \bar{g}_{2P} .

$$(11.7) \quad \bar{g}_{2P}S_{2P}(V_{rest}) + g_L^* = g_L$$

$$(11.8) \quad \bar{g}_{2P}S_{2P}(V)E_{2P} + g_L^*E_L^* = g_LE_L$$

The parameters g_L^* and E_L^* ensure that the baseline level of excitability is not altered in the new model because the effect of the new leakage currents are normalized to the original model at rest.

The proportion of two-pore potassium current in the EINs is not currently known. Therefore, we introduce the parameter ρ , which is the proportion of resting leakage conductance due to the two-pore potassium conductance. This will allow us to explore the effect that altering this proportion has on the models. When $\rho = .6$, for example, 60% of the total leakage current is due to I_{2P} and the remaining 40% is due to I_L^* . ρ is defined as

$$(11.9) \quad \rho = \frac{\bar{g}_{2P}S_{2P}(V_{rest})}{\bar{g}_{2P}S_{2P}(V_{rest}) + g_L^*}$$

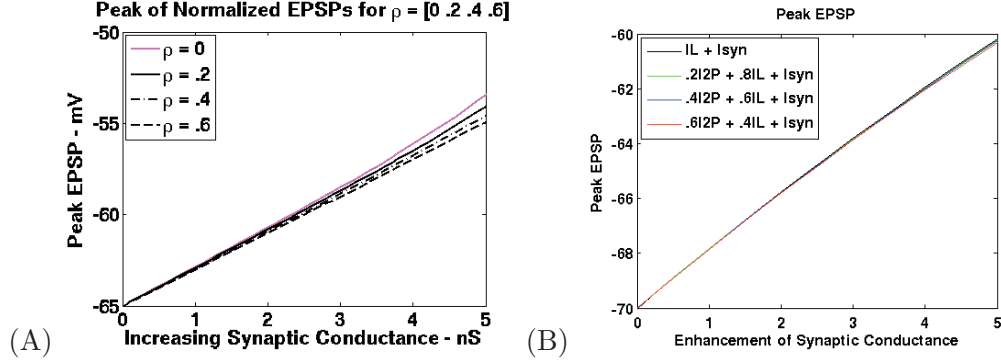


FIGURE 11.2. The peak of the normalized EPSP resulting from an alpha function synaptic conductance is recorded for various ρ values as the strength of the synaptic conductance increases in (A) the modified Butera et al. model and (B) a model equipped with only I_L^* and I_{2P}^* .

With ρ from (11.9), g_L^* and E_L^* become

$$(11.10) \quad g_L^* = g_L(1 - \rho)$$

$$(11.11) \quad E_L^* = \frac{E_L - \rho E_{2P}}{1 - \rho}$$

When $\rho = 0$, the new leakage current reduces to the original leakage current with $g_L^* = g_L$ and $E_L^* = E_L$. Keeping $\rho \in (0, .6)$ ensures E_L^* stays within a reasonable physiological range ($E_L^* \in (-65\text{mV}, -27\text{mV})$).

To demonstrate the effect of this normalization, a subthreshold alpha function synaptic conductance (see appendix) is injected into the model at rest and the change in the peak of the EPSP is monitored as ρ varies (see figure 11.2). In figure 11.2A, the normalization is tested using the modified Butera et al. model (described in section 11.2). The change in the size of the EPSP as a function of synaptic conductance is almost independent of ρ for synaptic conductances less than 3nS, i.e. EPSPs less than 5mV. The deviation in EPSPs at higher synaptic conductances results from the interaction between the rectification of the two-pore potassium current and other non-linearities in the cell. In figure 11.2B, the normalization is tested using a model equipped with only the new leakage currents. As the magnitude of the synaptic conductance increases, the size of the EPSP changes only slightly with ρ .

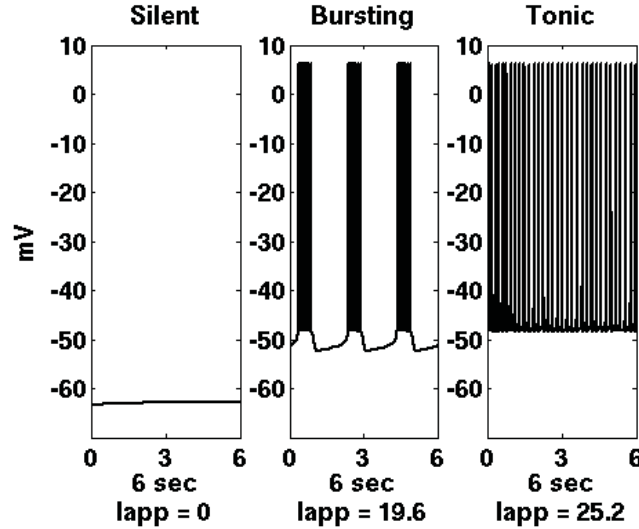


FIGURE 11.3. Three steady state behaviors of the modified Butera et al. model. Silence, bursting, and tonic firing are achieved for various applied current values (I_{app}).

11.2. The Modified Butera et al. Model

In this section, a canonical bursting model by Butera et al. is modified and studied using simulations, parameter exploration, and bifurcation analysis. We study how the bursting activity, which is primarily shaped by the inactivation of persistent sodium current h (figure 10.1A,B), is modulated by \bar{g}_{NaP} and \bar{g}_{2P} . The Butera et al. model, introduced in chapter 10, is capable of three steady state behaviors as seen in figure 11.3: bursting, tonic firing, and silence. The TREK and TASK currents, collectively referred to as I_{2P} , are added. The new background leakage currents, I_L^* and I_{2P} , are normalized as in section 11.1.1. Please see the appendix for a detailed description of the modified Butera et al. model.

11.2.1. Enhancing I_{2P} while blocking I_{NaP} reduces excitability. Isoflurane is known to enhance the two-pore potassium current [PHL⁺99] [FDL⁺96] and block the persistent sodium current [SPLIB98] (section 9.3 and 9.5). Therefore we will model the effect of isoflurane on bursting by enhancing the maximum conductance of I_{2P} and blocking the maximum conductance of I_{NaP} .

To test that enhancing I_{2P} and blocking I_{NaP} puts the cells in a less excitable state in accordance with the experimental effects of isoflurane, we alter the two maximal conductances and measure the excitability of the cells (figure 11.4). Excitability is measured by

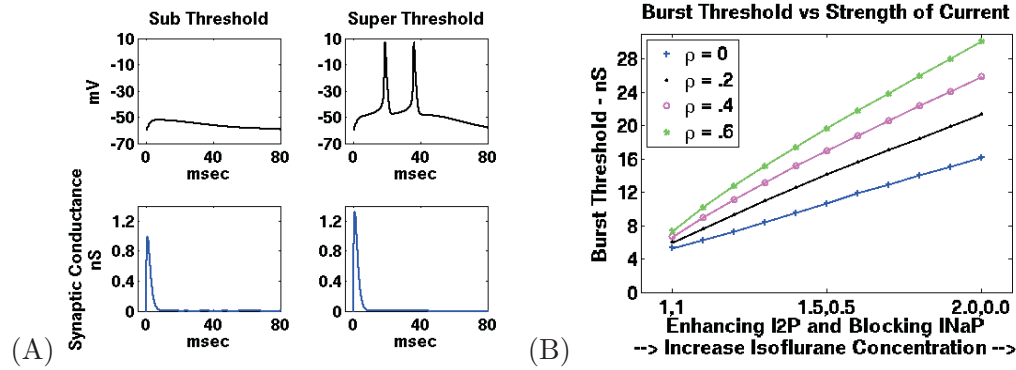


FIGURE 11.4. A) Burst threshold, defined as the minimum amount of synaptic conductance required to elicit an impulse, is demonstrated. In the left column, the synaptic conductance is not large enough to elicit a burst where in the right column it is. B) Burst threshold is measured as the two-pore potassium conductance is enhanced and the persistent sodium conductance is blocked in the modified Butera et al. model. I_{2P} is enhanced by altering the maximal conductance by $1.0 * \bar{g}_{2P}$ through $2.0 * \bar{g}_{2P}$. I_{NaP} is blocked by altering the maximal conductance by $1.0 * \bar{g}_{NaP}$ through $0.0 * \bar{g}_{NaP}$.

burst threshold, i.e. the minimum synaptic input required to elicit an impulse or burst (illustrated in figure 11.4A). This process is repeated for various values of ρ , where ρ describes the proportion of the total leakage current due to the two-pore potassium current. Figure 11.4B, shows that for a fixed ρ , enhancing I_{2P} while blocking I_{NaP} decreases excitability, resulting in an increased burst threshold. For all strengths of I_{2P} and I_{NaP} (i.e. all concentrations of isoflurane tested), burst threshold increases as ρ increases due to the outward rectification of the two-pore potassium currents. The outward rectification hyperpolarizes the cell, which reduces excitability. Thus, increasing the concentration of isoflurane, modeled by enhancing I_{2P} and blocking I_{NaP} , acts to increase burst threshold in the model and reduces excitability, as expected. In addition, burst threshold will increase if either the persistent sodium conductance is solely blocked or the two-pore potassium conductance is solely enhanced (results not shown).

11.2.2. Possible bifurcation route for bursting to tonic to silent transition. In this and the following sections, we analyze the effects of isoflurane on spontaneous bursting activity. We do this by using the techniques from section 10.5, which explain how to understand bursting in this model using a fast-slow time scale decomposition. Furthermore, a thorough bifurcation analysis was conducted previously for the Butera et al. model [BBR⁺05]. Here, a similar analysis is conducted to determine if the modified Butera et al. model is capable of transitioning from bursting to tonic firing to silence through a

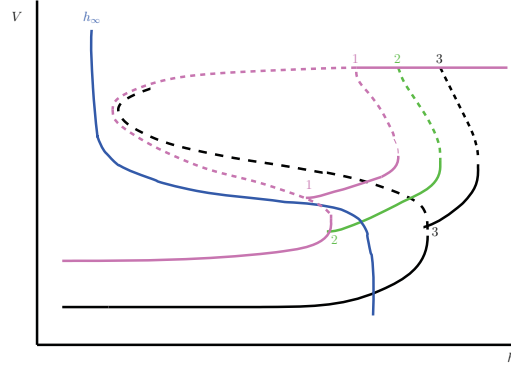


FIGURE 11.5. Schematic bifurcation diagrams showing the transition from bursting to tonic to silence. Starting with the model in bursting mode (1), a loss of bursting through a SNIC bifurcation (2) will lead to tonic firing. If a globally attracting steady state is created (3) the system moves to silence. Solid(dotted) lines correspond to stable(unstable) steady states. 'S' shaped pink and black curves are steady state curves of fast subsystem, projected onto the V - h plane. Inverted 'C' shaped pink, green, and black curves are limit cycle steady states emanating from a Hopf bifurcation. ' h_∞ ': superimposed h -nullcline.

continuous decrease in \bar{g}_{NaP} and increase in \bar{g}_{2P} . Some experimental preparations show recordings transitioning from bursting to tonic firing to silence as the concentration of isoflurane is increased (see figure 9.5). Other preparations show a transition directly from bursting to silence as the concentration of isoflurane is increased [Jinks et al., *unpublished*]. It is already known that the Butera et al. model is capable from transitioning from bursting to silence by decreasing \bar{g}_{NaP} (see [BRS99a]). Here we address the question if increasing \bar{g}_{2P} will allow the model to transition from bursting to tonic firing to silence.

This section looks for the possible sequence of changes to the bifurcation diagram of the fast subsystem that will give the transition from bursting to tonic to silence. This sequence of changes is known as the bifurcation route because qualitative differences between diagrams occur through bifurcations. Figure 11.5 shows an example of one such set of bifurcation diagrams (only the lower limit branches corresponding to the limit cycle solutions are shown). The bifurcation diagrams in figure 11.5 are schematic. The bifurcation analysis is explained in a manner similar to that in section 10.5. Figure 11.5, shows a series of three bifurcation diagrams of the fast subsystem, each describing the state of full system when overlaid with the h -nullcline.

- (1) Suppose, when there is no isoflurane, the system is in bursting mode. The corresponding bifurcation diagram of the fast subsystem (pink) and the h -nullcline

might look like figure 11.5 (labeled 1). Notice that bursting occurs because of the bistability in the fast subsystem between the stable steady state and the limit cycle, with an intersection of h_∞ and the middle, unstable, branch of ‘S’.

- (2) Now suppose isoflurane is added and has an effect that shifts the bifurcation structure of the fast subsystem in the following fashion. If the homoclinic bifurcation moves down to intersect the saddle node bifurcation, bistability is lost through a SNIC bifurcation. The corresponding bifurcation diagram might look like the green steady state curve in figure 11.5 (labeled 2). Along the way, the system transitions from bursting to tonic firing as the trajectory becomes trapped on the stable limit cycle branch. This happens because during the oscillation V is spending time both above the h -nullcline and below the h -nullcline. The trajectory gets pinned where there is a balance between the increase and decrease in h value. Thus, the trajectory remains on the stable limit cycle branch and the full system is tonically firing.
- (3) Now, if the isoflurane concentration is increased further and has an effect that shifts the lower and middle branches of the pink steady state curve to the right by a sufficient amount (black curves, 3), the model enters a silent mode. This happens because a globally attracting steady state is created when the h_∞ curve (blue) intersects the stable branch of the steady state curve for the fast subsystem (black). Note that this corresponds to a saddle node bifurcation in the full system.

The transitions outlined in steps 1,2, and 3 describe one possible bifurcation route for a square wave bursting model (defined in section 10.5) to transition from bursting to tonic firing to silence. This was the only bifurcation route that we found to give the transition from bursting to tonic firing to silence. There might be other bifurcation routes, but this is the most obvious and clear cut for square wave bursters like the Butera et al. model.

11.2.3. Altering \bar{g}_{2P} and \bar{g}_{NaP} does not show the transition from bursting to tonic to silent. Recall from chapter 9 that isoflurane is thought to block neural activity underlying organized movement in the isolated spinal cord by targeting the two-pore potassium and persistent sodium currents in spinal neurons. In this section, parameters relevant

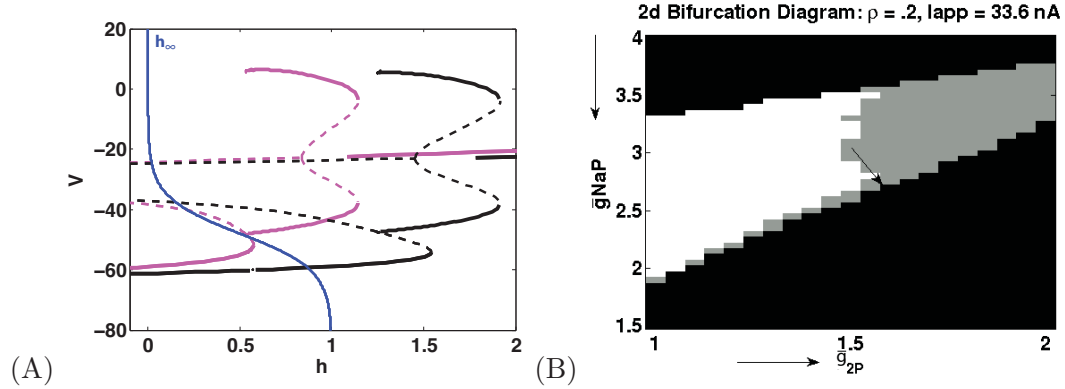


FIGURE 11.6. (A) Effect on modified Butera et al. model of changing parameters to model adding isoflurane. Beginning with the system in bursting mode, I_{2P} is enhanced by increasing g_{2P} and I_{NaP} is diminished by decreasing g_{NaP} . As a result the upper knee shifts left and the lower knee shifts right. The system transitions from bursting to silence with no possibility of tonic firing in between. (B) Two dimensional bifurcation diagram showing how the state of the model changes as the parameters \bar{g}_{2P} and \bar{g}_{NaP} are altered. Black corresponds to silence, grey to bursting and white to tonic firing.

to isoflurane action are altered in the modified Butera et al. model, and the resulting dynamics are studied using fast-slow decomposition. Blocking I_{NaP} is modeled by decreasing the maximum conductance \bar{g}_{2P} . Enhancing I_{2P} is modeled by increasing \bar{g}_{2P} . Consider the bifurcation diagrams of the fast subsystem in figure 11.6A. The pink bifurcation diagram corresponds to the full system in bursting mode with no isoflurane (similar to what is described in sections 10.5 and 11.2.2). If isoflurane is added and \bar{g}_{2P} is increased while \bar{g}_{NaP} is decreased, the system moves from bursting to silence without the possibility of tonic firing. This results from the saddle node bifurcation on the lower branch of ‘S’ crossing the h -nullcline without the minimum of the limit cycles dipping below the h -nullcline. As that happens, a globally attracting steady state is created for the system, which causes silence.

To further explore if the transition from bursting to tonic firing to silence is possible by altering I_{2P} and I_{NaP} , two-parameter bifurcation diagrams are analyzed. Figure 11.6B shows a two-parameter bifurcation diagram for \bar{g}_{2P} and \bar{g}_{NaP} , for which $\rho = .2$ and $I_{app} = 33.6\text{nA}$ and all other parameters are as in the appendix. The diagram is constructed using full numerical simulations of the modified Butera et al. model. This diagram does not capture the possibility of a bistable firing mode because only one initial condition is used per square. Bursting is represented by grey squares, tonic firing by white squares, and silence by black squares. Bursts are distinguished from tonic spiking by identifying particularly large interspike intervals relative to other interspike intervals. The full classification algorithm is

outlined in Butera et al. [BRS99b]. We note that this classification system used has trouble distinguishing between borderline bursting and tonic firing because it is difficult to identify the ‘particularly large’ interspike intervals during the smooth transition between the two behaviors. Thus, borderline behavior leads to the scattered grey squares (bursting) in a region dominated by white (tonic firing).

Figure 11.6B shows an example of a two-parameter bifurcation diagram for decreasing \bar{g}_{NaP} and increasing \bar{g}_{2P} . These parameter changes take system from bursting to silence or from tonic firing to silence. It is not possible to transition from bursting to tonic firing to silence. In fact, we generated these bifurcation diagrams over a large range of values for ρ and I_{app} , and this is the only diagram where the transition even came close (see arrow). These results suggest that it is unlikely that the transition from bursting to tonic firing to silence occurs in this model by altering \bar{g}_{2P} and \bar{g}_{NaP} . Therefore, the bursting displayed by EINs and the transition to silence seen with the application of isoflurane in experiments are most likely due to an alternate burst mechanism and/or an alternate isoflurane target mechanism.

11.3. The Reduced and Modified Brodin et al. Model

In this section, the biophysical model by Brodin et al. [BTL⁺91] for the lamprey EIN is reduced to a minimal model and modified to add the two-pore potassium and persistent sodium currents. Parameter exploration and bifurcation analysis are used to study this model, similar to section 11.2. Bursts in the Brodin et al. model are generated by a different biophysical mechanism from the Butera et al. model, i.e. they are shaped by the calcium-activated potassium current as described in figure 10.1C,D.

11.3.1. The Brodin et al. model is reduced then modified by adding TREK, TASK, and persistent sodium currents. To further study the actions of anesthetics, a biophysical model of a lamprey excitatory interneuron is developed using the model from Brodin et al. as a base [BTL⁺91] [EWL⁺91] [WEL⁺92] [KHKA⁺01]. The original model is designed specifically for simulation of the EIN in the locomotion CPG of the lamprey. It contains four compartments, a somatic compartment and three passive dendritic compartments. The soma contains fast voltage-dependent sodium and potassium currents, an ohmic leak current, a calcium-dependent potassium current, and an NMDA current. The

NMDA current models the effect of applying D-glutamate to the soma and is required to elicit bursting behavior.

In this section the model is systematically reduced to preserve the qualitative behavior of the model neuron following a similar method to that in Butera & Clark [BC96]. First, the passive dendrites are eliminated, which only reduces the load on the soma slightly. To further reduce the model, gating variables that activate or inactivate on time scales much smaller than the membrane time constant are assumed to activate or inactivate instantaneously. Thus, the activation and inactivation variables for the fast sodium current, m and h , are set to their steady state values. As a final step in the reduction, we take h to be $1 - n$, where n is the activation of the potassium current. This is a standard spiking reduction in Hodgkin-Huxley type models [BC96]. The state variable p , which models the voltage-sensitive Mg^{2+} block of the NMDA channels, is also set to its steady state value.

These changes do not significantly alter the dynamics of the model for our purposes, as it maintains the qualitative bursting behavior and same burst mechanism of the original model. Our reduced Brodin et al. model is a three variable model with variables V , n and $[Ca_{NMDA}]$, where $[Ca_{NMDA}]$ is the intracellular concentration of calcium that enters through the NMDA channels. V and n are much faster than $[Ca_{NMDA}]$.

The reduced model is then modified by adding the previously described TREK and TASK currents, which are normalized in the same manner discussed in section 11.1.1. An instantaneously activating persistent sodium current with no inactivation variable is also added (taken from model 2 in Butera et al. [BRS99a]). These currents are added because they are targets of isoflurane, along with the NMDA current. See the appendix for a detailed description of the reduced and modified Brodin et al. model.

11.3.2. Fast-slow analysis of bursting. The reduced and modified Brodin et al. model described above contains three state variables: two fast (V, n) and one slow ($[Ca_{NMDA}]$). As in section 10.5, a fast-slow decomposition is performed to examine the mechanism underlying bursting, however it is slightly different because the slow variable is not the inactivation of the persistent sodium current, h . Figure 11.7A shows a bifurcation diagram of the

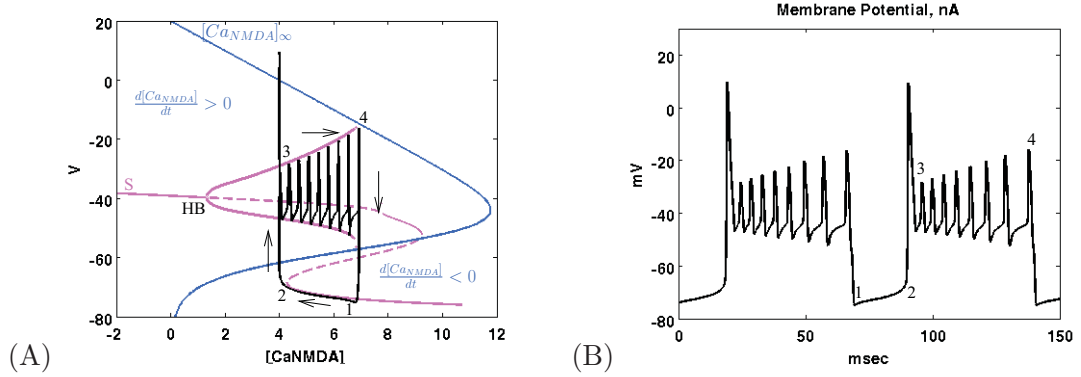


FIGURE 11.7. (A) Bifurcation diagram of the fast subsystem in the reduced and modified Brodin et al. model is shown as the slow parameter $[Ca_{NMDA}]$ varies. Solid lines correspond to stable steady states. Dotted lines correspond to unstable steady states. 'S': steady state curve of fast subsystem projected onto $V - [Ca_{NMDA}]$ plane. 'C': limit cycle steady state curves. 'HB': Hopf bifurcation. 'HC': Homoclinic bifurcation. ' $[Ca_{NMDA}]_{\infty}$ ': superimposed $[Ca_{NMDA}]$ -nullcline. (B) The voltage trace corresponding to black trace in (A) is shown over time.

modified Brodin et al. fast subsystem where $[Ca_{NMDA}]$ is the bifurcation parameter. The pink 'reverse-S' shaped curve (labeled 'S') represents the steady-state values for the $V-n$ fast subsystem projected onto the $V - [Ca_{NMDA}]$ plane. The pink curves emanating from the Hopf bifurcation point (labeled 'HB') on 'S' represent limit cycle solutions. Solid lines correspond to stable steady states and limit cycles. Dotted lines correspond to unstable steady states and limit cycles. The stable limit cycle terminates at a saddle node bifurcation of limit cycles (point 4), i.e. stable and unstable limit cycle solutions collide and then disappear. This particular bifurcation behaves similarly to the homoclinic bifurcation in the Butera et al. model because the period of spiking is increasing towards the end of the burst. For a range of $[Ca_{NMDA}]$ there is bistability between the stable limit cycle solutions and the stable steady-state solutions. This bistability plays a key role in the bursting displayed here.

To understand how the slow dynamics interact with the fast subsystem, the $[Ca_{NMDA}]$ -nullcline ($[Ca_{NMDA}]_{\infty}(V)$) is superimposed onto the bifurcation diagram (blue curve in figure 11.7A). The trajectory of the bursting dynamics is overlaid in black. Figure 11.7B shows the voltage trace corresponding to this trajectory over time with points 1-4 corresponding to the same points in (A). When V is to the right of $[Ca_{NMDA}]_{\infty}$, $\frac{d[Ca_{NMDA}]}{dt} < 0$ and $[Ca_{NMDA}]$ is slowly decreasing. When V is left of $[Ca_{NMDA}]_{\infty}$, $\frac{d[Ca_{NMDA}]}{dt} > 0$ and

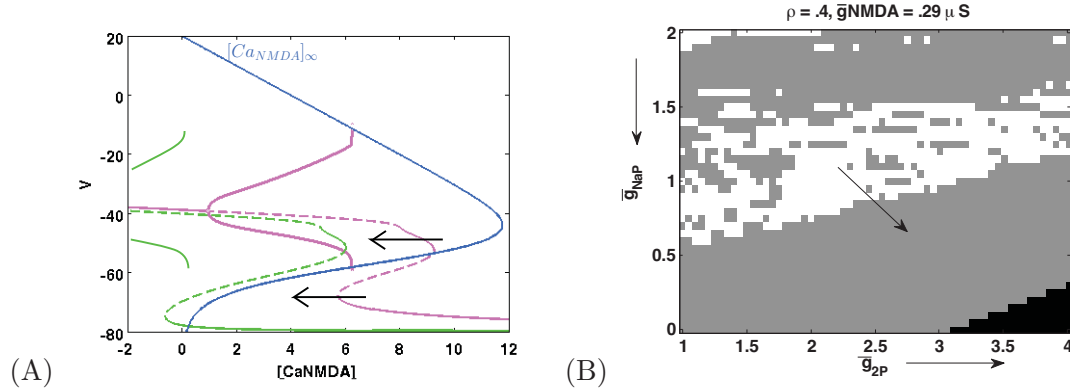


FIGURE 11.8. (A) Hypothesis #1. Beginning with the system in bursting mode (Pink), increase \bar{g}_{2P} and decrease \bar{g}_{NaP} in accordance with isoflurane. The upper and lower knees shift left (Green). The system transitions from bursting to silence without the possibility of tonic firing. (B) Two dimensional bifurcation diagram showing how the state of the model changes as the parameters \bar{g}_{2P} and \bar{g}_{NaP} are altered in accordance with isoflurane. Black corresponds to silence, grey to bursting and white to tonic firing.

$[Ca_{NMDA}]$ is slowly increasing. If the fast subsystem begins on the lower stable branch of 'S' (point 1), $[Ca_{NMDA}]$ decreases and the trajectory moves to the left as indicated by black arrows. Once the trajectory reaches the saddle node bifurcation (point 2), the system no longer has a stable quasi steady-state to adhere to. Therefore, the trajectory jumps up to the stable limit cycle (point 3) where the fast subsystem oscillates. During these oscillations, V is to the left of $[Ca_{NMDA}]_{\infty}$ so $[Ca_{NMDA}]$ increases and the trajectory moves to the right. The slow variable $[Ca_{NMDA}]$ continues to increase until the limit cycle disappears via the saddle node bifurcation of limit cycles (point 4). This results in the trajectory falling back down to the lower stable branch of 'S' (point 1). This pattern repeats, creating the bursting seen in figure 11.7B. This is classified as top-hat bursting, as mentioned in section 10.5 [Izh07].

11.3.3. Altering \bar{g}_{2P} and \bar{g}_{NaP} does not show the transition from bursting to tonic to silent. Recall that many of the experiments show a transition from bursting to tonic firing to silence as the concentration of isoflurane is increased (figure 9.5), while others show a transition directly from bursting to silence. Here, the reduced and modified Brodin et al. model is studied to see if these transitions are both possible by modeling the effects of isoflurane. We model the action of isoflurane by decreasing the maximum conductance of I_{NaP} and increasing the maximum conductance of I_{2P} .

Consider the set bifurcation diagrams of the fast subsystem in figure 11.8A. The pink bifurcation diagram corresponds to the system in burst mode with no isoflurane (similar to what was described in section 11.3.2). When \bar{g}_{2P} is increased and \bar{g}_{NaP} is decreased, the system moves from bursting to silence without the possibility of tonic firing (green bifurcation diagram). This results from the saddle node bifurcation on the lower left knee of 'S' crossing the $[Ca_{NMDA}]$ -nullcline without the minimum of the limit cycles dipping below the h -nullcline. As that happens, a globally attracting steady state is created for the system, which causes silence.

To further explore if the transition from bursting to tonic firing to silence is possible by altering \bar{g}_{2P} and \bar{g}_{NaP} , two-parameter bifurcation diagrams are generated as in section 11.2.3. Figure 11.8B shows a typical two-parameter bifurcation diagram for \bar{g}_{2P} and \bar{g}_{NaP} , for which $\rho = .4$ and $\bar{g}_{NMDA} = .29\mu S$ and all other parameters are as in the appendix. Bursting is represented by grey squares, tonic firing by white squares, and silence by black squares. As \bar{g}_{2P} increases and \bar{g}_{NaP} decreases in accordance with increasing the concentration of isoflurane, the system transitions from bursting through a scattered region of tonic firing to bursting and then to silence. The only possible transition to silence is from bursting mode. The scattered bursting seen in the mostly tonic firing section (upper-middle portion of diagram) occurs because of the classification system used (see section 11.2.3). It is not possible to transition from bursting to tonic firing to silence. In fact, we generated these bifurcation diagrams over a large range of values for ρ and \bar{g}_{NMDA} and do not see the transition from bursting to tonic to silence. These results suggest that it is unlikely that the transition from bursting to tonic firing to silence occurs in this model by altering \bar{g}_{2P} and \bar{g}_{NaP} .

11.3.4. Altering \bar{g}_{2P} and \bar{g}_{NMDA} does show the transition from bursting to tonic to silent. As mentioned in section 9.5, isoflurane is known to block the NMDA currents, as well as effecting the two-pore potassium and persistent sodium currents. Thus, isoflurane may block the neural activity underlying organized movement in the isolated spinal cord by blocking I_{NMDA} , blocking I_{NaP} and enhancing I_{2P} , or any combination of these currents. In this section, we model isoflurane by decreasing the maximum conductance \bar{g}_{NMDA} , and increasing \bar{g}_{2P} .

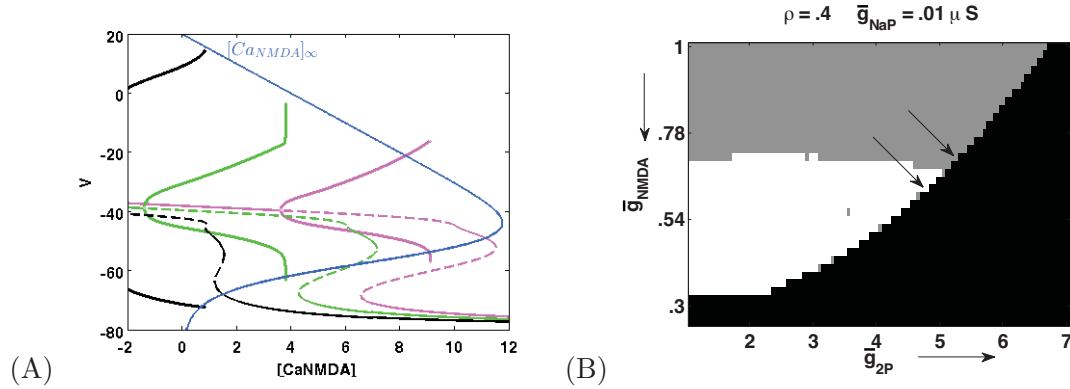


FIGURE 11.9. (A) Hypothesis #2. Beginning with the system in bursting mode (Pink), increase \bar{g}_{2P} and decrease \bar{g}_{NMDA} in accordance with isoflurane. The upper and lower knees shift left while bistability is lost through a SNIC bifurcation (Green). The system transitions from bursting to tonic firing. Further increase \bar{g}_{2P} and decrease \bar{g}_{NMDA} to create a globally attracting steady state (Black) and the system is silent. (B) Two dimensional bifurcation diagram showing how the state of the model changes as the parameters \bar{g}_{2P} and \bar{g}_{NMDA} are altered in accordance with isoflurane. Black corresponds to silence, grey to bursting and white to tonic firing.

Consider the set of bifurcation diagrams of the fast subsystem in figure 11.9A. The pink bifurcation diagram corresponds to the full system in bursting mode with no isoflurane. When \bar{g}_{2P} is increased and \bar{g}_{NMDA} is decreased, the system moves from bursting to tonic firing as bistability is lost through a SNIC bifurcation (green) before the saddle node bifurcation on the lower left knee of ‘S’ crosses the $[Ca_{NMDA}]$ -nullcline. This is a sufficient condition for tonic firing. If \bar{g}_{2P} is increased further and \bar{g}_{NMDA} is decreased further, the system moves from tonic firing to silence (black) as the saddle node bifurcation on the lower left knee of ‘S’ crosses the $[Ca_{NMDA}]$ -nullcline and a globally attracting steady state is created.

To further explore how the transition from bursting to tonic firing to silence occurs by altering I_{2P} and I_{NMDA} , two-parameter bifurcation diagrams are analyzed. Figure 11.9B shows a typical two-dimensional bifurcation diagram for \bar{g}_{2P} and \bar{g}_{NMDA} , for which $\rho = .4$ and $\bar{g}_{NaP} = .01 \mu S$ and all other parameters are as in the appendix. As before, bursting is represented by grey squares, tonic firing by white squares, and silence by black squares. As \bar{g}_{2P} increases and \bar{g}_{NMDA} decreases in accordance with increasing the concentration of isoflurane, the system transitions from bursting to tonic firing to silence. We generated these bifurcation diagrams over a large range of values for $\rho \bar{g}_{NaP}$ and see that the transition from bursting to tonic firing to silence very robust. In fact, you can see that decreasing \bar{g}_{NMDA} alone will give this transition.

The analysis of the reduced and modified Brodin et al. model for EINs suggest that it is unlikely that isoflurane blocks neural activity underlying organized movement in the isolated spinal cord by targeting only \bar{g}_{2P} and \bar{g}_{NaP} . Altering these two parameters allowed for the transition from bursting to silence, but not for the transition from bursting to tonic firing to silence with increased concentration of isoflurane. However, altering \bar{g}_{2P} and \bar{g}_{NMDA} showed both transitions in a very robust way. Thus, this could be the possible mechanism by which isoflurane acts in the lamprey EINs. In fact, the transition from bursting to tonic firing to silence does not require enhancing \bar{g}_{2P} and can be achieved by blocking \bar{g}_{NMDA} alone. Alternatively, if only \bar{g}_{2P} is enhanced, the transition from bursting to tonic firing will not occur and the system will transition from bursting to silence.

Of the parameters tested, blocking \bar{g}_{NMDA} is necessary and sufficient to take the model from bursting to tonic firing to silence, as well as from bursting to silence. Blocking \bar{g}_{NaP} and enhancing \bar{g}_{2P} aid in causing the transition through tonic firing by shifting the steady state curve of the fast subsystem to the left, however, they are not necessary. In order to see the transition from bursting to tonic firing to silence, altering \bar{g}_{2P} and \bar{g}_{NaP} must not cause the transition to silence before altering \bar{g}_{NMDA} has moved the system to tonic firing.

Blocking \bar{g}_{NMDA} decreases the amount of calcium entering the cell. The decreased concentration of intracellular calcium, modeled by $[Ca_{NMDA}]$, reduces the calcium-activated potassium current I_{KCa} . This current is dominant in shaping the bursting dynamics of this model. As I_{KCa} is reduced, the model transitions from bursting to tonic firing. However, it is unclear if \bar{g}_{NMDA} is necessary to cause the transition to tonic firing, or if decreasing \bar{g}_{KCa} would have a similar effect. More work needs to be done to figure out the exact mechanisms.

CHAPTER 12

Conclusion

Experimental data clearly indicates differences among anesthetics with regard to the sites of anesthetic action. Understanding the mechanisms leading to these differences will provide insight into specific anesthetic actions and provide a conceptual framework upon which to develop new anesthetics [AJC05]. Because of its relative simplicity, the lamprey isolated spinal cord can serve as a useful tool to investigate the neurophysiological and pharmacological processes that underlie anesthetic immobilizing action from both an experimental approach and a modeling approach [Jin05]. Working in collaboration with Dr. Steven Jinks, we have constructed and analyzed mathematical models for the lamprey EIN that have begun to uncover the mechanisms underlying the action of isoflurane.

12.1. Summary

The previous chapter used a canonical bursting model and a reduced biophysical model of a lamprey EIN to study the mechanisms of action of the volatile anesthetic isoflurane. Isoflurane is known to target the two-pore potassium current (I_{2P}) [PHL⁺99] [FDL⁺96], persistent sodium current (I_{NaP}) [SPLIB98], and NMDA current (I_{NMDA}) [SAD⁺03] [DPB⁺07]. Therefore, we modeled the effects of isoflurane by enhancing the maximal conductance of the two-pore potassium current and decreasing the maximal conductance of the persistent sodium and NMDA currents. Preliminary experimental results indicate that in some preparations, EINs transition from bursting to tonic firing to silence as the concentration of isoflurane is increased. In other preparations, the EINs transition directly from bursting to silence as the concentration of isoflurane is increased. We found that in the modified Butera et al. [BRS99a] and Brodin et al. [BTL⁺91] models, the transition from bursting to tonic to silence was not possible when the two-pore potassium and persistent sodium conductances were altered in accordance with the action of isoflurane. However, we found that in the modified Brodin et al. model, the transition from bursting to tonic to silence

was seen when the two-pore potassium conductance was enhanced and the NMDA conductance was blocked. In fact, blocking I_{NMDA} alone is both necessary and sufficient to cause the transition from bursting to tonic to silence in this model as well as the transition from bursting to silence. Blocking I_{NMDA} reduces the concentration of intracellular calcium, which reduces the calcium-activated potassium current, $I_{K_{Ca}}$. More work needs to be done to determine which current (I_{NMDA} or $I_{K_{Ca}}$) is responsible for the transition from bursting to tonic firing. These results suggest that isoflurane produces immobility through action on the NMDA current, or possibly the calcium-activated potassium current, in conjunction with the persistent sodium and/or two-pore potassium currents.

12.2. Future Experimental Work

Both models analyzed in the previous chapter describe the intrinsic properties of a single neuron. However, all experimental work regarding the effect of isoflurane in the lamprey has been conducted in a network setting where the motor neuron activity is monitored through ventral root recordings [JAD⁺05]. Therefore, the results in chapter 11 are not directly comparable to experimental data from figure 9.5 and in Jinks et al. [JAD⁺05]. A step towards reconciling this problem from an experimental standpoint is to use intracellular recordings to gather specific cellular EIN properties. Previous studies have performed intracellular recordings from EINs in the isolated lamprey spinal cord preparation (see [GW85] [BG87] [WG87] [HBG89] [WBG⁺89]). However, anesthetics have not been applied during these intracellular recordings. Intracellular recordings during anesthetic application could determine if single EINs transition from bursting to tonic spiking to silence, or directly from bursting to silence, as the concentration of isoflurane is increased. With these experiments, more accurate mathematical modeling and analysis may be performed.

12.2.1. Apply isoflurane during intracellular EIN recordings. The biophysical model proposed in section 11.3 indicates a specific mechanism of anesthetic action in the lamprey EINs. Namely, that isoflurane causes the transition from bursting to tonic to silence by blocking I_{NMDA} , which indirectly activates $I_{K_{Ca}}$. One possible experiment is to apply D-glutamate to elicit oscillations while recording from an EIN intracellularly, then apply isoflurane and study the resulting transition to silence. If the EIN transitions from

bursting to tonic to silence, the modified Brodin et al. model predicts that applying NMDA antagonists will produce the same result, indicating that isoflurane's main effects are on NMDA receptors.

Through ventral root recordings, Jinks has shown that NMDA antagonists do not mimic the action of isoflurane [Jinks, unpublished]. As the concentration of isoflurane increases, burst duration is reduced and burst frequency is increased, before causing tonic firing and then silence. When Jinks applies NMDA antagonists, both burst duration and burst frequency are reduced before causing silence with no transition through tonic firing. Moreover, intracellular recordings in the presence of NMDA antagonists have been done. Wallèn et al. [WG87] used intracellular EIN recordings to study the effect of applying NMDA blockers in the presence of TTX. TTX eliminates the spiking behavior, so the remaining burst envelope may be studied. They found that blocking NMDA reduced the frequency of the remaining membrane oscillations until the cell stopped oscillating. However, it is unclear if the cell transitioned from bursting to tonic firing in this experiment because the spiking currents were blocked. A similar experiment should be repeated without TTX to monitor changes in spiking, as well.

Alternatively, if an NMDA receptor agonist is added to the system in small percentage steps and intracellular EIN recordings show the cells transitioning from silence to tonic firing to bursting, then the Brodin et al. model suggests that isoflurane will reproduce the result. Similarly, if the NMDA agonist is washed out of the preparation in small percentage steps and the EINs transition from bursting to tonic firing to silence, the Brodin et al. model suggests that isoflurane will reproduce the result. There are currently no known studies of this type.

12.2.2. Reduce intracellular Ca^{2+} concentration during intracellular EIN recordings. A second possible experiment is to apply D-glutamate to elicit oscillations while performing intracellular recordings, then remove Ca^{2+} by perfusion with a Ca^{2+} free solution, or simply block all calcium currents with an antagonist. The Ca^{2+} free solution can be achieved by replacing Ca^{2+} with Ba^{2+} (as in Grillner et al. [GW85], Hill et al. [HBG89], and Wallèn et al. [WG87]), or by replacing Ca^{2+} with Mn^{2+} (as in Wallèn et

al. [WBG⁺89]). The latter study addressed the afterhyperpolarization during spiking, and did not study burst dynamics. The former three studies analyzed changes in bursting while spiking currents were blocked with TTX. If a similar experiment is repeated without TTX and the EIN transitions from bursting to tonic to silence, the modified Brodin et al. model predicts that applying isoflurane will reproduce the same result, indicating that isoflurane's main effects are on the calcium currents. While calcium is not considered a main target of isoflurane in this work, several studies have shown that isoflurane is able to depress calcium currents [Stu94] [HL96] [JWL⁺09], and therefore might be a main target in lamprey EINs.

A similar experiment is to apply D-glutamate to elicit oscillations while performing intracellular recordings and then block the calcium-activated potassium current with an antagonist. If EIN transitions from bursting to tonic to silence, the modified Brodin et al. model suggests that applying isoflurane will reproduce the same result, indicating that isoflurane's main effects are on the I_{KCa} current.

12.3. Future Modeling Work

12.3.1. Further analysis of single cell model. Even in the absence of experimental recordings, further modeling work can and should continue. Using the reduced and modified Brodin et al. model (section 11.3), a parameter study can be continued looking for qualitative agreement with Jinks experiments performed while investigating the mechanism of anesthetic action. The model can be analyzed for qualitative changes in burst duration and burst frequency as parameters relevant to isoflurane action are altered. Preliminary analysis has been done on this subject, but results so far remain inconclusive.

Additional experimental work indicates that when NMDA antagonists are applied to the disinhibited rhythm, both burst duration and burst frequency decrease [Jinks, *unpublished*]. The bifurcation scenario of the modified Brodin et al. model (section 11.3) predicts a decrease in burst duration but an increase in burst frequency as NMDA antagonists are applied. This latter characteristic disagrees with what Jinks sees, but more analysis needs to be done in order to make decisive conclusions.

12.3.2. Analyze network of excitatory interneurons in one and many segments. The work presented here modeled and analyzed single cell bursting dynamics. However, the disinhibited rhythm in the lamprey spinal cord consists of a population of EINs in each segment [BG87], i.e. CPG bursts might be inherently generated by network dynamics rather than single cell dynamics. A network of EINs can be built using the single cell model as a base. First, the excitatory synapses may be added with AMPA/kainate currents as in Kozlov et al. [KHKA⁺01]. Then, a model of a population of EINs may be constructed and studied. In each scenario, the effect of isoflurane may be studied by altering relevant parameters such as the NMDA conductance, persistent sodium conductance and two-pore potassium conductance.

12.3.3. Expand topology of network. Noting that EINs project only two-to-three segments in both the rostral and caudal directions [BK99] [CG03] and that normal phase delays can be obtained in the lamprey cord from as few as six segments [MG92], this connection topology can be used to create a model of several segments in the disinhibited spinal cord. Then, the effect of isoflurane on coordination may be studied on the network level. Anesthetic effects may be broken into two components: synaptic vs. intrinsic effects. Anesthetic effects on neuronal coordination may also be studied.

It should be noted that the disinhibited rhythm generated entirely from excitatory interneurons is not behaviorally similar to the original fictive swimming rhythm. In the complete rhythm, the spinal CPG oscillators undergo an alternating left-right active behavior down the length of the spinal cord [BG85] [BG86]. The disinhibited rhythm, on the other hand, experiences lower frequency synchronous bursts throughout the spinal cord [Jinks, *unpublished*]. For this reason, one may model both excitatory (EIN) and commissural inhibitory (CC) interneurons that make up the lamprey CPG. The lateral inhibitory (LIN) interneurons may be ignored because they are not crucial for burst generation or termination, whereas the EIN and CC interneurons are [CG03]. EIN interneurons project 2-3 segments in the rostral and caudal directions [BK99] [CG03]. CC interneurons project 2-3 segments rostrally and about 20 segments cross-caudally [CG03]. Using this topology, a chain of oscillators can be created to model the spinal cord. It is then possible to separate out the rostral, middle, and caudal thirds in order to mimic Jinks' experiments [Jin05] computationally by

incorporating the actions of isoflurane in the middle segment to study the response in the rostral and caudal segments.

APPENDIX B

B.1. Modified Butera et al. model

The minimal Butera et al. [BRS99a] model is modified by adding the two-pore potassium currents, TREK and TASK to study isoflurane modulation of I_{2P} and I_{NaP} conductances.

$$(B.1) \quad C \frac{dV}{dt} = I_{app} - I_{Na} - I_K - I_{NaP} - (1 - \rho)I_L^* - \rho I_{2P} - I_{syn}$$

$$(B.2) \quad \frac{dh}{dt} = \frac{h_\infty(V) - h}{\tau_h(V)}$$

$$(B.3) \quad \frac{dn}{dt} = \frac{n_\infty(V) - n}{\tau_n(V)}$$

$$(B.4) \quad \frac{d^2s}{dt^2} = -2\alpha \frac{ds}{dt} - \alpha^2 s$$

$$(B.5) \quad I_{Na} = \bar{g}_{Na} m_\infty^3(V) (1 - n) (V - E_{Na})$$

$$(B.6) \quad I_K = \bar{g}_K n^4 (V - E_K)$$

$$(B.7) \quad I_{NaP} = \bar{g}_{NaP} m_{\infty,p}(V) h (V - E_{Na})$$

$$(B.8) \quad I_L^* = \bar{g}_L (V - E_L^*)$$

$$(B.9) \quad I_{2P} = \bar{g}_{2P} S_{2P}(V) (V - E_{2P})$$

$$(B.10) \quad I_{syn} = \bar{g}_{syn} s (V - E_{syn})$$

$$(B.11) \quad h_\infty(V) = \left(1 + e^{[(V - \theta_h)/\sigma_h]}\right)^{-1}$$

$$(B.12) \quad \tau_h = \bar{\tau}_h / \cosh [(V - \theta_h)/(2\sigma_h)]$$

$$(B.13) \quad n_\infty(V) = \left(1 + e^{[(V - \theta_n)/\sigma_n]}\right)^{-1}$$

$$(B.14) \quad \tau_n = \bar{\tau}_n / \cosh [(V - \theta_n)/(2\sigma_n)]$$

$$(B.15) \quad m_\infty(V) = \left(1 + e^{[(V - \theta_m)/\sigma_m]}\right)^{-1}$$

$$(B.16) \quad m_{\infty,p}(V) = \left(1 + e^{[(V - \theta_{mp})/\sigma_{mp}]}\right)^{-1}$$

$$(B.17) \quad S_{2P}(V) = \left[\frac{(.3949 e^{(.0169V)} - .0500)}{(V + 122.2846)} + \frac{(.7509 e^{(.0133V)} - .0500)}{(V + 203.7030)} \right]$$

Model Parameters:

$$\begin{aligned} E_{Na} &= 50 \text{ mV} & \bar{g}_{Na} &= 28 \text{ nS} & \theta_m &= -34 \text{ mV} & \theta_h &= -48 \text{ mV} \\ E_K &= -85 \text{ mV} & \bar{g}_K &= 11.2 \text{ nS} & \sigma_m &= -5 \text{ mV} & \sigma_h &= 6 \text{ mV} \\ & & \bar{g}_{NaP} &= 2.8 \text{ nS} & \theta_n &= -29 \text{ mV} & \bar{\tau}_h &= 10,000 \text{ ms} \\ E_L &= -65 \text{ mV} & \bar{g}_L &= 2.8 \text{ nS} & \sigma_n &= -4 \text{ mV} & \theta_{m_p} &= -40 \text{ mV} \\ E_{2P} &= -90 \text{ mV} & \bar{g}_{2P} &= 1 \text{ nS} & \bar{\tau}_n &= 10 \text{ ms} & \sigma_{m_p} &= -6 \text{ mV} \\ E_{syn} &= 0 \text{ mV} & \bar{g}_{syn} &= 1 \text{ nS}^* \\ C &= 21 \text{ pF} & \rho &\in (0, .6) \end{aligned}$$

* $\bar{g}_{syn} = 1 \text{ nS}$ only when measuring burst threshold. $\bar{g}_{syn} = 0 \text{ nS}$ otherwise.

Initial Conditions:

$$V(0) = -65 \text{ mV}, \quad h(0) = .02, \quad n(0) = .7, \quad s(0) = 0, \quad s_p(0) = \alpha^2 **$$

** $s_p(0) = \alpha^2$ only when measuring burst threshold. $s_p(0) = 0$ otherwise.

Definition of Model Parameters and Variables:

I_{app} = applied current (pA)

I_{Na} = sodium current (pA)

I_K = potassium current (pA)

I_{NaP} = persistent sodium current (pA)

I_L^* = normalized leak current (pA)

I_{2P} = two-pore potassium current (pA)

I_{syn} = synaptic current used to measure burst threshold (pA)

$\bar{g}_{Na}, \bar{g}_K, \bar{g}_{NaP}, \bar{g}_L, \bar{g}_{2P}, \bar{g}_{syn}$ = maximal conductance for Na^+ , K^+ , persistent sodium, leak, two-pore potassium, and synaptic currents (nS)

$E_{Na}, E_K, E_L, E_{2P}, E_{syn}$ = equilibrium potentials for Na^+ , persistent sodium, K^+ , leak, two-pore potassium, and synaptic currents (mV)

V = membrane potential (mV)

C = membrane capacitance (pF)

t = time (ms)

$m_\infty(V), m_{\infty,p}(V)$ = steady-state activation functions of sodium and persistent sodium currents

n = activation variable of K^+ current

n_∞ = steady-state activation function of K^+ current

τ_n = rate constant for activation variable of K^+ current

h = inactivation variable of persistent sodium current

h_∞ = steady-state inactivation function of persistent sodium current

τ_h = rate constant for inactivation variable of persistent sodium current

$S_{2P}(V)$ = steady-state activation function for the two-pore potassium current

s = activation of synaptic current

ρ = fraction of normalized leak current attributed to the two-pore potassium current

E_L^*, g_L^* = equilibrium potential and maximal conductance for the normalized leak current, as defined in section 11.1.1

B.2. Reduced and modified Brodin et al. model

The Brodin et al. model [BTL⁺91] is reduced and modified as described in section 11.3.1 to study isoflurane modulation of I_{2P} , I_{NaP} and I_{NMDA} conductances.

$$(B.18) \quad C \frac{dV}{dt} = I_{app} - I_{Na} - I_K - I_{NaP} - (1 - \rho)I_L^* - \rho I_{2P} - I_{KCa} - I_{NMDA}$$

$$(B.19) \quad \frac{dn}{dt} = \alpha_n(1 - n) - \beta_n$$

$$(B.20) \quad \frac{d[Ca_{NMDA}]}{dt} = p_\infty \rho_{NMDA}(E_{NMDA} - V) - \delta_{NMDA}[Ca_{NMDA}]$$

$$(B.21) \quad I_{Na} = \bar{g}_{Na} m_\infty^3(V)(1 - n)(V - E_{Na})$$

$$(B.22) \quad I_K = \bar{g}_K n^4(V - E_K)$$

$$(B.23) \quad I_{NaP} = \bar{g}_{NaP} m_{\infty,p}(V)(V - E_{Na})$$

$$(B.24) \quad I_L^* = \bar{g}_L(V - E_L^*)$$

$$(B.25) \quad I_{2P} = \bar{g}_{2P} S_{2P}(V)(V - E_{2P})$$

$$(B.26) \quad I_{KCa} = \bar{g}_{KCa}[Ca_{NMDA}](V - E_K)$$

$$(B.27) \quad I_{NMDA} = \bar{g}_{NMDA} p_\infty(V - E_{NMDA})$$

$$(B.28) \quad \alpha_n = \frac{A(V - B)}{1 - e^{(B-V)/C}}$$

$$(B.29) \quad \beta_n = \frac{A(B - V)}{1 - e^{(V-B)/C}}$$

$$(B.30) \quad p_\infty = \frac{\alpha_p}{(\alpha_p + \beta_p)}$$

$$(B.31) \quad \alpha_p = A e^{V/C}$$

$$(B.32) \quad \beta_p = A[Mg]e^{-V/C}$$

$$(B.33) \quad m_\infty = \frac{\alpha_m}{(\alpha_m + \beta_m)}$$

$$(B.34) \quad \alpha_m = \frac{A(V - B)}{1 - e^{(B-V)/C}}$$

$$(B.35) \quad \beta_m = \frac{A(B - V)}{1 - e^{(V-B)/C}}$$

$$(B.36) \quad m_{\infty,p}(V) = \frac{1}{(1 + e^{V - \theta_m/\sigma_m})}$$

$$(B.37) \quad S_{2P}(V) = \left[\frac{(.3949 e^{(.0169V)} - .0500)}{(V + 122.2846)} + \frac{(.7509 e^{(.0133V)} - .0500)}{(V + 203.7030)} \right]$$

Model Parameters:

$$\begin{aligned} E_{Na} &= 50 \text{ mV} & \bar{g}_{Na} &= 1 \mu\text{S} & \theta_m &= -40 \text{ mV} \\ & & \bar{g}_{NaP} &= 1 \mu\text{S} & \sigma_m &= -6 \text{ mV} \\ E_K &= -80 \text{ mV} & \bar{g}_K &= .5 \mu\text{S} & \rho_{NMDA} &= .0005 * \text{nmda ms}^{-1} \text{mV}^{-1}) \\ & & \bar{g}_{KCa} &= .04 \mu\text{S} & \delta_{NMDA} &= .002 \text{ ms}^{-1} \\ E_L &= -70 \text{ mV} & \bar{g}_L &= .05 \mu\text{S} & \text{nmda} &= .8 \\ E_{2P} &= -90 \text{ mV} & \bar{g}_{2P} &= 1 \mu\text{S} \\ E_{NMDA} &= 0 \text{ mV} & \bar{g}_{NMDA} &= .45 * \text{nmda} \mu\text{S} \\ C &= .05 \text{ nF} & \rho &\in (0, .6) \end{aligned}$$

		m	n	p
α	A	.2 (mV ⁻¹ ms ⁻¹)	.02 (mV ⁻¹ ms ⁻¹)	.7 (ms ⁻¹)
	B	-45(mV)	-45(mV)	
	C	1(mV)	.8(mV)	10(mV)
β	A	.06 (mV ⁻¹ ms ⁻¹)	.005 (mV ⁻¹ ms ⁻¹)	.0056 (mM ⁻¹ ms ⁻¹)
	B	-54 (mV)	-35 (mV)	
	C	20 (mV)	.4 (mV)	10 (mV)
	[Mg]			1.8 mM

Initial Conditions:

$$V(0) = -70 \text{ mV}, \quad n(0) = 0, \quad [Ca_{NMDA}](0) = 6$$

Definition of Model Parameters and Variables:

I_{app} = applied current (nA)

I_{Na} = sodium current (nA)

I_K = potassium current (nA)

I_{NaP} = persistent sodium current (nA)

I_L^* = normalized leak current (nA)

I_{2P} = two-pore potassium current (nA)

$I_{K_{Ca}}$ = calcium-dependent potassium current (nA)

I_{NMDA} = Bath-activated NMDA current (nA)

$\bar{g}_{Na}, \bar{g}_{NaP}, \bar{g}_K, \bar{g}_{K_{Ca}}, \bar{g}_L, \bar{g}_{2P}, \bar{g}_{NMDA}$ = maximal conductance for Na^+ , persistent sodium, K^+ , Ca^{2+} -dependent K^+ , leak, two-pore potassium, and NMDA currents (μS)

$E_{Na}, E_K, E_L, E_{2P}, E_{NMDA}$ = equilibrium potentials for Na^+ and persistent sodium, K^+ , leak, two-pore potassium, and NMDA currents (mV)

V = membrane potential (mV)

C = membrane capacitance (nF)

t = time (ms)

p_∞ = steady-state fraction of open NMDA channels

α_p, β_p = rate constants describing the unblocking and blocking of the NMDA channel, respectively

$m_\infty(V), m_{\infty,p}(V)$ = steady-state activation functions of sodium and persistent sodium currents

n = activation variable of K^+ current

α_n, α_m = rate by which the potassium and sodium channels switch from a closed to an open state

β_n, β_m = rate by which the potassium and sodium channels switch from an open to a closed state

$[Ca_{NMDA}]$ = concentration of calcium that has entered the cell through the NMDA channel

ρ_{NMDA} = rate of calcium ion influx

δ_{NMDA} = rate of calcium ion decay

$S_{2P}(V)$ = steady-state activation function for the two-pore potassium current

ρ = fraction of normalized leak current attributed to the two-pore potassium current

E_L^*, g_L^* = equilibrium potential and maximal conductance for the normalized leak current, as defined in section 11.1.1

Bibliography

- [AJC05] J. F. Antognini, S. L. Jinks, and E. E. Carstens, *The spinal cord, anesthesia and immobility: A re-examination*, International Congress Series 1283 (2005), 126–131.
- [AOP⁺93] Y. I. Arshavsky, G. Orlovsky, Y. V. Panchin, A. Roberts, and S. R. Soffe, *Neuronal control of swimming locomotion: analysis of the pteropod mollusc *clione* and embryos of the amphibian *xenopus**, TINS **16** (1993), no. 6, 227–233.
- [BBR⁺05] J. Best, A. Borisyuk, J. Rubin, D. Terman, and M. Wechselberger, *The Dynamic Range of Bursting in a Model Respiratory Pacemaker Network*, SIAM J. Applied Dynamical Systems **4** (2005), no. 4, 1107–1139.
- [BC96] R. J. Butera and J. Clark, *Dissection and reduction of a modeling bursting neuron*, J. Comput. Neurosci. **3** (1996), 199–223.
- [BG85] L. Brodin and S. Grillner, *The role of putative excitatory amino acid neurotransmitters in the initiation of locomotion in the lamprey spinal cord. i. the effects of excitatory amino acid antagonists*, Brain Research **360** (1985), 139–148.
- [BG86] ———, *Effects of magnesium on fictive locomotion induced by activation of n-methyl-d-aspartate (nmda) receptors in the lamprey spinal cord in vitro*, Brain Research **380** (1986), 244–252.
- [BG87] J. T. Buchanan and S. Grillner, *Newly identified 'glutamate interneurons' and their role in locomotion in the lamprey spinal cord*, Science **236** (1987), 312–314.
- [BK99] J. T. Buchanan and S. Kasicki, *Segmental distribution of common synaptic inputs to spinal motoneurons during fictive swimming in the lamprey*, J Neurophysiol **82** (1999), 1156–1163.

-
- [BL05] I. Bojak and D. T. J. Liley, *Modeling the effects of anesthesia on the electroencephalogram*, Physical Review E **71** (2005), 041902(22).
- [BLW64] L. E. Brackman, B. Lümfström, and L. Widen, *Electroencephalography in halothane anaesthesia*, Acta Anaesthesiol Scand **8** (1964), 115–130.
- [BM95] G. Braun and B. Mulloney, *Coordination in the crayfish swimmeret system: Differential excitation causes changes in intersegmental phase*, J Neurophysiol **73** (1995), no. 2, 880–885.
- [BPOS02] P. A. Baker, P. S. Pennefather, B. A. Orser, and F. K. Skinner, *Disruption of Coherent Oscillations in Inhibitory Networks With Anesthetics: Role of GABA_A Receptor Desensitization*, J Neurophysiol **88** (2002), 2821–2833.
- [Bro11] T. Brown, *The intrinsic factors in the act of progression in the mammal*, Proc R Soc Lond B Biol Sci **84** (1911), 308–319.
- [Bro14] ———, *On the nature of the fundamental activity of the nervous centres; together with an analysis of the conditioning of rhythmic activity in progression, and a theory of the evolution of function in the nervous system*, J Physiol **48** (1914), 18–46.
- [BRS99a] R. J. Butera, J. Rinzel, and J. C. Smith, *Models of respiratory rhythm generation in the pre-Bötzinger complex. I. Bursting pacemaker neurons*, Journal of Neurophysiology **81** (1999), 382–397.
- [BRS99b] ———, *Models of respiratory rhythm generation in the Pre-Bötzinger complex. II. Populations of coupled pacemaker neurons*, J Neurophysiol **81** (1999), 398–415.
- [BTL⁺91] L. Brodin, H. G. C. Tråvén, A. Lansner, P. Wallén, O. Ekeberg, and S. Grillner, *Computer Simulations of N-Methyl-D-Aspartate Receptor-Induced Membrane Properties in a Neuron Model*, Journal of Neurophysiology **66** (1991), no. 2, 473–484.
- [Buc99] J. T. Buchanan, *Commissural Interneurons in Rhythm Generation and Intersegmental Coupling in the Lamprey Spinal Cord*, J Neurophysiol **81** (1999), no. 5, 2037–2045.
- [CB05] S. Coombes and P. C. Bressloff (eds.), *Bursting: The Genesis of Rhythm in the Nervous System*, ch. 4, 13, World Scientific, 2005.

-
- [CDS92] R. L. Calabrese and E. De Schutter, *Motor-pattern-generating networks in invertebrates: modeling our way toward understanding*, *TINS* **15** (1992), no. 11, 439–445.
- [CG03] L. Cangiano and S. Grillner, *Fast and Slow Locomotor Burst Generation in the Hemispinal Cord of the Lamprey*, *J Neurophysiol* **89** (2003), 2931–2942.
- [CG05] ———, *Mechanisms of Rhythm Generation in a Spinal Locomotor Network Deprived of Crossed Connections: The Lamprey Hemicord*, *The Journal of Neuroscience* **25** (2005), no. 4, 923–935.
- [CW80] A. Cohen and P. Wallén, *The neuronal correlate of locomotion in fish. "fictive swimming" induced in an in vitro preparation of the lamprey spinal cord*, *Exp. Brain Res.* **41** (1980), 11–18.
- [DLF⁺97] F. Duprat, F. Lesage, M. Fink, R. Reyes, C. Heurteaux, and M. Lazdunski, *Task, a human background k^+ channel to sense external ph variations near physiological ph* , *The EMBO Journal* **16** (1997), no. 17, 5464–5471.
- [DPB⁺07] R. Dickinson, B. K. Peterson, P. Banks, C. Simillis, J. C. S. Martin, C. A. Venzuela, M. Maze, and N. P. Franks, *Competitive inhibition at the glycine site of the n -methyl- d -aspartate receptor by the anesthetics xenon and isoflurane*, *Anesthesiology* **107** (2007), 756–67.
- [DRR09] S. Daun, J. Rubin, and I. Rybak, *Control of oscillation periods and phase durations in half-center central pattern generators: a comparative mechanistic analysis*, *J Comput Neurosci* **27** (2009), no. 1, 3–36.
- [EK90] G. B. Ermentrout and N. Kopell, *Oscillator death in systems of coupled neuronal oscillators*, *SIAM J. Appl. Math* **50** (1990), 125–146.
- [EK91] ———, *Multiple pulse interactions and averaging in systems of coupled neural oscillators*, *J. Math. Biol.* **29** (1991), 33–44.
- [Erm02] G. B. Ermentrout, *Simulating, analyzing, and animating dynamical systems: A guide to XPPAUT for researchers and students*, Society for Industrial and Applied Mathematics, 2002.
- [EWL⁺91] O. Ekeberg, P. Wallén, A. Lansner, H. Tråvén, L. Brodin, and S. Grillner, *A Computer Based Model for Realistic Simulations of Neural Networks I. The single neuron and synaptic interaction.*, *Biological Cybernetics* **65** (1991),

81–90.

- [FDL⁺96] M. Fink, F. Duprat, F. Lesage, R. Reyes, G. Romey, C. Heurteaux, and M. Lazdunski, *Cloning, functional expression and brain localization of a novel unconventional outward rectifier K^+ channel.*, The EMBO Journal **15** (1996), no. 24, 6854–6862.
- [GE02] P. Goel and G. B. Ermentrout, *Synchrony, stability, and firing patterns in pulse-coupled oscillators*, Physica D **163** (2002), 191–216.
- [GH03] A. Gottschalk and P. Haney, *Computational Aspects of Anesthetic Action in Simple Neural Models*, Anesthesiology **98** (2003), no. 2, 548–564.
- [GMS⁺81] S. Grillner, A. McClellan, K. Sigvardt, P. Wallén, and M. Wilén, *Activation of nmda receptors elicits "fictive locomotion" in lamprey spinal cord in vitro*, Acta. Physiol. Scand. **113** (1981), 549–551.
- [Gri81] S. Grillner, *Control of locomotion in bipeds, tetrapods, and fish. in: Handbook of physiology. sec. 1: The nervous system. vol. ii. motor control. part 2*, pp. 1179–1236, Bethesda, MD: Am. Physiol. Soc., 1981.
- [GW85] S. Grillner and P. Wallén, *The ionic mechanisms underlying n-methyl-d-aspartate receptor-induced, tetrodotoxin-resistant membrane potential oscillations in lamprey neurons during fictive locomotion*, Neuroscience Letters **60** (1985), 289–294.
- [GW99] ———, *On the cellular bases of vertebrate locomotion*, Prog Brain Res **123** (1999), 297–309.
- [GWD⁺87] S. Grillner, P. Wallén, N. Dale, L. Brodin, J. T. Buchanan, and R. Hill, *Transmitters, membrane properties and network circuitry in the control of locomotion in lamprey*, Trends in Neuroscience **10** (1987), 34–41.
- [HBG89] R. Hill, L. Brodin, and S. Grillner, *Activation of n-methyl-d-aspartate (nmda) receptors augments repolarizing responses in lamprey spinal neurons*, Brain Research **499** (1989), 388–392.
- [HH52] A. Hodgkin and A. Huxley, *A quantitative description of membrane current and its application to conduction and excitation in nerve*, J Physiol. **117** (1952), no. 4, 500–544.

-
- [HKGL92] J. Hellgren Kotaleski, S. Grillner, and A. Lansner, *Computer simulation of the segmental neural network generating locomotion in lamprey by using populations of network interneurons*, Biol. Cybern. **68** (1992), 1–13.
- [HL96] K. Hirota and D. Lambert, *Voltage-sensitive calcium channels and anaesthesia*, British Journal of Anaesthesia **76** (1996), 344–346.
- [Hon07] E. Honoré, *The neuronal background K_{2P} channels: focus on TREK1*, Nature Reviews Neuroscience **8** (2007), 251–261.
- [HSEL91] J. Herrington, R. C. Stern, A. S. Evers, and C. J. Lingle, *Halothane inhibits two components of calcium current in clonal (GH3) pituitary cells*, J Neurosci **11** (1991), 2226–40.
- [HW60] G. Hughes and A. Wiersma, *The co-ordination of swimmeret movements in the crayfish, procambaraus clarkii*, J Exp Biol **37** (1960), no. 4, 657–670.
- [IW64] K. Ikeda and C. Wiersma, *Autogenic rhythmicity in the abdominal ganglia of the crayfish: The control of swimmeret movements*, Comp Biochem Physiol **12** (1964), 107–115.
- [Izh07] E. M. Izhikevich, *Dynamical systems in neuroscience: The geometry of excitability and bursting*, The MIT Press, 2007.
- [JAD⁺05] S. L. Jinks, R. J. Atherley, C. L. Domingues, K. A. Sigvardt, and J. F. Antognini, *Isoflurane Disrupts Central Pattern Generator Activity and Co-ordination in the Lamprey Isolated Spinal Cord*, Anesthesiology **103** (2005), no. 3, 567–575.
- [JBH08] S. L. Jinks, M. Bravo, and S. G. Hayes, *Volatile anesthetic effects on midbrain-elicited locomotion suggest that the locomotor network in the ventral spinal cord is the primary site for immobility*, Anesthesiology **108** (2008), no. 6, 1016–1024.
- [Jin05] S. L. Jinks, *The lamprey isolated spinal cord as a model for anesthetic effects on vertebrate locomotor systems*, International Congress Series 1283 (2005), 172–176.
- [JK06] S. Jones and N. Kopell, *Local network parameters can affect inter-network phase lags in central pattern generators*, J. Math. Biol. **52** (2006), 115–140.

-
- [JMKK03] S. Jones, B. Mulloney, T. J. Kaper, and N. Kopell, *Coordination of Cellular Pattern-Generating Circuits that Control Limb Movements: The Sources of Stable Differences in Intersegmental Phases*, *Journal of Neuroscience* **23** (2003), no. 8, 3457–3468.
- [JWL⁺09] P. M. Joksovic, M. Weiergräber, W. Lee, H. Struck, T. Schneider, and S. M. Todorovic, *Isoflurane-sensitive presynaptic r-type calcium channels contribute to inhibitory synaptic transmission in the rat thalamus*, *Journal of Neuroscience* **24** (2009), no. 5, 1434–1445.
- [KC76] W. Kristan and R. L. Calabrese, *Rhythmic swimming activity in neurons of the isolated nerve cord of the leech*, *J Exp Biol* **65** (1976), 643–668.
- [KE02] N. Kopell and G. Ermentrout, *Mechanisms of phase-locking and frequency control in pairs of coupled neural oscillators*, pp. 5–55, Amsterdam: Elsevier, 2002.
- [KE09] T.-W. Ko and G. B. Ermentrout, *Phase-response curves of coupled oscillators*, *Physical Review E* **79** (2009), no. 016211, 1–6.
- [KHKA⁺01] A. Kozlov, J. Hellgren Kotaleski, E. Aurell, S. Grillner, and A. Lansner, *Modeling of Substance P and 5-HT Induced Synaptic Plasticity in the Lamprey Spinal CPG: Consequences for Network Pattern Generation*, *Journal of Computational Neuroscience* **11** (2001), 183–200.
- [KS98a] J. P. Keener and J. Sneyd, *Mathematical physiology*, ch. 2,3,4, Springer-Verlag, 1998.
- [KS98b] C. Koch and I. Segev (eds.), *Methods in neuronal modeling: From ions to networks*, The MIT Press, 1998.
- [Kur84] Y. Kuramoto, *Chemical oscillations, waves, and turbulence*, New York: Springer-Verlag, 1984.
- [LB05] D. T. J. Liley and I. Bojak, *Understanding the Transition to Seizure by Modeling the Epileptiform Activity of General Anesthetic Agents*, *Journal of Clinical Neurophysiology* **22** (2005), no. 5, 300–313.
- [LC03] D. T. J. Liley and P. J. Cadusch, *Drug-induced modification of the system properties associated with spontaneous human electroencephalographic activity*, *Physical Review E* **68** (2003), 051906(15).

-
- [LCW99] D. T. J. Liley, P. J. Cadusch, and J. J. Wright, *A continuum theory of electrocortical activity*, Neurocomputing **26-27** (1999), 795–800.
- [LHKG98] A. Lansner, J. Hellgren Kotaleski, and S. Grillner, *Modeling of the Spinal Neuronal Circuitry Underlying Locomotion in a Lower Vertebrate*, Annals of the New York Academy of Sciences **860** (1998), 239–249.
- [LR03] T. J. Lewis and J. Rinzel, *Dynamics of spiking neurons connected by both inhibitory and electrical coupling*, J. Comput. Neurosci. **14** (2003), 283–309.
- [MB01] E. Marder and D. Bucher, *Central pattern generators and the control of rhythmic movements*, Current Biology **11** (2001), R986–R996.
- [MBK08] M. M. McCarthy, E. N. Brown, and N. Kopell, *Potential network mechanisms mediating electroencephalographic beta rhythm changes during propofol-induced paradoxical excitation*, Journal of Neuroscience **28** (2008), no. 50, 13488–13504.
- [MBST05] E. Marder, D. Bucher, D. J. Schulz, and A. L. Taylor, *Invertebrate central pattern generation moves along*, Current Biology **15** (2005), R685–R699.
- [MC96] E. Marder and R. L. Calabrese, *Principles of rhythmic motor pattern generation*, Physiological Reviews **76** (1996), no. 3, 687–717.
- [McC07] E. W. McCleskey, *A local route to pain relief*, Nature **449** (2007), no. 4, 545–546.
- [MCM93] D. Murchison, A. Chrachri, and B. Mulloney, *A separate local pattern-generating circuit controls the movements of each swimmeret in crayfish*, J Neurophysiol **70** (1993), no. 6, 2620–2631.
- [MG92] T. Matsushima and S. Grillner, *Neural mechanisms of intersegmental coordination in lamprey: Local excitability changes modify the phase coupling along the spinal cord*, J Neurophysiol **67** (1992), no. 2, 373–388.
- [MH00] B. Mulloney and W. Hall, *Functional organization of crayfish abdominal ganglia: Iii. swimmeret motor neurons.*, J Comp Neurol **419** (2000), 233–243.
- [MH03] ———, *Local commissural interneurons integrate information from intersegmental coordinating interneurons*, J Comp Neurol **466** (2003), 366–476.
- [MH07] B. Mulloney and W. A. Hall, *Local and Intersegmental Interactions of Coordinating Neurons and Local Circuits in the Swimmeret System*, J Neurophysiol

- 98** (2007), 405–413.
- [MHH06] B. Mulloney, P. I. Harness, and W. A. Hall, *Bursts of Information: Coordinating Interneurons Encode Multiple Parameters of a Periodic Motor Pattern*, *J Neurophysiol* **95** (2006), 850–861.
- [MMC93] B. Mulloney, D. Murchison, and A. Chrachri, *Modular organization of pattern-generating circuits in a segmental motor system: the swimmerets of crayfish*, *Semin Neurosci* **5** (1993), 49–57.
- [MS90] R. E. Mirollo and S. H. Strogatz, *Synchronization of pulse-coupled biological oscillators*, *SIAM J. Appl. Math* **50** (1990), no. 6, 1645–1662.
- [MS10] B. Mulloney and C. Smarandache, *Fifty years of cpgs: two neuroethological papers that shaped the course of neuroscience*, *Frontiers in Behavioral Neuroscience* **4** (2010), no. 45, 1–7.
- [Mul96] B. Mulloney, *During fictive locomotion, graded synaptic currents drive bursts of impulses in swimmeret motor neurons*, *J Neurosci* **23** (1996), no. 13, 5953–5962.
- [NAS⁺01] Y. Nishimura, M. Asahi, K. Saitoh, H. Kitagawa, Y. Kumazawa, K. Itoh, M. Lin, T. Akamine, H. Shibuya, T. Asahara, and T. Yamamoto, *Ionic Mechanisms Underlying Burst Firing of Layer III Sensorimotor Cortical Neurons of the Cat: An In Vitro Slice Study*, *J Neurophysiol* **86** (2001), no. 2, 771–781.
- [Nas02] H. Nash, *In vivo genetics of anesthetic action*, *British Journal of Anaesthesia* **89** (2002), no. 1, 143–55.
- [NBD⁺05] T. Netoff, M. Banks, A. Dorval, C. Acker, H. J.S., N. Kopell, and J. White, *Synchronization in hybrid neural networks of the hippocampal formation*, *J Neurophysiol* **93** (2005), 1197–1208.
- [Neu79] J. Neu, *Coupled chemical oscillators*, *SIAM J. Appl. Math* **37** (1979), no. 2, 307–315.
- [NM99] H. Namba and B. Mulloney, *Coordination of Limb Movements: Three Types of Intersegmental Interneurons in the Swimmeret System and Their Responses to Changes in Excitation*, *J Neurophysiol* **81** (1999), 2437–2450.

-
- [OM09] M. Oh and V. Matveev, *Loss of phase-locking in non-weakly coupled inhibitory networks of type-i model neurons*, *J Comput Neurosci* **26** (2009), no. 2, 303–320.
- [ONC95] O. H. Olsen, F. Nadim, and R. L. Calabrese, *Modeling the leech heartbeat elemental oscillator: II. Exploring the parameter space.*, *J. Comput. Neurosci.* **2** (1995), 237–257.
- [Ors07] B. A. Orser, *Lifting the fog around anesthesia*, *Scientific American* (2007), 54–61.
- [Pea96] R. A. Pearce, *Volatile anesthetic enhancement of paired-pulse depression investigated in the rat hippocampus in vitro*, *J Physiol* **492** (1996), no. 3, 823–840.
- [PHL⁺99] A. J. Patel, E. Honoré, F. Lesage, M. Fink, G. Romey, and M. Lazdunski, *Inhalational anesthetics activate two-pore-domain background K^+ channels*, *Nature Neuroscience* **2** (1999), no. 5, 422–426.
- [PM74] D. H. Perkel and B. Mulloney, *Motor pattern production in reciprocally inhibitory neurons exhibiting postinhibitory rebound*, *Science* **185** (1974), no. 4146, 181–183.
- [PM85] D. Paul and B. Mulloney, *Local interneurons in the swimmeret system of the crayfish*, *J Comp Physiol A* **156** (1985), 489–502.
- [RA04] U. Rudolph and B. Antkowiak, *Molecular and neuronal substrates for general anaesthetics*, *Nature Reviews Neuroscience* **5** (2004), 709–720.
- [Ram98] I. J. Rampil, *A primer for EEG signal processing in anesthesia*, *Anesthesiology* **89** (1998), 980–1002.
- [SAD⁺03] J. M. Sonner, J. F. Antognini, R. C. Dutton, P. Flood, A. T. Gray, R. A. Harris, G. E. Homanics, J. Kendig, B. Orser, D. E. Raines, J. Trudell, B. Vissel, and E. I. Eger II, *Inhaled Anesthetics and Immobility: Mechanisms, Mysteries, and Minimum Alveolar Anesthetic Concentration*, *Anesth Analg* **97** (2003), 718–740.
- [Sat85] R. A. Satterlie, *Reciprocal inhibition and postinhibitory rebound produce reverberation in a locomotor pattern generator*, *Science* **229** (1985), no. 4711, 402–404.

-
- [SGWVD85] K. Sigvardt, S. Grillner, P. Wallén, and P. Van Dongen, *Activation of nmda receptors elicits fictive locomotion and bistable membrane properties in the lamprey spinal cord*, *Brain Research* **336** (1985), 390–395.
- [SHM09] C. Smarandache, W. M. Hall, and B. Mulloney, *Coordination of rhythmic motor activity by gradients of synaptic strength in a neural circuit that couples modular neural oscillators*, *J Neurosci* **29** (2009), no. 29, 9351–9360.
- [Sig93] K. A. Sigvardt, *Intersegmental coordination in the lamprey central pattern generator for locomotion*, *Semin Neurosci* **5** (1993), no. 1, 3–15.
- [SKM94] F. K. Skinner, N. Kopell, and E. Marder, *Mechanisms for oscillation and frequency control in reciprocally inhibitory model neural networks*, *Journal of Computational Neuroscience* **1** (1994), 69–87.
- [SKM97] F. K. Skinner, N. Kopell, and B. Mulloney, *How Does the Crayfish Swimmeret System Work? Insights from Nearest-Neighbor Coupled Oscillator Models*, *Journal of Computational Neuroscience* **4** (1997), 151–160.
- [SM98a] F. K. Skinner and B. Mulloney, *Intersegmental coordination in invertebrates and vertebrates*, *Curr. Opin. Neurobiol.* **8** (1998), 725–732.
- [SM98b] ———, *Intersegmental Coordination of Limb Movements during Locomotion: Mathematical Models Predict Circuits That Drive Swimmeret Beating*, *Journal of Neuroscience* **18** (1998), no. 10, 3831–3842.
- [SPLIB98] J. E. Sirois, J. J. Pancrazio, C. Lynch III, and D. A. Bayliss, *Multiple ionic mechanisms mediate inhibition of rat motoneurons by inhalation anaesthetics*, *Journal of Physiology* **512** (1998), no. 3, 851–862.
- [SRSRS04] M. L. Steyn-Ross, D. A. Steyn-Ross, and J. W. Sleigh, *Modelling General Anaesthesia as a First-Order Phase Transition in the Cortex*, *Prog Biophys Mol Biol* **85** (2004), 369–385.
- [SRSRSL99] M. L. Steyn-Ross, D. A. Steyn-Ross, J. W. Sleigh, and D. T. J. Liley, *Theoretical electroencephalogram stationary spectrum for a white-noise-driven cortex: Evidence for a general anesthetic-induced phase transition*, *Physical Review E* **60** (1999), no. 6, 7299–7311.

-
- [SRSRSW01] M. L. Steyn-Ross, D. A. Steyn-Ross, J. W. Sleight, and L. C. Wilcocks, *Toward a theory of the general-anesthetic-induced phase transition of the cerebral cortex. I. A thermodynamics analogy*, Physical Review E **64** (2001), 011917(61).
- [Ste71] P. S. Stein, *Intersegmental coordination of swimmeret motoneuron activity in crayfish*, J Neurophysiol **34** (1971), 310–318.
- [Str94] S. H. Strogatz, *Nonlinear dynamics and chaos: With applications to physics, biology, chemistry, and engineering*, Westview Press, 1994.
- [Stu94] R. E. Study, *Isoflurane inhibits multiple voltage-gated calcium currents in hippocampal pyramidal neurons*, Anesthesiology **81** (1994), 104–116.
- [SW96] K. A. Sigvardt and T. L. Williams, *Effects of Local Oscillator Frequency on Intersegmental Coordination in the Lamprey Locomotor CPG: Theory and Experiment*, J Neurophysiol **76** (1996), 4094–4103.
- [THM01] N. Tschuluun, W. M. Hall, and B. Mulloney, *Limb movements during locomotion: Tests of a model of an intersegmental coordinating circuit*, J Neurosci **21** (2001), no. 19, 7859–7869.
- [TKB98] D. Terman, N. Kopell, and A. Bose, *Dynamics of two mutually coupled slow inhibitory neurons*, Physica D **117** (1998), 241–275.
- [TLSE00] E. M. Talley, Q. Lei, J. E. Sirois, and D. A. Bayliss, *Task-1, a two-pore domain k^+ channel, is modulated by multiple neurotransmitters in motoneurons*, Neuron **25** (2000), 399–410.
- [TSL⁺01] E. M. Talley, G. Solórzano, Q. Lei, D. Kim, and D. A. Bayliss, *CNS Distribution of Members of the Two-Pore-Domain (KCNK) Potassium Channel Family*, Journal of Neuroscience **21** (2001), no. 19, 7491–7505.
- [UB02] B. Urban and M. Bleckwenn, *Concepts and correlations relevant to general anesthesia*, British Journal of Anaesthesia **89** (2002), no. 1, 3–16.
- [VKH⁺08] P. L. Várkonyi, T. Kiemel, K. Hoffman, A. H. Cohen, and P. Holmes, *On the derivation and tuning of phase oscillator models for lamprey central pattern generators*, J Comput Neurosci **25** (2008), 245–265.
- [VVAE94] C. Van Vreeswijk, L. F. Abbott, and G. B. Ermentrout, *When inhibition not excitation synchronizes neural firing*, Journal of Computational Neuroscience **1** (1994), 313–321.

-
- [WBG⁺89] P. Wallén, J. T. Buchanan, S. Grillner, R. H. Hill, J. Christenson, and T. Hökfelt, *Effects of 5-hydroxytryptamine on the afterhyperpolarization, spike frequency regulation, and oscillatory membrane properties in lamprey spinal cord neurons*, *Journal of Neurophysiology* **61** (1989), no. 4, 759–768.
- [WEL⁺92] P. Wallén, O. Ekeberg, A. Lansner, L. Brodin, H. Tråvén, and S. Grillner, *A Computer Based Model for Realistic Simulations of Neural Networks II. The Segmental Network Generating Locomotor Rhythmicity in the Lamprey*, *Journal of Neurophysiology* **68** (1992), no. 6, 1939–1950.
- [WG87] P. Wallén and S. Grillner, *N-methyl-d-aspartate receptor-induced, inherent oscillatory activity in neurons active during fictive locomotion in the lamprey*, *Journal of Neuroscience* **7** (1987), no. 9, 2745–2755.
- [Wil61] D. Wilson, *The central nervous control of locust flight*, *J Exp Biol* **38** (1961), no. 2, 471–490.
- [Wil92a] T. L. Williams, *Phase coupling by synaptic spread in chains of coupled neuronal oscillators*, *Science* **258** (1992), 662–665.
- [Wil92b] ———, *Phase coupling in simulated chains of coupled oscillators representing the lamprey spinal cord*, *Neural Computation* **4** (1992), 546–558.
- [Wil02] A. R. Willms, *Neurofit: software for fitting hodgkin-huxley models to voltage-clamp data*, *Journal of Neuroscience Methods* **121** (2002), no. 2, 139–150.
- [Win80] A. Winfree, *The geometry of biological time*, Springer-Verlag, Berlin, 1980.
- [WR92] X.-J. Wang and J. Rinzel, *Alternating and synchronous rhythms in reciprocally inhibitory model neurons*, *Neural Computation* **4** (1992), 84–97.
- [WS94] T. L. Williams and K. A. Sigvardt, *Intersegmental phase lags in the lamprey spinal cord: Experimental confirmation of the existence of a boundary region*, *Journal of Computational Neuroscience* **1** (1994), 61–67.
- [WS95] ———, *The Handbook of Brain Theory and Neural Networks*, pp. 918–921, The MIT Press, 1995.
- [WSK⁺90] T. L. Williams, K. A. Sigvardt, N. Kopell, G. B. Ermentrout, and M. P. Remler, *Forcing of coupled nonlinear oscillators: Studies of intersegmental coordination in the lamprey locomotor central pattern generator*, *Journal of Neurophysiology* **64** (1990), no. 3, 862–871.

- [WW84] T. Williams and P. Wallén, *Fictive locomotion in the lamprey spinal cord in vitro compared with swimming in the intact and spinal animal*, *J Physiol.* **347** (1984), 225–239.
- [WWBB06] M. Wechselberger, C. L. Wright, G. A. Bishop, and J. A. Boulant, *Ionic channels and conductance-based models for hypothalamic neuronal thermosensitivity*, *Am J Physiol Regul Integr Comp Physiol* **291** (2006), R518–R529.
- [ZS09] T. Zahid and F. K. Skinner, *Predicting synchronous and asynchronous network groupings of hippocampal interneurons coupled with dendritic gap junctions*, *Brain Research* **1262** (2009), 115–129.